Single Proton Transfer on ^{55}Mn

Richard Thomas Newman

A thesis submitted in ~~partial~~ fulfilment of the requirements
for the degree of Doctor of Philosophy
in the Department of Physics
University of Cape Town

September 1996

Single Proton Transfer on ^{55}Mn

Richard Thomas Newman

National Accelerator Centre, P. O. Box 72, Faure, 7131, South Africa

e-mail: newman@nac.ac.za

Abstract

Differential cross sections for the ^{55}Mn(d,^{3}He)^{54}Cr and ^{55}Mn(d,d)^{55}Mn(g.s.) reactions at E_d = 45.6 MeV were measured in the 6°–48° angular region (laboratory frame) using a k = 600 MeV magnetic spectrometer with a resolution of $\sim$ 40 keV (full-width at half maximum). Spectroscopic factors associated with the observed transitions to twenty-four ^{54}Cr final states up to 6.107 MeV excitation were determined from local, zero-range distorted-wave Born approximation (DWBA) analyses of the measured angular distributions, allowing for $\ell = 0, 1, 2$ and 3 transfers. An optical-model analysis of the (d,d) data has been performed in order to yield optimum values of the potential parameters required for calculating the distorted wave-functions associated with the entrance channel.

Spin-dependent non-energy weighted sum-rule (NEWSR) analyses of the $0f_{\frac{7}{2}}$ proton transfer data were made using existing complementary stripping data obtained from a study of the ^{55}Mn(α,t)^{56}Fe reaction. The NEWSR analyses, together with comparisons with the predictions of $0f1p$ shell-model calculations exploiting a new effective interaction for A = 41–66 nuclei, have resulted in the assignment of spins 6^+, 5^+ and 6^+ to the ^{54}Cr levels located at 3.222, 3.786 and 4.042 MeV excitation respectively. For the remaining orbitals of the $0f1p$ shell, the findings are consistent with a small $1p_{\frac{3}{2}}$, and negligible $0f_{\frac{5}{2}}$ and $1p_{\frac{1}{2}}$ proton occupancy in ^{55}Mn. A substantial fraction of the $0s1d$ proton pickup strength was located above 4.128 MeV excitation energy, allowing further spin and parity assignments to be made, in particular that of 3^- to the 4.245 MeV state of ^{54}Cr. The NEWSR fits, though acceptable, are inferior to those previously obtained, indicating some deficiencies in the $0f_{\frac{7}{2}}$ proton transfer data used. Nevertheless, good overall agreement with the results of the shell-model calculations was found, underlining the reliability of these calculations.

- Mr. Zain Karriem[δ] for his assistance with the calculations reported on in appendix A;
- D. S. for making his energy-loss program STACK available to me;
- Dr. Friedrich Neumeyer[ϵ] and Mr. Steffen Strauch[ϵ] for supplying me with their peak-fitting program FIT2.1;
- R. S., C. S, Mr. Adriaan Müller[β] and Mr. Bruno Eisinger[β] for providing me with some of the figures shown below;
- Drs. John Pilcher[β] and Kobus Lawrie[β] for their assistance with many aspects of the data handling;
- Drs. Bruce Simpson[β], R. S., K. L. and D. S. for sharing their insight concerning many aspects of the data analysis;
- my thesis proof-readers: B. S., R. S., Dr. Siegie Förtsch[β], D. S., J. P. and Dr. Lowry Conradie[β];
- The University of Cape Town (UCT) Research Committee, the UCT Mellon Foundation and the Foundation for Research Development for their financial support and
- last but not least, those closest to me: my mother (to whom I dedicate this thesis), my father, Des, Gilli, Pierre, Raquel, Simon, Nina, Candice, Eunice, Howard, Garth and Crystal for their loving support throughout the duration of this project.

Richard Newman, *Faure, September 1996*

Acknowledgements

I wish to express my sincere gratitude to the following[1] for making the realization of this thesis possible:

- my co-supervisors, Prof. Sandy Perez[α] and Dr. Roger Fearick[α], for their patient guidance and support throughout the duration of the project;
- the director of the National Accelerator Centre (Faure, South Africa) and members of its program advisory panel for their allocation of beam-time to this project;
- Dr. Adriaan Botha[β] and his skilled team for delivering a reliable deuteron beam onto target;
- Dr. Ricky Smit[β], Dr. Deon Steyn[β], Mr. Charles Stevens[β] and Mr. Charles Wikner[β] for their design and construction of spectrometer hardware, especially items required for the experiments discussed below;
- those who assisted with the manufacture of the target and its thickness measurement: Mr. Dieter Geduld[α], Mr. Chris Theron[θ], Dr. Cecil Churms[θ], Dr. Terence Marais[θ] and Dr. Raven Naidoo[ψ];
- those who assisted during the many weekends of data acquisition: R. F., R. S., Mr. Victor Tshivhase[α,β], Mr. Trevor Volkwyn[α], Prof. Krish Bharuth-Ram[γ] and Prof. David Aschman[α];
- Dr. Werner Richter[φ] for performing the shell-model calculations;
- Mr. Garrett de Villiers[β] for performing the ion-optical simulations;
- R. S. and D. S. for performing the drift-chamber simulations;

[1] α: University of Cape Town, β: National Accelerator Centre, γ: University of Durban-Westville, ϕ: University of Stellenbosch, θ: Van de Graaff group (National Accelerator Centre), ψ: Ministry of Trade and Industry, ϵ: Technische Hochschule, Darmstadt (Federal Republic of Germany), δ: University of the Western Cape.

Contents

List of Figures

List of Tables

Chapter 1

Introduction

One of the most successful models of the intrinsically many-body nature of the atomic nucleus is the tractable and intuitively appealing single particle[1] shell model developed by Goeppert-Mayer, Jensen, Haxel and Süss in 1949 (for example, [Man85, Sic91, Gra92, Hey94, Wal95]). In this model the nucleus is described as an assembly of independent nucleons, each of which moves in a well-defined orbit subject to a mean field associated with the remaining nucleons. Despite its many successes, including the accounting for the nuclear magic numbers and the prediction of the ground-state properties of nuclei near closed shells, the validity of the shell model remains a subject of ongoing research (for example,[den88a, Per88, Wag90, Gra94]). This is a consequence of experimental findings that the number of nucleons occupying single particle orbits may be considerably smaller than naive shell-model predictions. Since the mean field approximation (MFA) is the leading contribution in an expansion of multi-particle correlations [Udí93], this quenching of the single particle occupancy is considered by some (for example, [Wag90, Gra94]) to be indicative of a fundamental shortcoming in the shell model. In particular, the above evidence supports the contention that the residual interaction between nucleons is significant [Gra92]. The validity of this contention depends crucially on whether single particle occupancies can be accurately extracted from experimental measurements. The manner in which these occupancies are measured is addressed next.

[1] Also referred to as the independent-particle shell model.

1.1 Measurement of occupancies

In order to obtain the occupancy of the single particle state α in a given nucleus, single-nucleon transfer spectroscopic factors, S_α, need to be determined for that nucleus. For reactions in which a single nucleon is removed (for example via pickup or quasifree-knockout reactions) from an initial state i of a nucleus of mass A resulting in a final state f of a nucleus of mass $A-1$, S_α is given by

$$S_\alpha^- = |\langle A-1, f|a_\alpha|A, i\rangle|^2 \tag{1.1}$$

where a_α is the annihilation operator [Wag90]. For the analogous reaction in which a nucleon is added to a nucleus (for example via a stripping reaction), the corresponding S_α reads

$$S_\alpha^+ = |\langle A+1, f|c_\alpha|A, i\rangle|^2 \tag{1.2}$$

where c_α is the creation operator.

The particle (hole) occupancy of a state α can then be determined by summing up to infinite excitation the spectroscopic factors S_α determined from experiments in which a single nucleon is removed (added) from (to) a nucleus [Gra94]. In a variant of the above, derived by French and MacFarlane (for example [Cle73, Wag90, Cle91, Gra94]), the sum of particle and hole occupancies associated with a state characterized by a total angular momentum j, should amount to $(2j+1)$. This sum rule, also referred to as the total sum rule, will be further discussed below.

Two approaches (other than the application of spin-dependent spectroscopic sum rules) are currently considered the most reliable in determining absolute spectroscopic factors and occupancies associated with single particle states. The first of these involves the use of the quasifree-knockout $(e,e'p)$ reaction. Since the electromagnetic interaction is well understood this approach should enable absolute spectroscopic factors to be determined with good accuracy. There are, however, ambiguities stemming from the manner in which the $(e,e'p)$ reaction mechanism is modelled which result in uncertainties in the extracted spectroscopic information. In this regard the treatment of the Coulomb distortion of the electron has been shown to be important [Udí93]. Analyses based on a nonrelativistic treatment of

this distortion using the eikonal approximation have resulted in severely quenched occupancies [Udí93, Udí95]. So for example, one study has shown that for target nuclei with A $\geq$ 12 the observed spectroscopic strength for valence orbits is only 50% of the shell-model limit [Wag90]. Subsequently a full partial-wave analysis of electron waves in the Coulomb potential of the target has led to an increase from $\sim$ 0.50 to $\sim$ 0.70 of the spectroscopic factor associated with the much-studied reaction in which a proton is removed from the $3s_{\frac{1}{2}}$ orbital in ^{208}Pb [Udí95]. Further questions surrounding the use of nonrelativistic and relativistic optical model potentials (for example, [Hod74, Eis88, Sat90, Bur95]) for the outgoing proton waves have recently been raised and are being investigated [Udí95].

The second manner in which occupancies are believed to be reliably determined is via the CERES (Combined Evaluation of Relative spectroscopic factors and Electron Scattering) formalism [Wag90, Sic91, Gra92, Gra94]. This approach involves the use of the ratio of truncated sums[2] of relative spectroscopic factors (extracted via single-nucleon transfer reactions on neighbouring target nuclei) and charge-density differences of isotones obtained via elastic electron scattering. In a recent study [Udí93] an occupation probability of 0.78 $\pm$ 0.12 has been found for the $3s_{\frac{1}{2}}$ orbital in ^{208}Pb using this approach. The extraction of occupancies from CERES analyses is however also not free of ambiguities, as for example in the assumption of equal quenching of transfer strength in different nuclei.

The use of spectroscopic factors obtained directly from transfer reactions involving hadrons in the entrance and exit channels is largely ineffective as a means of determining occupancies because of uncertainties associated with the absolute normalization of these spectroscopic factors [Moa79, Nan89, Cle91]. These uncertainties stem primarily from the manner in which the reaction mechanism is modelled. For single-nucleon transfer reactions the experimentally measured differential cross section for the transition to a particular final state is proportional to the product of the spectroscopic factor and the corresponding differential cross section calculated within

[2]Normally over a $\sim$ 5 MeV excitation region since the level densities become too high above this region to determine spectroscopic factors associated with transitions to discrete states.

the framework of the distorted-wave Born approximation (DWBA) (for example, [Aus60, Aus64, Roy67, Jac77, Sat83, Eis88, Bur95]). In particular, for the case of pickup and stripping reactions respectively:

$$\sigma(\theta)_{\text{expt}} = \sum_{j\ell} C_p^2 S_{j\ell}^p (\sigma(\theta)_{\text{DWBA}})_{j\ell} \tag{1.3}$$

$$\sigma(\theta)_{\text{expt}} = \sum_{j\ell} \frac{[J']}{[J_t]} C_s^2 S_{j\ell}^s (\sigma(\theta)_{\text{DWBA}})_{j\ell} \tag{1.4}$$

where

- j and ℓ denote total and orbital angular-momentum transfer, respectively;
- J' and J_t denote the final-state and target ground-state spin, respectively;
- $[x] = (2x + 1)$;
- $\sigma(\theta)_{\text{expt}}$ and $\sigma(\theta)_{\text{DWBA}}$ denote the measured and calculated DWBA differential cross sections, respectively;
- S^p and S^s denote pickup and stripping spectroscopic factors, respectively; and
- C_p and C_s denote the corresponding isospin Clebsch-Gordan coefficients.

In practice, spectroscopic factors are determined by normalizing a portion (normally including the peak) of the DWBA angular distribution to the corresponding experimental data. One of the main sources of uncertainty associated with the extracted spectroscopic factors is the strong dependence of the calculated cross section on the potential parameters used to generate the distorted wave-functions for the entrance and exit channels, and the bound-state wave function, $\psi_\alpha(r)$, which describes the transferred nucleon [Moa79, Gra92]. The dependence of the calculated DWBA differential cross section on the bound-state radius has been shown to be particularly pronounced [Wag90, Cle91, Sic91]. So for example, a 1% change in the radius parameter of the potential used to calculate $\psi_\alpha(r)$ translates

E* (MeV)	J^π	$(d,^3\mathrm{He})^a$	$(d,^3\mathrm{He})^b$	$(e,e'p)^c$
0	0^+	0.73 (0.78)	0.41 (0.73)	0.37 (0.83)
1.55	2^+	0.39 (0.42)	0.22 (0.39)	0.15 (0.33)
2.67	4^+	0.64 (0.68)	0.41 (0.73)	0.33 (0.74)
3.22	6^+	1.05 (1.12)	0.65 (1.15)	0.49 (1.10)
Total:		2.81 (3.00)	1.69 (3.00)	1.34 (3.00)

[a] from Ref. [Hin67].

[b] from Ref. [Kra88].

[c] from Ref. [den88b].

Table 1.1: *Absolute and, in parentheses, the corresponding relative spectroscopic factors for $0f_{\frac{7}{2}}$ proton removal from ^{51}V. (Adapted from Ref. [Wag90].)*

into about a 10% change in absolute spectroscopic factor [Moa79, Sic91]. As a result absolute spectroscopic factors are inherently strongly model-dependent. Furthermore summing these spectroscopic factors to calculate occupancies is problematic since only a finite excitation energy region can be sampled, and the spectroscopic strength of an orbit of interest may not have been exhausted. Typically only strength associated with transitions to states at excitation energies, E*, up to about 5 MeV in the residual nucleus can be reliably extracted. Any higher-lying strength due to, for example, short-range correlations and the coupling of single particle strength to giant resonance excitations, is therefore ignored in calculating occupancies in this way [Sic91].

In contrast to their absolute counterparts, relative values of spectroscopic factors from independent experiments generally agree to within $\sim 10\%$ [Cle77, Cle91]. This is due to the fact that many experimental and theoretical sources of error largely cancel, as is illustrated in table 1.1 where the absolute and the corresponding relative spectroscopic factors associated with the $0f_{\frac{7}{2}}$ proton removal on ^{51}V are compared. This consistency of relative spectroscopic factors has led to the development of a formalism based on the standard (asymmetric) form of the non-energy weighted sum rules

(NEWSR) [Cle91], whereby complementary sets of spectroscopic strength spin-distributions (spectroscopic factors and corresponding final-state spins) can be critically examined. The NEWSR formalism has been used, *inter alia*, to assess the consistency of the input data (i.e. the spin distributions), determine absolute DWBA normalizations [Cha77, Cle77, Moa77], make spin assignments to final states [Cle73]; and provide insight, albeit indirectly, into the unobservable single particle strength located beyond the excitation region probed experimentally [New95].

An important component of the formalism, which is detailed in chapter 4, involves introducing the renormalization constants n^- and n^+ to take into account errors in the absolute normalizations of pickup and stripping spectroscopic factors, respectively, as derived from DWBA analyses of transfer data. The goodness-of-fit to the NEWSR is assessed by plotting an error parameter σ, which is indicative of the average uncertainty associated with relative spectroscopic factors, as a function of n^+ or n^-. For cases where the NEWSR fit the input data well the curve of σ versus renormalization constant displays a distinct minimum. The smaller the minimum value σ_{min} of σ, the more significant any fit to the sum rules is and the more reliable the complementary sets of transfer spin-distributions are. If a value of $\sigma_{min} \leq 10\%$ is obtained the transfer spin-distributions are considered to satisfy the sum rules. In this event the absolute DWBA normalizations can be determined from the values of n^+ and n^- corresponding to σ_{min}. These spectroscopic factors can then be used, *inter alia*, to determine expectation values associated with one-body operators acting on the target ground-state by using further sum rules. One such extensively used sum rule is the dipole sum rule [Cle91] which allows the target ground-state spin to be calculated from the estimated absolute spectroscopic factors.

NEWSR analyses have mostly been performed on $0f_{\frac{7}{2}}$ transfer data acquired in the lower part of the fp shell [Cle77, Cle91]. This is because the large energy gap between the $0f_{\frac{7}{2}}$ and $0f_{\frac{5}{2}}$ orbitals allows a confident assignment of $0f_{\frac{7}{2}}$ to any $\ell = 3$ transition to a low excitation energy final state in this mass region. A further reason for focussing on $0f_{\frac{7}{2}}$ transfer is the fact that the number of independent linear relations constituting the NEWSR is equal to the smaller of $[J_t]$ and $[j]$ [Cle91]. Thus the larger

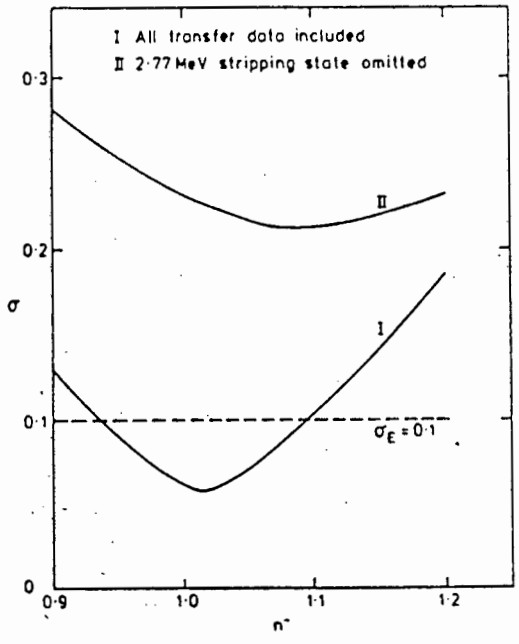

Figure 1.1: *Results of a NEWSR analysis of complementary sets of spin distributions associated with $0f_{\frac{7}{2}}$ proton transfer on ^{51}V. The relative error parameter, σ, is plotted as a function of pickup renormalization constant, n^-. The effect of omitting all the strength (20% of the total strength) associated with the 2.77 MeV stripping state is shown. (Reproduced from Ref. [Cle91].)*

J_t, the greater the number[3] of linear relations representing the NEWSR, and the greater the overdeterminancy of any quantity to be determined through the sum rules (e.g. the renormalization constants n^+ and n^-). So for example, using $0f_{\frac{7}{2}}$ transfer data for ^{51}V ($J_t = \frac{7}{2}$) in a NEWSR analysis involves eight independent linear relations in sixteen partial spectroscopic sums. It is this overdeterminancy which makes the NEWSR formalism such a powerful diagnostic tool. The sensitivity of the NEWSR to the distribution of transfer strength is shown in figure 1.1, where the effect of omitting some of the strength is illustrated.

Analyses of $0f_{\frac{7}{2}}$ transfer data on ^{41}Ca, ^{43}Ca, ^{45}Sc, ^{49}Ti and ^{51}V that have been made thus far have resulted in successful fits to the NEWSR in all cases [Cle77, Cle91], with values of σ_{min} varying between 3% and 9% [Cle91]. Renormalization constants obtained from these NEWSR analyses, together with subsequent dipole sum-rule analyses, are consistent with orbit occupancies being close to those expected from the shell model. This is in contrast to results from $(e,e'p)$ work and CERES analyses which indicate a quenching of occupancy, as discussed above, of $\sim$ 30%.

1.2 Aims and scope of this study

The primary motivation for conducting this study [New96] was the desire to complement the existing NEWSR analyses of $0f_{\frac{7}{2}}$ transfer data on odd-even fp-shell nuclei, in order to attempt obtaining further corroboration for the trends delineated above.

Odd-even nuclei with $40 < A < 60$ for which complete sets of $0f_{\frac{7}{2}}$ transfer data were unavailable before the completion of this study are listed in table 1.2. From this table it can be seen that ^{47}Ti and ^{55}Mn were the only remaining targets in the lower part of the fp shell with $J_t \geq \frac{5}{2}$ for which NEWSR analyses[4] had not been performed [Cle91]. The latter target was focussed on in this study mainly because a set of stripping

[3] Even-even targets, with $J_t = 0$, yield only the total sum rule, from which the renormalization constants n^- and n^+ cannot be determined.

[4] A sum-rule analysis on these two targets will therefore involve six independent linear relations.

nucleus	isotopic abundance (%)	ground-state spin	N
^{47}Ti	7.4	$\frac{5}{2}$	6
^{53}Cr	2.36	$\frac{3}{2}$	4
^{55}Mn	100	$\frac{5}{2}$	6
^{57}Fe	2.2	$\frac{1}{2}$	2

Table 1.2: *Remaining odd-even fp-shell nuclei with incomplete* $0f_{\frac{7}{2}}$ *transfer data. N represents the number of independent linear relations constituting the NEWSR.*

spectroscopic factors for single proton transfer on ^{55}Mn is available in the literature [Mat68]. The fact that ^{54}Cr final states, which are reached via proton pickup on ^{55}Mn, are mostly well-separated and have known spins, along with the fact that ^{55}Mn occurs with a 100% natural isotopic abundance while ^{47}Ti occurs with an abundance of only 7.4%, were additional reasons for choosing ^{55}Mn as the target nucleus in this study.

Two earlier studies of proton stripping on ^{55}Mn exist. A summary of the pertinent results are given in table 1.3. The first study was performed using the (^{3}He,d) reaction [Hin67]. The transitions to only three ^{56}Fe final states were studied and no spectroscopic factors were reported. A more extensive study by Matoba [Mat68] used the (α,t) reaction to study transitions to twelve ^{56}Fe final states. Two previous studies of proton pickup on ^{55}Mn also exist. The main results from these studies are summarized in table 1.4. In the first, Colli *et al.* [Col59, Col61] reported transitions to five final states observed via the (n,d) reaction. However they only extracted the spectroscopic factor for the transition to the ^{54}Cr ground state. The second study, by Yntema *et al.* [Ynt61] who employed the (d,^{3}He) reaction, yielded no spectroscopic factors.

A reliable set of spectroscopic factors for $0f_{\frac{7}{2}}$ proton pickup on ^{55}Mn was therefore required. In the present study these were obtained through DWBA analyses of new measurements of the differential cross section for the ^{55}Mn(d,^{3}He)^{54}Cr reaction at a nominal beam energy of 45 MeV. This beam energy was chosen to exploit available parameterizations of the mass dependence of optical potentials for ^{3}He at 39.7 MeV [Bar77] and 41 MeV [Tro80],

reaction	E* (MeV)	ℓ transfer	$\frac{[J']}{[J_t]}C^2S$	Ref.
(^{3}He,d)	0.85	1,3		[Hin67]
	2.09	1,3		
	2.66	1		
(α,t)	0.00	3	0.01	[Mat68]
	0.85	3	1.45	
	2.09	3	0.36	
	2.66	3	0.14	
	2.97	3	0.08	
	3.15	3		
	3.40	3	0.90	
	3.78	3	0.25	
	4.08	1		
	4.42	1		
	4.73	1		
	5.20	1		

Table 1.3: *Summary of available proton stripping data on ^{55}Mn as compiled in Refs. [Jun87, Jun92].*

reaction	E* (MeV)	ℓ transfer	S	Ref.
(n,d)	0.00	3	0.59	[Col59, Col61]
	0.90			
	1.80			
	$\sim$ 3.0			
	$\sim$ 4.0			
(d,^{3}He)	0.00			[Ynt61]
	0.84			
	1.90			

Table 1.4: *Summary of available proton pickup data on ^{55}Mn as compiled in Refs. [Gon87, Jun93].*

from which distorted wave-functions for the exit channel could be determined.

The form of the optical potential used to generate the distorted waves for the entrance channel was identical to the one used to obtain a global parameterization of deuteron optical-model parameters [Boj88]. In order to obtain optimum parameters for this potential, the angular distribution for the ^{55}Mn(d,d)^{55}Mn(g.s.) reaction was measured in conjunction with the pickup data, and subsequently analysed with a standard optical-model code.

Another aim of this study was to further investigate the use [New95] of a symmetric form of the diagonal NEWSR together with an improved error-analysis formalism. A further advantage of using the symmetric rather than the standard form of the NEWSR is that the total sum rule is obtained separately for one of the linear relations constituting the former sum rules, and is thus decoupled from the remaining linear relations. After estimating the fraction, γ, of transfer strength located above the excitation region considered (typically in the 0–5 MeV region), absolute spectroscopic factors can be determined. Furthermore, the symmetric form is suggestive of a possible spin distribution associated with the transfer strength located above the excitation region studied [New95].

Recently, shell-model calculations have been performed for A = 41–66 nuclei, using a new two-body effective interaction and a model space which allows for the excitation of a $0f_{\frac{7}{2}}$ particle to the $1p_{\frac{3}{2}}$, $0f_{\frac{5}{2}}$ and $1p_{\frac{1}{2}}$ subshells [van94]. Theoretical energy levels and static electromagnetic moments have been shown to be in good agreement with their experimental counterparts [van94]. In order to further assess the quality of these calculations, the derived wave functions were used to calculate spectroscopic factors for comparison with those determined through single proton transfer on ^{55}Mn. This assessment constituted the third and final aim of this study.

1.3 Thesis overview

To conclude the introduction, the structure of the remainder of this dissertation is outlined.

The experimental methods used to acquire the proton pickup and deuteron elastic scattering data on ^{55}Mn are discussed in chapter 2. The extraction of pickup angular distributions from these data and subsequent calculation of spectroscopic factors via DWBA analyses are described in chapter 3; while the analysis of the deuteron elastic scattering data is discussed in appendix F. In chapter 4 the results of the shell-model calculations are first presented. This is followed by a description of how the stripping and pickup spin-distributions for $0f_{\frac{7}{2}}$ proton transfer on ^{55}Mn were established. Non-energy weighted sum-rule analyses of these spin distributions are then described. A concluding summary, along with suggestions for possible complementary studies, are presented in the final chapter.

Chapter 2

The Experiments

In this chapter the experimental techniques which were used to measure the data required to perform non-energy weighted sum-rule (NEWSR) analyses of data for $0f_{\frac{7}{2}}$ proton transfer on ^{55}Mn are detailed. As discussed in section 1.2, Matoba's ^{55}Mn(α,t)^{56}Fe study [Mat68] yielded a set of stripping spectroscopic factors, leaving the complementary set of pickup data to be measured. In this study these data were extracted from measured differential cross sections associated with the ^{55}Mn(d,^{3}He)^{54}Cr reaction at a nominal beam energy of 45 MeV. As a by-product of the above, the ^{55}Mn(d,d)^{55}Mn(g.s.) reaction was studied at the same beam energy. These data were then used (see appendix F) to obtain optimized optical-potential parameters for the entrance channel of the ^{55}Mn(d,^{3}He)^{54}Cr reaction in the distorted-wave Born approximation (DWBA) analyses.

2.1 Overview

The differential cross sections for the ^{55}Mn(d,^{3}He)^{54}Cr and ^{55}Mn(d,d)^{55}Mn(g.s.) reactions were measured using a k = 600 magnetic spectrometer[1] at the National Accelerator Centre (NAC), the national multi-disciplinary research

[1]The energy constant, k, is defined as k = $\frac{mE}{q^2}$, where q and m are in units of proton charge and mass respectively; and E is the the kinetic energy of the particle in MeV units [Weg87].

facility at Faure[2] in the Republic of South Africa. The measurements were made intermittently between December 1991 and September 1994.

The light (charged) reaction products were detected in the spectrometer's focal-plane detector array [Ful85] consisting of a vertical drift chamber[3](VDC) [Ber77] followed by two plastic scintillator paddle detectors. Signals from the paddles were used to generate the event trigger, while the momenta of the ejectiles were determined from the position where they intersected the wire-plane of the VDC. Particle identification of the rigidity-selected reaction products was effected by studying their times-of-flight through the spectrometer.

2.2 Deuteron beam

At the NAC, particle beams are initially accelerated using one of two solid-pole injector cyclotrons [Bot84, Pil89a]. The first injector, solid-pole cyclotron 1 (SPC1), is used to accelerate light-ion beams, while the second, SPC2, is used to accelerate mainly heavy ions, polarized protons and deuterons. Beams extracted from the injectors are then further accelerated in a separated-sector cyclotron (SSC) until the beam particles attain the required kinetic energy. A floor-plan of the NAC facility showing, *inter alia*, the locations of these cyclotrons is shown in figure 2.1.

For this experiment deuterium gas molecules were ionized in a Penning Ion Gauge ion-source located at the centre of SPC1 (k = 8). A hot filament inside the ion-source thermally ejects electrons from a lanthanum hexaboride (LaB_6) pellet (cathode) into a plasma-filled anode column [Con94]. Deuterons were extracted from the plasma by means of negatively charged puller electrodes and accelerated in SPC1. At a radius of about 0.48 m the deuterons have been accelerated to an energy of 4 MeV and were then extracted from SPC1 for injection into the NAC's main cyclotron, the k = 200 SSC. To accelerate deuterons to about 45 MeV a radio frequency of $\sim$ 9.9 MHz is used for the acceleration voltage. Although a maximum pulse

[2]Located approximately 30 km from Cape Town.

[3]The term was coined to refer to drift chambers in which the direction of electron drift is perpendicular to the wire-plane.

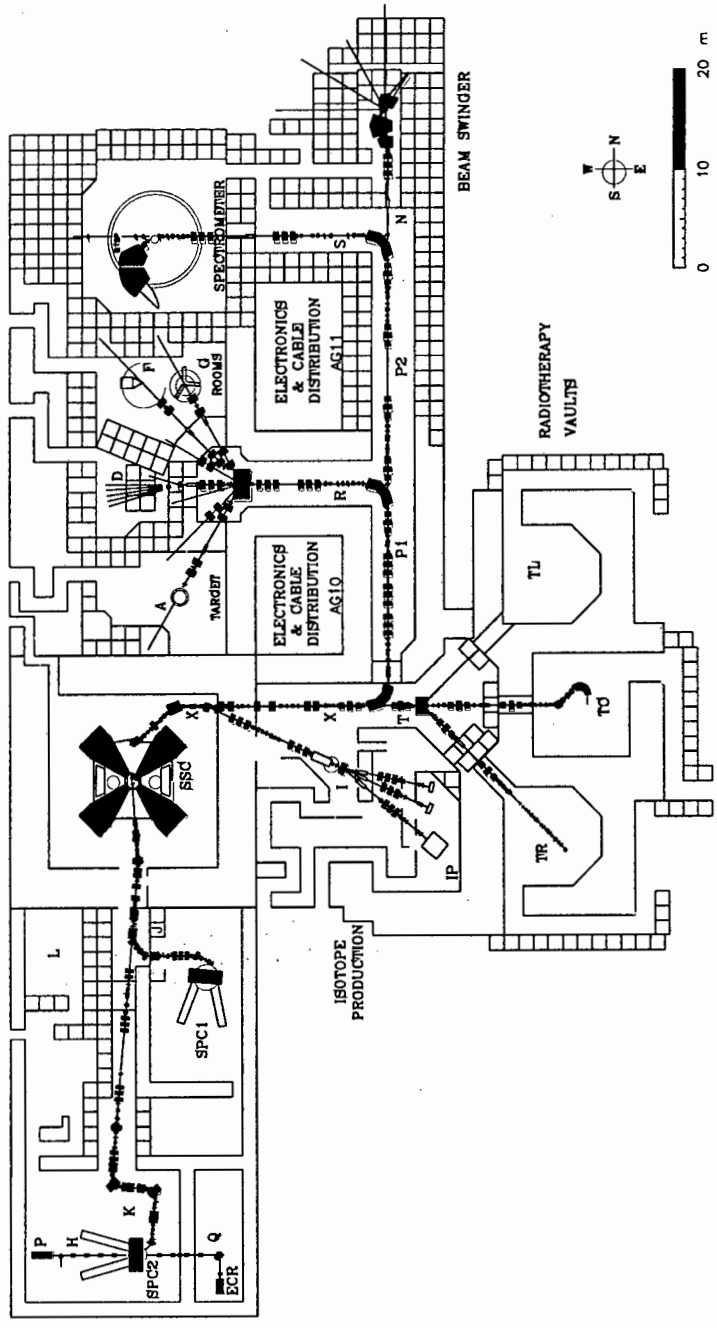

Figure 2.1: *Floor-plan of the NAC cyclotron facility.*

selection of one in three is available for a deuteron beam of 45 MeV, no pulse selection was used since the associated beam-burst interval of about 100 ns proved convenient for identifying particles by means of the time-of-flight technique (see section 2.6).

After extraction from the SSC the deuteron beam was steered along the X, P_1, P_2 and S beam-lines (see figures 2.1 and 2.2), and delivered achromatically onto the target. The beam energy was calculated from the currents supplied to two 90° bending magnets located along the extraction beam-line. An uncertainty of $\sim$ 0.25 MeV [Bot95] is associated with this measurement. The average energy of the beam delivered for this study was 45.6 MeV. In order to optimize resolution on target the widths of energy-defining slits located along the X and P_1 beam-lines respectively, were kept fixed at 1.00 mm. As a result the energy spread in the beam was about 10 keV since this spread, δE, is calculated using the relation

$$\delta E = \frac{2E}{R_1} \tag{2.1}$$

where E is the beam energy and R_1 the first-order resolving power[4].

At the start of an experimental session the beam alignment on target was checked by reducing the current to about 3 nA and using closed circuit television to monitor the beam spot on an aluminium oxide viewer. This viewer had a 3 mm diameter hole located at its centre. When perfectly aligned, the beam passed through the central hole in the viewer with no afterglow. Beam halo was reduced by tuning the beam in order to minimize the paddle count rate (see section 2.7.1) when using an empty target frame. In this manner it was possible to reduce the halo rate down to $\leq$ 4% of the count rate obtained with the target in place. Beam intensities on target varied between 1 nA and 29 nA. The accumulated charge associated with

[4]The first-order resolving power, R_1, expresses the capability of a spectrometer to separate particles of different momenta and is defined as the ratio of the horizontal momentum dispersion to image size, i.e.

$$R_1 = \frac{R_{16}}{R_{11} X_o}$$

where X_o is the slit-width, R_{11} relates the final beam-width to the initial beam-width and R_{16} describes the broadening of the beam caused by the dispersion of the system. While performing the experiments the first-order resolving power was typically 8000.

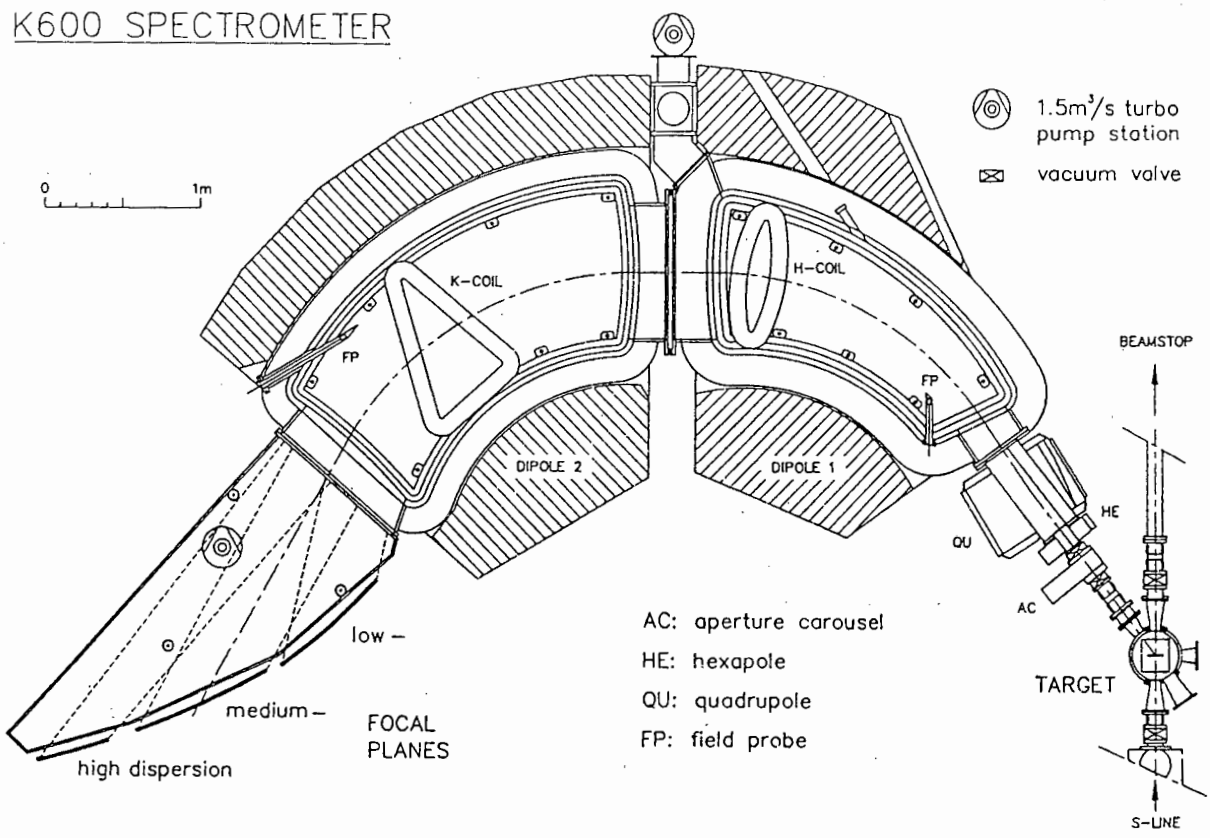

Figure 2.2: *Drawing of the k = 600 magnetic spectrometer at the NAC. The locations of the focal planes associated with the low-, high- and medium-momentum dispersion modes respectively, are shown.*

pickup data-sets varied between 96 μC and 506 μC, while that for elastic scattering varied between 0.02 μC and 48 μC.

2.3 K = 600 spectrometer

The k = 600 magnetic spectrometer at the NAC is based on the design of the K600 spectrometer at the Indiana University Cyclotron Facility (IUCF) [Ber86, Ber88, Ber89, Bac90]. This spectrometer comprises[5], *inter alia*, a quadrupole, two dipole magnets, and K and H trim-coils (see figure 2.2). The K-coil which is located inside the second dipole (D_2) is used to adjust $(x|\theta)$ for first-order point-to-point focussing from the object-slit to the focal plane while the H-coil, located inside the first dipole (D_1), is used to correct for $(x|\theta^2)$ aberrations [Ber79, Off87] (see also section 2.9).

The spectrometer can be operated in a low-, high- or medium-momentum dispersion mode, with the last mentioned being the one used in this study. The focal-planes associated with each of these modes are also shown in figure 2.2. A summary of the NAC k = 600 spectrometer's technical specifications for its medium dispersion mode is given in table 2.1.

Targets (see section 2.4) were mounted inside a 301 mm diameter scattering chamber which was positioned in relation to the incident deuteron beam as shown in figure 2.3. After exiting the scattering chamber, the ejectiles pass through a collimator which defines the spectrometer's angular acceptance (detailed in section 2.3.3). Those particles which are charged follow a curved path through the spectrometer causing particles with different momenta, but with sufficient rigidity, to be focussed at different points along the spectrometer focal plane (see figure 2.12).

2.3.1 Focal-plane detectors

Reaction products which moved through the spectrometer were detected by means of a vertical drift chamber (VDC) followed by two plastic scintillation paddle detectors. These detectors were positioned along the medium-

[5]The hexapole magnet was not used.

feature	value
maximum momentum per charge, p/Q	1080 MeV/c
maximum proton energy	493 MeV
maximum particle rigidity	3.60 Tm
maximum dipole fields (D_1 and D_2)	1.64 (T)
dipole field ratio	1
nominal bend radius	2.1 m
nominal bend angle	115°
maximum solid angle, $\Delta\theta\Delta\phi$	6.0 msr
maximum horizonal acceptance, $\Delta\theta$	± 44 mrad
maximum vertical acceptance, $\Delta\phi$	± 44 mrad
momentum range, P_{max}/P_{min}	1.097
resolving power, $P/\delta P$ (0.6 mm object slit)	28000
momentum dispersion	8.4 cm/%
energy dispersion (200 MeV protons)	42 kev/mm
horizontal magnification at p_{max}	–0.52
vertical magnification at p_{max}	7.4
central-ray angle w.r.t. focal plane	35.75°
horizontal VDC acceptance	78 cm
vertical VDC acceptance	10 cm

Table 2.1: *Technical specifications for the medium-momentum dispersion mode of the NAC k = 600 magnetic spectrometer.*

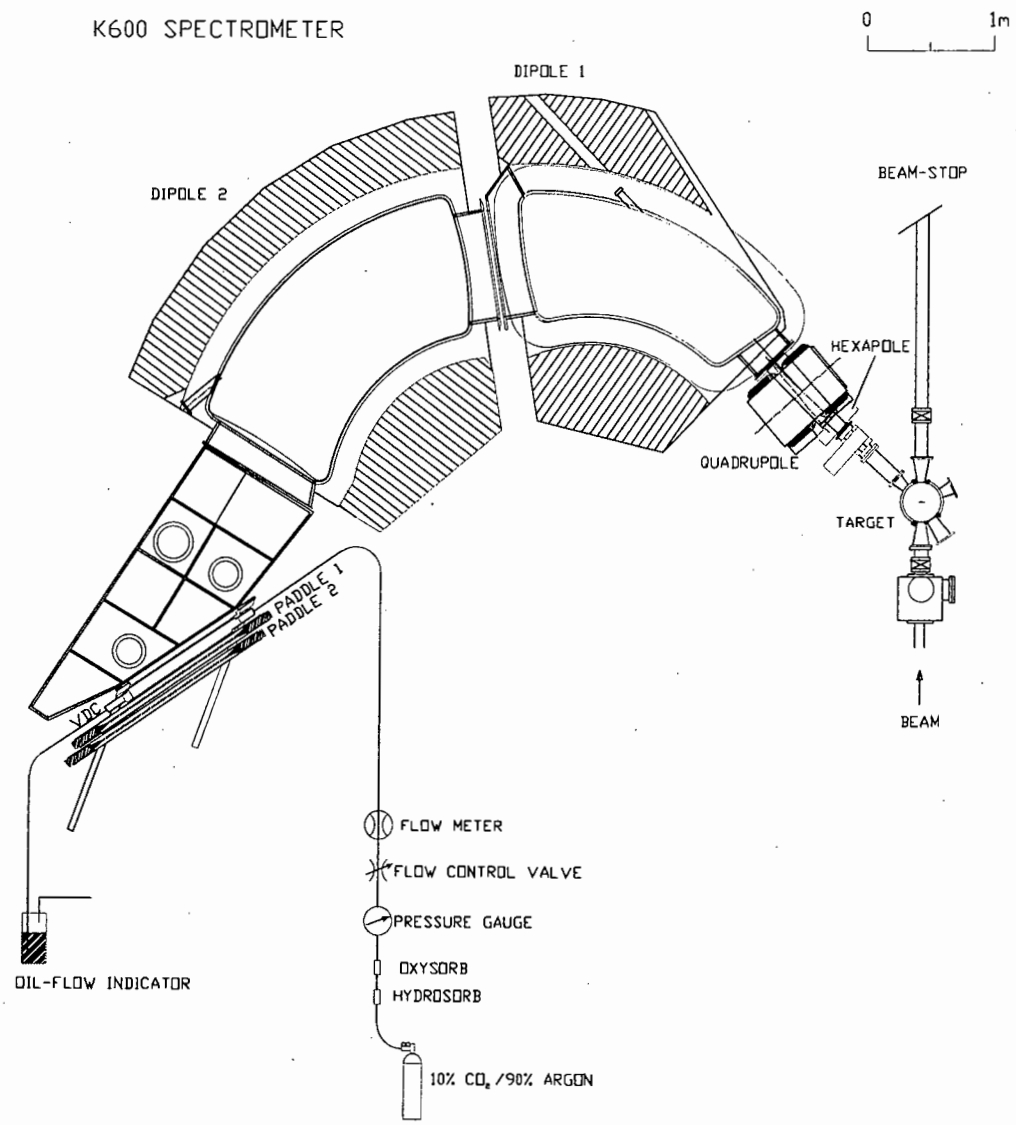

Figure 2.3: *Positioning of the spectrometer focal-plane detectors. A schematic representation of the VDC gas-handling system is also shown.*

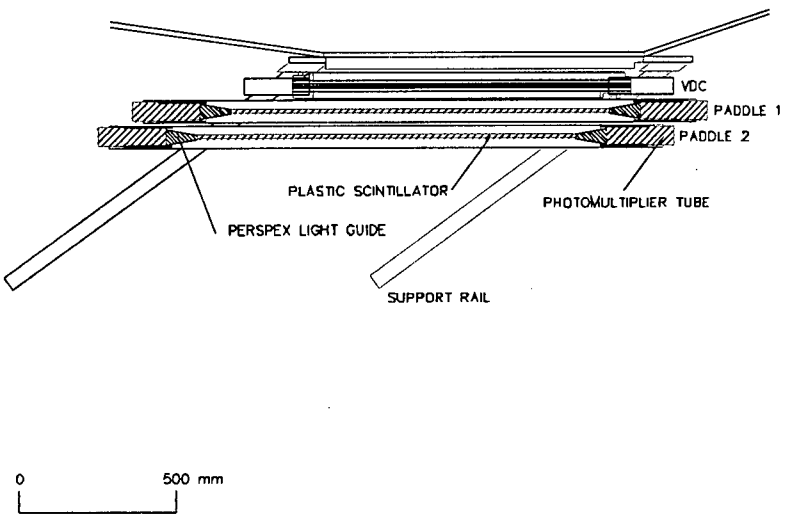

Figure 2.4: *Magnified view of the focal-plane detector array arrangement.*

momentum dispersion focal plane of the spectrometer on steel support rails (see figures 2.3 and 2.4).

Vertical Drift Chamber

The VDC[6] used in this work was designed and built by NAC personnel. It comprises, *inter alia*, two high voltage (HV) anode planes, an earthed signal-wire cathode plane situated midway between the cathodes and a gas which fills the VDC volume. Two 25 μm thick Mylar windows are used to seal off the gas-filled VDC interior from the environment, while two 27 μm thick aluminium foils separated by 16.0 mm are used as cathode high voltage planes (see figure 2.5). The earthed signal wire-plane situated midway between these foils comprises 198 signal wires, each 25 μm thick, and spaced 4.0 mm apart. In order to improve the field shaping and facilitate the application of lower high voltages on the cathode planes, these wires are interspersed with 199 guard wires, each of thickness 50 μm and also positioned 4.00 mm apart. All wires used were made from gold-plated tungsten. Negative high voltages of 3.50 kV and 550 V are applied to the cathode planes and guard wires respectively. A 90%Ar/10%CO_2 gas mixture at atmospheric pressure is used as a VDC fill gas. The gas is supplied to the VDC by means of the gas-handling system shown schematically in figure 2.3. Under the above operating conditions the position accuracy, σ_x, achieved with the VDC was 81 μm (see appendix A).

The VDC is positioned flush up against a 75 μm thick Kapton window on the exit-flange of the spectrometer vacuum chamber. It was arranged in a way such that its wire-plane coincides with the spectrometer's focal plane which is at an angle $\theta_{\text{f.p.}} = 35.75°$ with respect to the central-momentum trajectory through the spectrometer (see figure 2.6). This angle was determined via three-dimensional ion-optical simulations using the computer program TRACK [Geo91] which utilizes calculated three-dimensional median-plane field maps[7] associated with the spectrometer magnets [NAC94]. A schematic

[6]For a detailed overview of the principles of drift chambers, the reader is referred to [Sau77] and references therein.

[7]These maps were generated from the measured two-dimensional median-plane field maps using the computer program NACCON developed at the NAC.

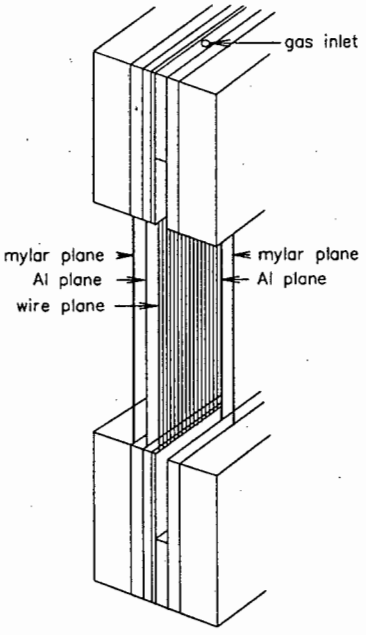

Figure 2.5: *Schematic cross-sectional view of the VDC used.*

representation of a charged particle traversing a VDC is shown in figure 2.7. The particle ionizes gas molecules along its path through the VDC. Because of the applied potential difference, electrons generated by the ionization drift at nearly constant velocity[8] to within less than 1 mm of the signal wires, whereupon avalanching [Cha84] occurs. As a result, pulses are induced on the signal wire. By measuring the time it takes for these electrons to drift from the point of primary ionization to the point where avalanching occurs, and by making use of a mapping from drift time to drift distance, it is possible to reconstruct the particle's in-plane trajectory through the VDC (see section 2.8, appendix A and appendix C). The position where the particle's trajectory crosses the focal plane can therefore be determined and hence the particle's momentum calculated.

Paddles

Pulses from the plastic scintillation detectors mounted behind the VDC were used to generate an event trigger and a start signal for the measurement of the time-of-flight of particles through the spectrometer. In the following, the paddle scintillation detector which was located behind the VDC relative to particles moving through the spectrometer will be labelled paddle 1; and the following one will be labelled paddle 2 (see figure 2.4). Both paddles were constructed using plastic scintillator (Bicron BC408) with a rectangular cross section of 122.0 cm $\times$ 10.2 cm. The scintillator thicknesses for paddles 1 and 2 are 3.18 mm and 12.70 mm respectively. Silgel (NE586) was used to link two fishtail perspex lightguides to each end of the scintillators. The same compound was used to couple photomultiplier tubes (Hamamatsu R329) to each lightguide. Hamamatsu E934 bases are used on all photomultiplier tubes, each being magnetically shielded with a mu-metal shield. The assembled paddles are mounted inside black paper-covered rectangular frames in order to make them light-tight and positioned directly behind the VDC. Both paddles were operated at a negative high voltage of $\sim$ 1500 V.

[8]The inverse drift velocity for the VDC used is $\sim$ 18 ns/mm.

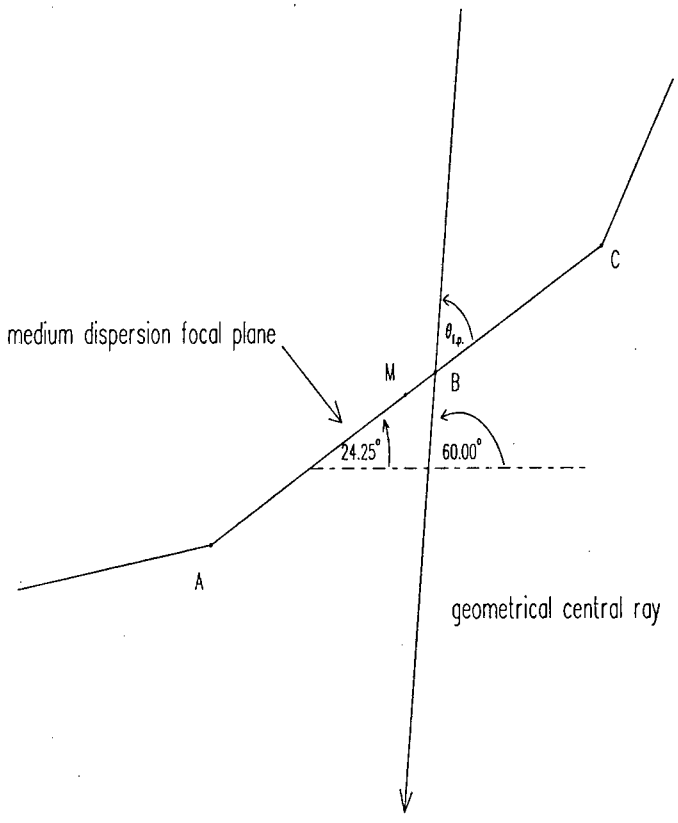

Figure 2.6: *Schematic representation of the positioning of the VDC w.r.t. the k = 600 spectrometer's central-momentum trajectory. The distances between points* **A** *and* **B**; **B** *and* **C**; *and,* **M** *and* **B** *are 535.54 mm, 498.82 mm and 18.36 mm respectively. Point* **M** *is located midway between points* **A** *and* **C**.

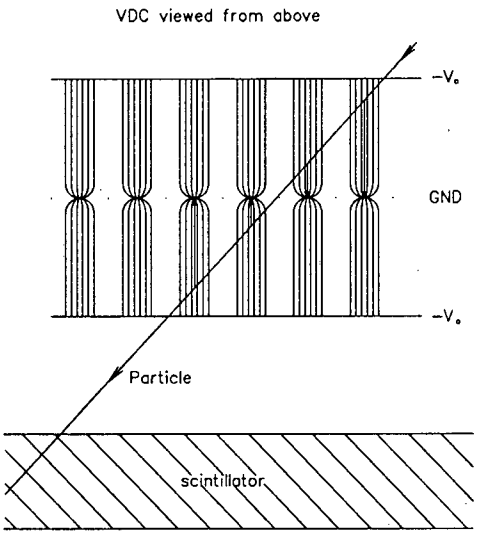

Figure 2.7: *Schematic top-view of a charged particle's trajectory across the VDC and a plastic scintillator.*

2.3.2 Angle modes

The spectrometer angle can be set to a precision of 0.1° using a scale on the spectrometer vault floor. It is estimated that the uncertainty in the spectrometer angle, primarily due to uncertainty in the beam direction, was 0.25°. Data were collected at spectrometer laboratory angles, θ, in the 6°–48° region at 2° intervals. Since the beam-pipe from the scattering chamber to the external beam-stop (Faraday cup) prevented the spectrometer from reaching angles less than 18°, a beam-stop had to be located inside the scattering chamber in order to make measurements in this angular region[9]. The spectrometer was therefore operated in a normal-angle mode ($\theta \geq 18°$) and small-angle mode ($\theta \leq 18°$).

While acquiring data in the normal-angle mode the standard external beam-stop arrangement shown in figure 2.3 was used. When the spectrometer was operated in the small-angle mode, two different internal beam-stop configurations were used. In the first, used for $12° \leq \theta \leq 18°$, a graphite block placed inside the scattering chamber served as a beam-stop (see figure 2.8). In the second configuration, used in the $6° \leq \theta \leq 12°$ angular

[9]This resulted in high backgrounds inside the scattering chamber which made the use of a monitor detector to check the consistency of the beam-current integration impossible.

region, the beam-pipe extending from the scattering chamber to the external beam-stop was removed, thereby allowing the spectrometer to reach further forward angles. In this case the beam was stopped on a graphite block placed inside an evacuated chamber located behind the scattering chamber as shown in figure 2.9.

2.3.3 Collimators

The spectrometer acceptance was defined by brass collimators having the shape shown in figure 2.10. Two collimators were used[10]; one for $\theta \geq 12°$ and the other for $\theta \leq 12°$. The former collimator, which was located inside the collimator carousel shown in figure 2.8, had the dimensions shown in figure 2.10. These dimensions were chosen so as to maximize the solid angle, minimize the kinematic spread due to the in-plane angular acceptance but yet yield 100% transmission through the spectrometer (see appendix D for a study of the spectrometer's transmission). The second collimator, which was located further down-stream (see figure 2.9) had its dimensions scaled in order to give the same solid angle as that associated with the first. The distances from the target centre to the back of the two collimators were 735.5 mm and 545.0 mm respectively. The arrangements resulted in horizontal angular acceptances of 1.09° and 1.07° respectively; while the vertical angular acceptances were 4.28° in both cases. The solid angle subtended by both collimators was 1.34 msr.

2.4 Targets

Since manganese is not self-supporting it is usually deposited onto a backing when making targets (for example, [Mat68, Pee74, Cam81]). A backing made of Mylar was used in this work because of its robustness. Two ^{55}Mn targets were manufactured at the Van de Graaff facility at the NAC for use in this experiment. These targets were made under vacuum by evaporating 99.99% pure[11] Mn onto a 1.5 μm thick Mylar backing.

[10] See figure F.6 of appendix F for the results of a consistency check regarding the use of these two collimators.

[11] The natural isotopic abundance of ^{55}Mn is 100%.

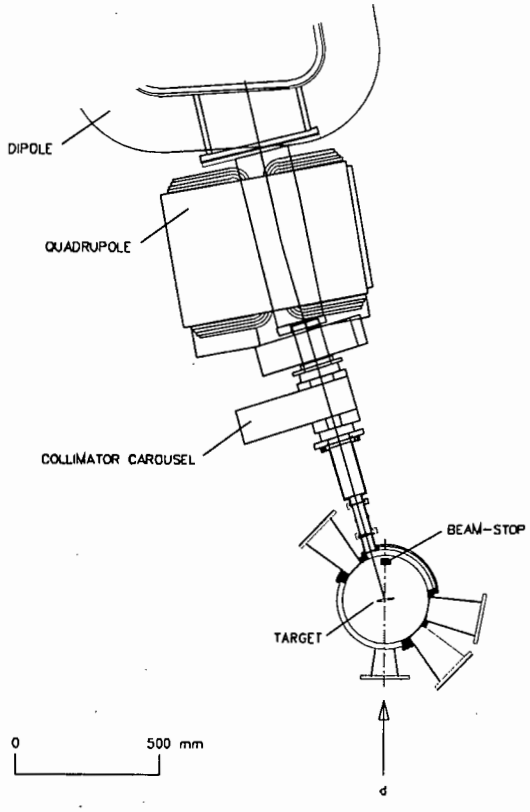

Figure 2.8: *Beam-stop configuration used in the spectrometer's small-angle mode for 12 ° $\leq \theta \leq$ 18 °.*

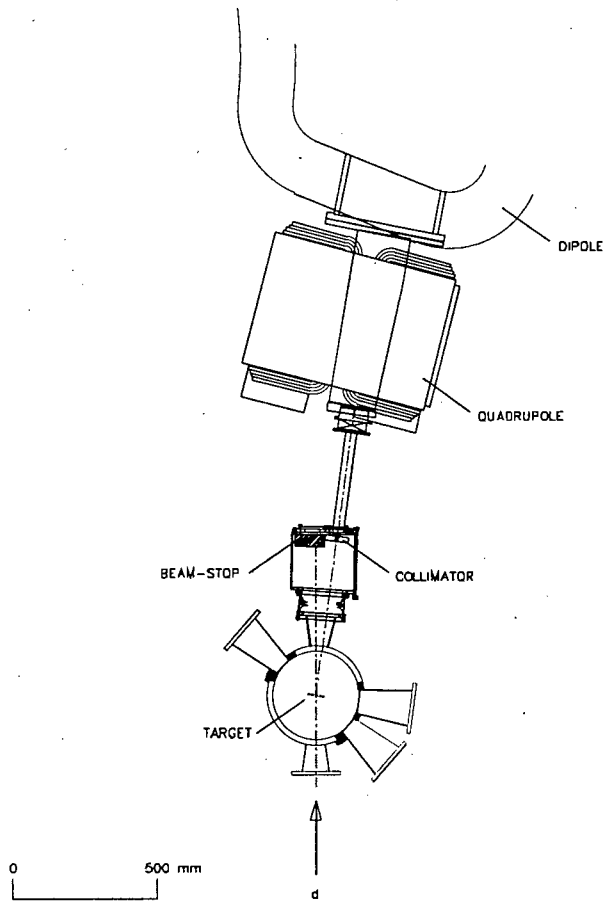

Figure 2.9: *Beam-stop configuration used in the spectrometer's small-angle mode for* $6\,^{\circ} \leq \theta \leq 12\,^{\circ}$.

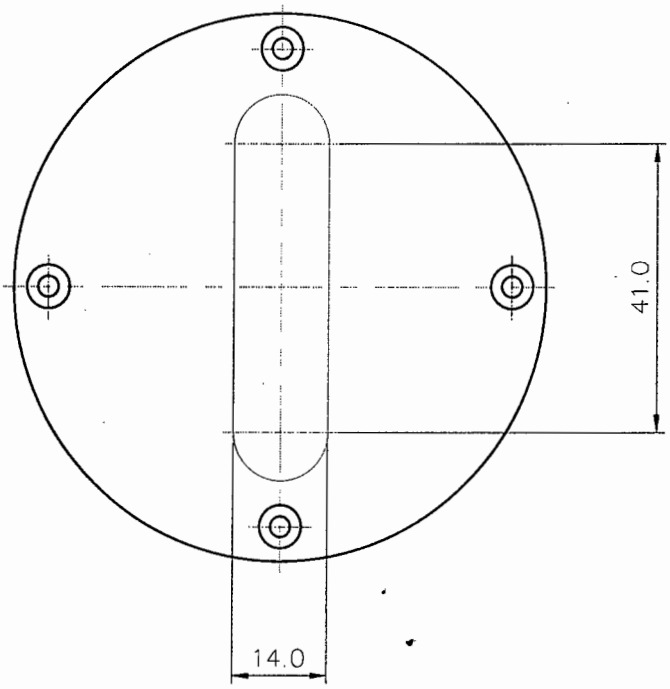

Figure 2.10: *Drawing of brass collimator used to define the spectrometer acceptance. The dimensions shown are for the collimator used for* $\theta \geq 12$ °. *All dimensions shown are in mm.*

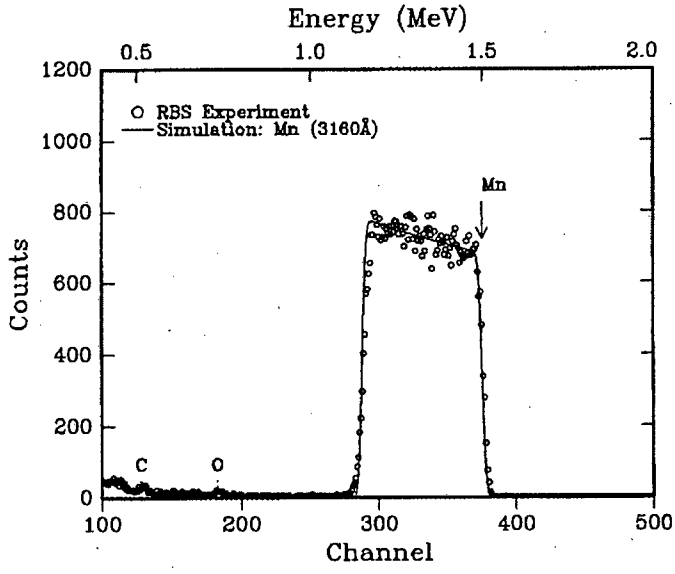

Figure 2.11: *RBS spectrum, obtained using a 2 MeV α beam, associated with one of the Mn targets used. The expected locations of a few common elements assuming that they are present at the surface of the target are shown. The solid line is a RUMP [Doo85] simulation of the spectrum for a layer of ^{55}Mn having a thickness determined as described in the text.*

target no.	experimental session	Mn layer thickness (Å)	(μg/cm^2)
1	December 1991 - December 1993	2132	159
2	January 1993 - September 1994	3160	235

Table 2.2: *Manganese layer thicknesses associated with the two targets used. The maximum uncertainty associated with the quoted thicknesses is 10% (see text for details).*

A rough estimate of the thickness of the Mn layer deposited onto the Mylar was obtained using a quartz crystal film-thickness and deposition rate-meter (Inficon XTM). A more accurate measurement of the Mn layer thickness was made using Rutherford backscattering spectrometry (RBS) [Chu78]. A 2 MeV α beam and a standard experimental arrangement [Cha93, Mar93] were used to perform RBS on the two targets at the Van de Graaff facility. A backscattering angle of 170° was used. The RBS spectra collected were analysed off-line using the Rutherford backscattering Utilities and Manipulation Program (RUMP) [Doo85], a standard software package for analysing RBS spectra. RUMP was used to determine[12] thicknesses of Mn layers from the the full-width at half maximum (FWHM) of the ^{55}Mn peaks observed in the RBS spectra. The limiting factor on the accuracies of thicknesses determined in this manner, is the 5–10% accuracy associated with the stopping power tables used by RUMP. The RBS spectrum associated with one of the manufactured targets is shown in figure 2.11. A RUMP simulation of the expected spectrum assuming that the target comprises only a Mn layer of thickness determined in the manner described above, is also shown in this figure. The thicknesses so obtained are given in table 2.2.

Targets were mounted in the scattering chamber on a target ladder which was linked to a remote target-positioner. The target angle was always set to half the spectrometer angle in order to fix the target transformation factor[13] [Hen74] to a value of 1.0 as is common practice. On the ladder

[12]In particular the *width-thick* function, which is based on the mean-energy approximation for the stopping power, was used.

[13]This factor is given by $t_{11} = \frac{cos(\theta-\phi)}{cos\phi}$, where ϕ is the target angle.

was a ^{55}Mn target, an aluminium oxide viewer-target used for beam-spot alignment, an empty target frame for beam-halo reduction and a 1.5 μm thick Mylar target used for background checks. Care was taken to mount the Mn target with the Mylar backing facing the beam in order to minimize the deterioration in the spectrometer resolution.

2.5 Trigger logic

Since both pickup and elastic scattering data were required, the spectrometer had to be operated in two modes. These will be referred to below as the (d,^{3}He)- and (d,d)-modes respectively. Calculations of the energy lost by the helions and deuterons in the materials constituting the focal-plane detectors (given in table 2.3) were performed in order to decide on the trigger logic required for the (d,^{3}He)- and (d,d)-modes respectively.

For an assumed deuteron beam energy of 45 MeV, the lowest energy helions of interest (i.e. those associated with an excitation energy of 6 MeV in ^{54}Cr at a spectrometer angle of 48°) are stopped 0.2 mm inside[14] the scintillator of paddle 1. Each of these helions deposit 9.2 MeV in this scintillator. The corresponding highest energy helions of interest (i.e. those associated with the transition to the ^{54}Cr(g.s.) at $\theta = 6°$) are stopped 0.8 mm inside[15] paddle 1's scintillator where they each deposit 27.1 MeV. Since no thinner scintillator was available, the paddle 1 signal, P_1, was used in anti-coincidence with the paddle 2 signal (P_2) to generate an event trigger while operating in the (d,^{3}He)-mode. In order to minimize the data buffered to tape for off-line analysis in this mode, a VDC "or"-box was used. This module, which was designed and built at the NAC, generates a logic signal, O_V, whenever one or more VDC signal wires register a hit. A (d,^{3}He)-mode event trigger was therefore generated only when P_1, $\overline{P_2}$ and O_V signals were in coincidence. It was found that by including the O_V signal in the trigger

[14]The angle of the helion trajectory w.r.t. the focal plane was assumed to be 32.8°, i.e. the minimum value expected from ion-optical simulation of trajectories through the spectrometer (see appendix B).

[15]The angle of the helion trajectory w.r.t. the focal plane was assumed to be 40.1°, i.e. the maximum value expected from ion-optical simulations of trajectories through the spectrometer (see appendix B).

material	thickness (mm)
Kapton	0.075
air	20.0
Mylar	0.025
Ar/CO_2	8.0
aluminium	0.027
Ar/CO_2 gas	16.0
aluminium	0.027
Ar/CO_2 gas	8.0
Mylar	0.025
air	20.0
paper	0.235
air	20.0
aluminium	0.027
plastic scintillator	3.18
aluminium	0.027
air	20.0
paper	0.235
paper	0.235
air	20.0
aluminium	0.027
plastic scintillator	12.70
aluminium	0.027
air	20.0
paper	0.235

Table 2.3: *Details of materials constituting the array of focal-plane detectors. Materials are listed in order from the Kapton foil on the exit flange of the spectrometer vacuum-chamber to the layer of paper on the back of the paddle 2.*

spectrometer mode	trigger logic
(d,d)	$P_1 \cdot P_2$
$(d,^3\mathrm{He})$	$P_1 \cdot \overline{P_2} \cdot O_V$

Table 2.4: *Trigger logic used when acquiring proton pickup and deuteron elastic scattering data. P_1 and P_2 are the signals associated with paddle 1 and paddle 2 respectively while O_V is the signal associated with the VDC "or"-box used.*

logic, a 40% improvement in the signal-to-noise ratio was obtained without giving rise to a statistically significant variation in helion yield.

Using the same assumed beam energy and trajectory geometry as above, the lowest and highest energy deuterons of interest are found to have ranges of 2.0 mm and 3.7 mm respectively inside the scintillator of paddle 2. These deuterons deposit energies of 17.1 MeV and 25.0 MeV respectively in the scintillator. For the (d,d)-mode, therefore, an event trigger was generated whenever a P_1 signal was coincident with a P_2 signal. The coincidence requirement resulted in relatively good signal-to-noise ratios which obviated the need for the "or"-box. The trigger logic used in conjunction with the two spectrometer modes is summarized in table 2.4.

2.6 Particle identification

2.6.1 $(d,^3\mathrm{He})$-Mode

The helions of interest are expected to have a kinetic energy of about 39 MeV[16]. Table 2.5 shows the other particles with the same energy constant (k) as these helions. Energy-loss calculations show, that of the latter, only 29 MeV protons, 15 MeV deuterons and 10 MeV tritons should reach the scintillator of paddle 1. Four time-of-flight (TOF) peaks were therefore expected when operating the spectrometer in the $(d,^3\mathrm{He})$-mode.

The minimum and maximum flight-paths from target to focal plane associated with the spectrometer's effective momentum-acceptance and in-plane angular acceptance were obtained by means of ion-optical simulations

[16]For an assumed beam energy of 45 MeV and a spectrometer angle of 18°.

particle	kinetic energy (MeV)
p	29
d	15
t	10
α	29

Table 2.5: *Kinetic energies of other particles having the same energy constant, k, as that of a 39 MeV helion.*

(see appendix B). The simulated trajectories are shown in figure 2.12. The 788 cm and 887 cm flight-paths[17] found to be associated with the extreme trajectories were used to calculate the corresponding extreme times-of-flight for the helions, protons, deuterons and tritons respectively from the target to the focal plane. The results of these calculations (see figure 2.13) show that the helion peak is well separated from the others on an absolute time scale. A typical (relative[18]) TOF spectrum acquired in the (d,^{3}He)-mode is shown in figure 2.17(a). By assuming a location of the helion TOF peak, the location of the proton, deuteron and triton peaks can be predicted using knowledge of the beam-burst interval ($\sim$ 100 ns for this study) and the results summarized in figure 2.13. Excellent correspondence was found between prediction and experiment as is shown in figure 2.17(a). The helion, proton, deuteron and triton peaks are clearly seen. The additional structure observed in this spectrum is thought to be associated with the beam-stop. Since the helion peak could be identified and did not overlap with any other peaks, it was not necessary to understand this additional structure in detail. The helions of interest in the (d,^{3}He)-mode could therefore be selected by setting a software gate on the TOF spectrum.

[17]The dependence of flight-paths on the vertical dimension was estimated from figure D.1 (see appendix D) to be negligible.

[18]Timing start- and stop-signals were derived from the paddle- and the cyclotron RF-signals respectively as detailed in section 2.7.

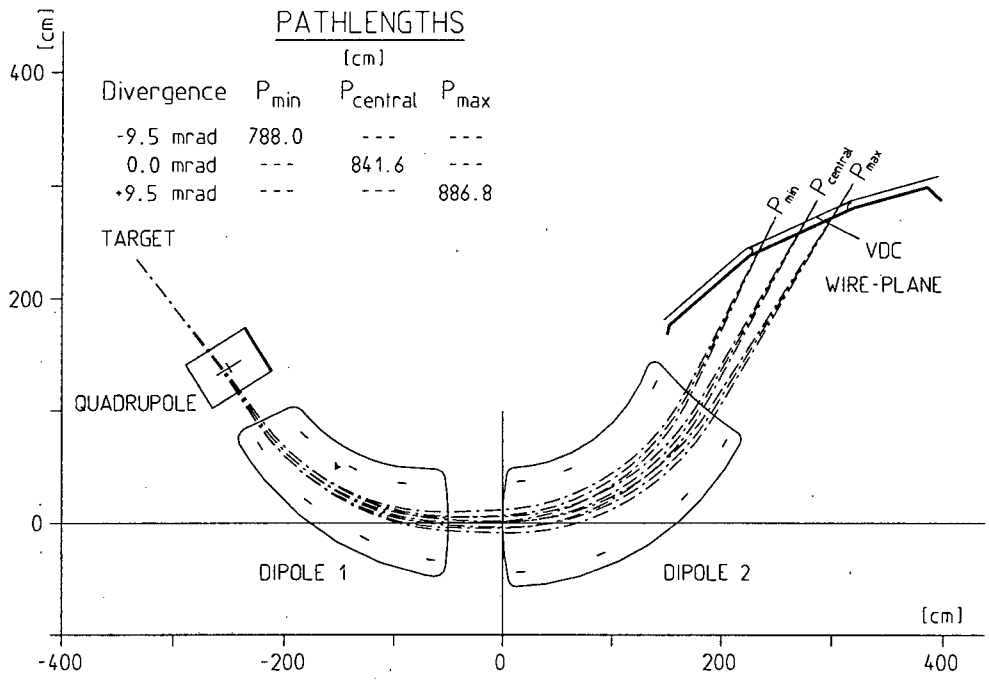

Figure 2.12: *Simulated trajectories through the NAC k = 600 spectrometer. The pathlengths from target to focal plane associated with the minimum-, maximum- and central-momentum trajectories through the spectrometer are shown. The simulations were made using the computer program TRACK [Geo91].*

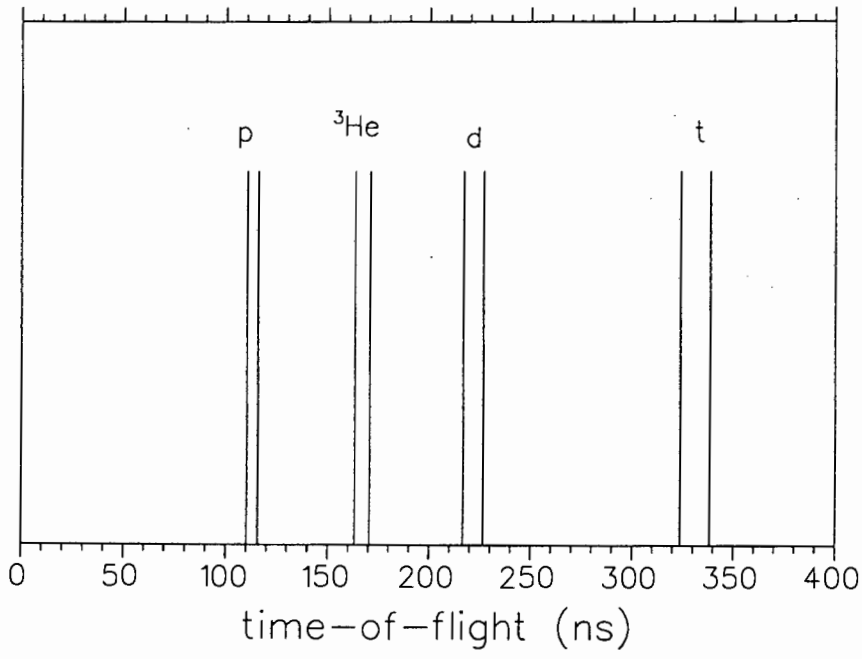

Figure 2.13: *Predicted absolute time-of-flight spectrum (from target to focal plane) for the (d,^{3}He)-mode showing the expected locations and widths of the peaks for helions, protons, deuterons and tritons having the kinetic energies shown in table 2.5.*

particle	kinetic energy (MeV)
p	88
t	29
^{3}He	117
α	88

Table 2.6: *Kinetic energies of particles having the same energy constant, k, as that of a 44 MeV deuteron.*

2.6.2 (d,d)-Mode

For an assumed beam energy of 45 MeV the elastically scattered deuterons of interest have a kinetic energy of about 44 MeV. The other particles with the same energy constant as a 44 MeV deuteron are listed in table 2.6. Protons, ^{3}He and α particles which have the same k value as a 44 MeV deuteron are kinematically not allowed assuming they are produced by deuterons interacting with ^{55}Mn or the constituent nuclei of Mylar. By considering only rigidity and kinematics it is possible for tritons with an energy of about 29 MeV to reach the focal plane along with the deuterons of interest. Energy-loss calculations show however that 29 MeV tritons will stop in the scintillator[19] of paddle 1. These tritons are therefore not expected to appear in the TOF spectrum since they would not satisfy the $P_1 \cdot P_2$ trigger logic used in the (d,d)-mode. A typical TOF spectrum acquired in (d,d)-mode, shown in figure 2.17(b), shows only the expected deuteron peak.

2.7 Electronics

Signals from the VDC and paddles were processed in the spectrometer vault (see figure 2.1), while the electronics used to measure the effective data acquisition deadtime, measure the integrated current and monitor the paddle rate for the beam-halo measurement were located in the NAC dataroom, where the data acquisition computer was located. In the main, commercially available electronic modules adhering to the Nuclear Instrument Module

[19]The tritons have a range of 2.6 mm in this scintillator where they deposit 24.9 MeV.

(NIM) and Computer Automated Measurement and Control (CAMAC) standards were used in the electronic set-up (see table 2.7).

2.7.1 Paddle signals

A block diagram of the electronics used to process signals associated with the paddles is shown in figure 2.14. The output pulse from each of the four photomultiplier tubes associated with the two paddles was fed into a linear fan-in/fan-out channel. One of the outputs associated with this channel, delayed by 100 ns, served as an input to an analogue-to-digital converter (ADC) which was located in one of the CAMAC crates in the spectrometer vault, while a second output served as the input to a constant fraction discriminator (CFD).

In order to get an accurate time-pickoff the two CFD outputs associated with each paddle were fed into a mean timer, and the output from there served as input to a discriminator. The width of the discriminator output pulse associated with paddle 1 was made narrow ($\sim$ 5 ns) while the corresponding pulse width for the paddle 2 pulse was set to 20 ns in order to pick the timing off the thinner paddle 1. In the (d,d)-mode the latter two pulses served as input to a four-fold logic unit (4FLU) where a paddle coincidence ($P_1 \cdot P_2$) pulse was generated as the event trigger[20].

In the (d,^{3}He)-mode the P_1 and $\overline{P}_2$ paddle pulses along with the output pulse from the VDC "or"-box, O_V, were instead sent to this 4FLU, enabling the ($P_1 \cdot \overline{P}_2 \cdot O_V$) logic pulse to be generated as the event trigger in this mode. One of the outputs from this 4FLU was fed to a discriminator from which an event trigger for the CAMAC event trigger module (ETM)[21], an ADC gate (for the paddle pulse heights) and the experimental common stop signal for time-to-digital converters (TDC) (which digitized the VDC drift times) were derived. A further output channel from the 4FLU served as the start signal for a TDC which measured the time-of-flight of rigidity-selected particles through the spectrometer. The stop signal for this TDC was generated by another 4FLU channel which was operated in two-fold

[20]The generation of an event trigger was vetoed by the VDC-associated electronics (detailed in section 2.7.2) in the manner shown in figure 2.14.

[21]Not shown in figure 2.14.

module	model
analogue-to-digital converter (ADC)	LeCroy 2249A
CAMAC crate controller (CC)	Hytec 1180 (crate CCA2)
CAMAC current integrator interface	EDA14-5 (NAC)
CAMAC differential branch extender	Hytex 6501A
CAMAC event trigger module (ETM)	EDA10 (NAC)
CAMAC scaler	Kinetic Systems 3615 Hex Counter
constant fraction discriminator (CFD)	Ortec 934
current integrator	Brookhaven Instruments Corporation 1000c
discriminator	Phillips 711 or LeCroy 821
four-fold logic unit (4FLU)	LeCroy 365AL
gate-and-delay generator (GDG)	Ortec 416A
LED counter	Ortec 875
level adapter (LA)	LeCroy 688 AL
log/lin ratemeter	Ortec 449-2
logic fan-in/fan-out (FIFO)	LeCroy 429A
mean-timer	LeCroy 624
paddle high voltage (HV) supply unit	Ortec 456
time-to-digital converter (TDC)	LeCroy 2228A
timer	Ortec 719
timing single channel analyser (TSCA)	Ortec 551
VDC high voltage supply unit	F.U.G. HCN 35-12500
VDC preamplifier/discriminator (A/D)	LeCroy 2735
VDC time digitizer module (TDM)	LeCroy 4291B
VDC dedicated crate controller (DCC)	LeCroy 4298
VDC DATABUS interface module (DIM)	LeCroy 4299
VDC threshold supply module	EDA47 (NAC)

Table 2.7: *Electronic modules used to process signals associated with the paddles, VDC, beam current integration, deadtime measurement and the CAMAC system.*

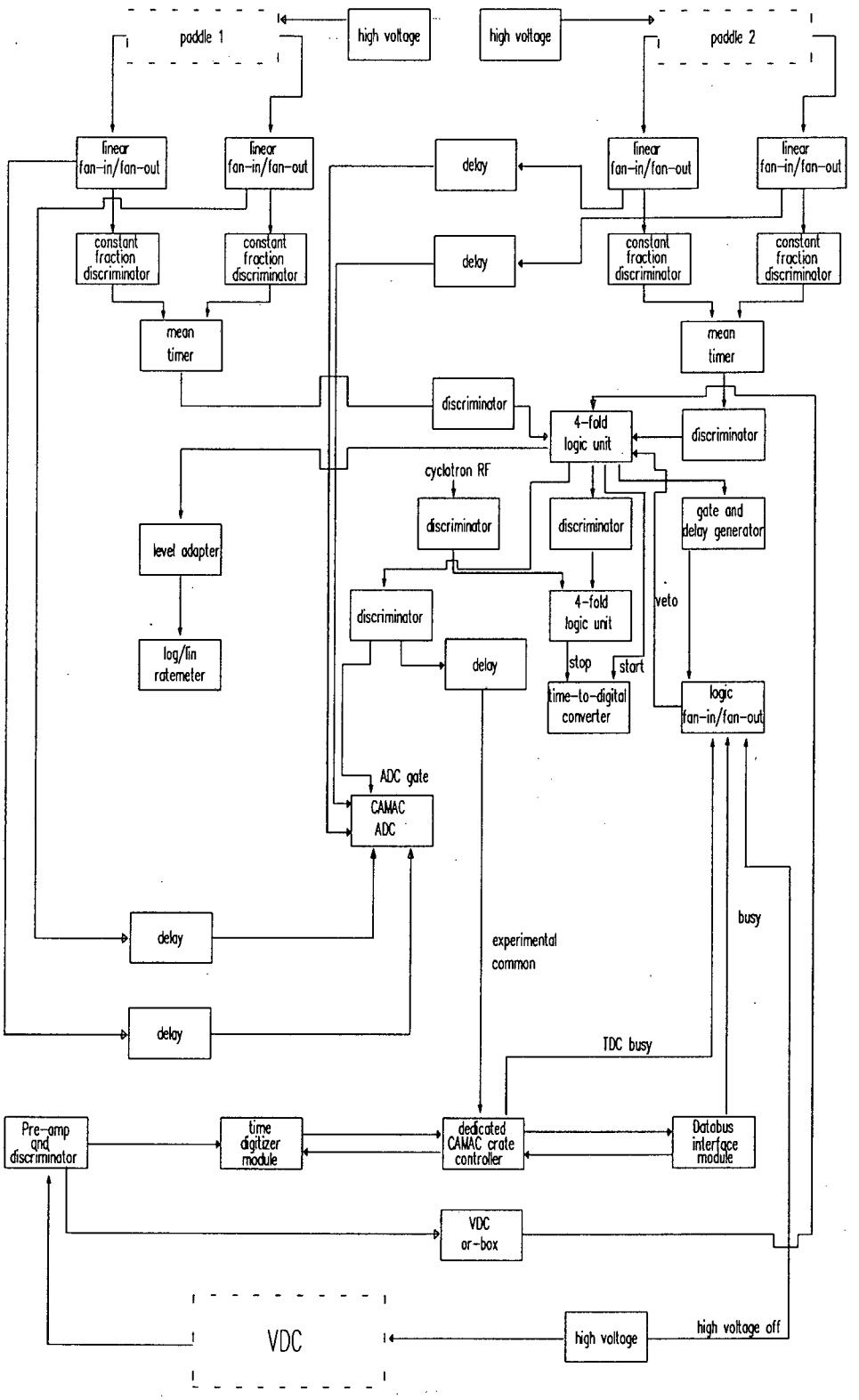

Figure 2.14: *Schematic representation of the electronics used to process the paddle and VDC signals.*

coincidence mode. The first input to this 4FLU was a discriminated $P_1 \cdot P_2$ or $P_1 \cdot \overline{P}_2 \cdot O_V$ pulse, depending on the spectrometer mode used. The second input was generated by attenuating and discriminating the cyclotron RF signal. In effect, a TDC (TOF) stop was only produced when an RF signal was coincident with an event trigger.

The monitoring of the paddle rates, required for checking the beam halo on target, was achieved by feeding the paddle coincidence (d,d)-mode or anti-coincidence (d,^{3}He)-mode signal from the spectrometer vault to the dataroom where it served as input into a level adapter, the output of which was fed into a ratemeter.

2.7.2 VDC signals

The VDC signals were processed by means of a dedicated CAMAC data acquisition system (LeCroy 4290) which is used to handle data associated with multiwire drift chambers. The system comprised 16-channel VDC-mounted preamplifier/discriminator (A/D) cards, 32-channel drift chamber time digitizer modules (TDM), a dedicated CAMAC crate controller (CC) and DATABUS interface/buffer module (DIM). A schematic diagram of the VDC electronics are also shown schematically in figure 2.14.

Each signal[22] from the A/D card served as an input to a channel on a TDM, each occupying a single slot in the CAMAC crate. A total of seven of these modules were used in order to process the pulses from the VDC's 198 signal wires. In the crate used to house the TDMs there was a dedicated crate controller (DCC), which amongst other operations, pre-processed TDM outputs, rejecting unwanted zero or full-scale values during data acquisition. The TDMs were operated in common stop mode which was selected by a side-panel switch on the DCC. In this mode the timing cycle was started on receipt of a wire signal and stopped on receipt of an experiment common trigger which was obtained by delaying by 500 ns the output pulse from the 4FLU, which generated the event trigger as described above. Valid data from the DCC were transferred by means of a fast bi-

[22]Thresholds in 0.0–0.7 V region could be set on A/D cards by means of a threshold supply module (see table 2.7) which was designed and built by the NAC electronics staff. The threshold was 0.25 V during data acquisition.

directional DATABUS to the memory (4K × 16 bit) of the DIM located in a slot of an adjacent CAMAC crate which housed a standard CC.

2.7.3 Beam-current integration

The electronics used to process pulses associated with the beam-current integrator system are shown schematically in figure 2.15. The current from the beam-stop was patched through to the dataroom where it was fed into the current integrator (CI). A thousand pulses per second are generated if this current equals the full-scale current setting on the CI. The digital output from the CI served as input into a timing single channel analyser, the output of which was in turn fed into a discriminator. One output from the latter formed the input to a CAMAC scaler module, while a second was sent to an identical scaler module which was inhibited by the busy signal from the CAMAC crates in the spectrometer vault. The latter scaler, in conjunction with the CI full-scale range setting, was used to calculate the integrated current corrected for the data acquisition deadtime. The full-scale range setting from the CI was fed into a CI CAMAC interface module, which was designed and built by NAC personnel.

2.7.4 Deadtime measurement

The deadtime of the data acquisition system was measured by using a pulser and two scalers. The electronics used are shown schematically in figure 2.15. The signal from an adjustable frequency pulser, which was constructed using a timer, served as the input to a discriminator. One of its outputs served as the uninhibited input to a CAMAC scaler module while a second output was fed into an identical CAMAC scaler which was inhibited by the busy signal associated with the focal-plane electronics. The number of inhibited and uninhibited pulses recorded by the two scalers were then used to determine the effective deadtime.

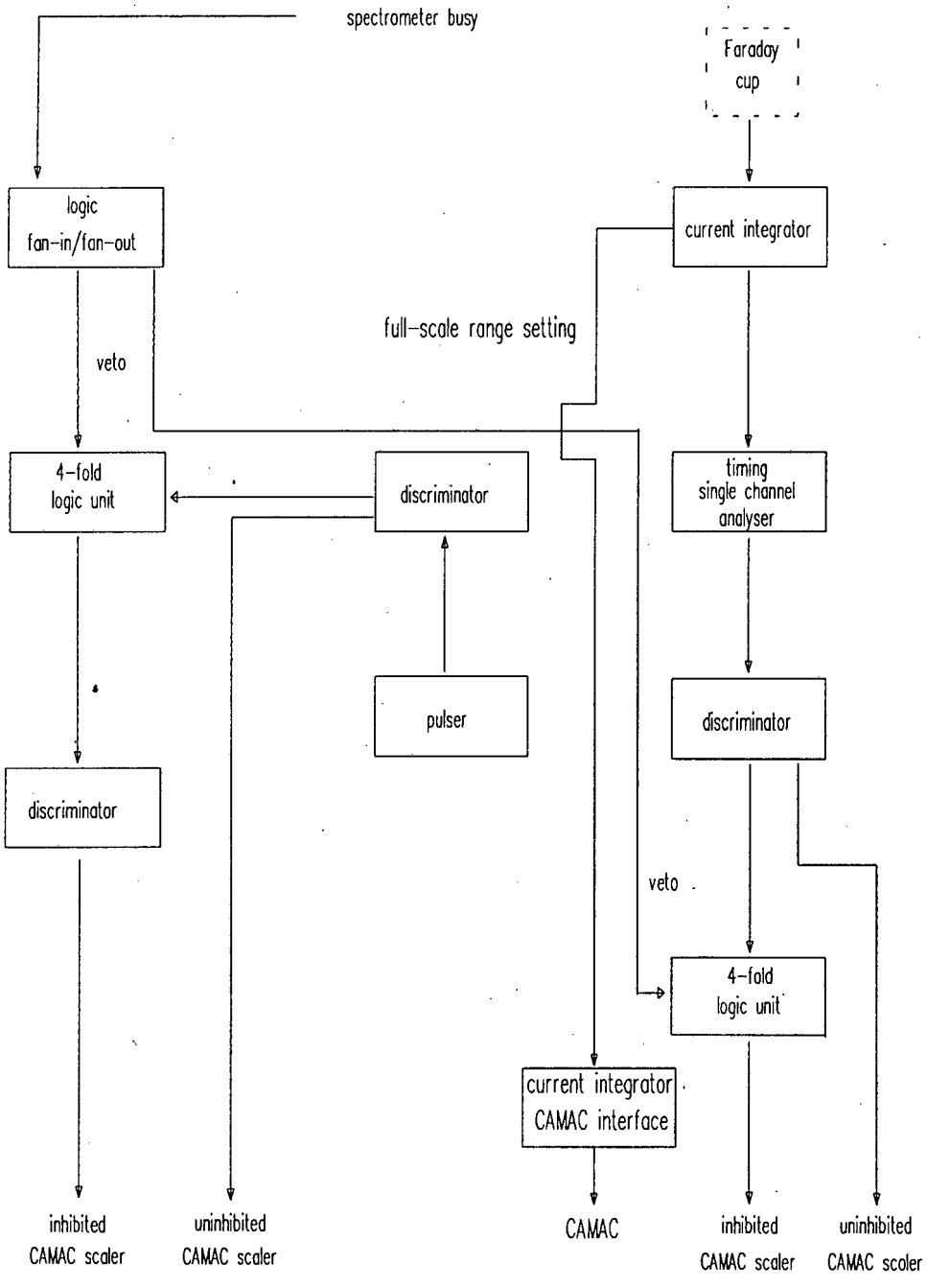

Figure 2.15: *Schematic representation of the electronics used to measure the effective deadtime and measure the integrated beam current.*

2.8 Data handling

The CAMAC system configuration comprised four crates, two of which were located in the dataroom, while a further two were in the spectrometer vault, linked to each other by means of a differential branch extender. The CAMAC branch highway, which linked the CAMAC crates, was interfaced to a VAX-11/750 (Digital Equipment Corporation) dedicated data acquisition computer by means of a BiRa microprogrammed branch driver (MBD).

The MBD is a 16 bit micro-computer which controls the flow of data and commands between the VAX and the CAMAC branch highway. It has a 430 ns instruction execution time and is capable of transferring data from the branch highway to the memory of the VAX via one of eight channels, each of which acts as a direct memory access device [Kin81, Pil89b, Pil92]. In this experiment two MBD channels were used. The first channel was used to transfer data relating to the VDC and paddles, while the second was used to transfer scaler data. On receipt of a CAMAC look-at-me (LAM) signal associated with one of the channels, a user-specified list of CNAF commands[23] was executed. These commands were downloaded to the MBD from the VAX in the form of a single re-entrant data acquisition program (DAP) which was custom-written for the CAMAC configuration used. The transfer of data associated with the MBD scaler channel was also controlled via CNAF commands in the DAP program. A software trigger, which was automatically generated by the VAX every ten seconds, initiated this transfer of data.

The data acquisition and analysis package, XSYS [Gou81, Gou83, Pil88, Pil92], which is a modular, structured system written to support the CAMAC branch highway and the MBD-11 branch driver, was used to process the acquired data. XSYS enables single or multi-parameter data to be acquired and manipulated according to the user's specifications and finally sorted into spectrum arrays. It consists of stand-alone FORTRAN subroutines which communicate with each other by means of two global sections of memory called XSCOM and XDATA. The former global section is the key

[23] *C*rate-slot*N*umber-sub*A*ddress- *F*unction.

XSYS data structure which contains control information, while the latter holds spectrum definitions and stores spectral data.

The data from the two MBD channels used were associated with a set of three data buffers in VAX memory. Buffers are filled by the code running in the MBD. As each buffer was filled the XSYS sorting process, XSORT, running on the VAX was signalled. While XSORT processed the data in a buffer, the MBD code started filling another buffer. As soon as XSORT had finished sorting all the events in a buffer, it in turn signalled the MBD code that the buffer was available again for receiving new event data. An algorithm programmed in the event analysis language (EVAL) is used by XSORT in the sorting of data into spectra, amongst other tasks [Hol81]. If writing to storage medium was enabled, the XSORT subprocess wrote the raw event buffers to a digital audio tape mounted on a tape drive which was accessed from the NAC local area network via an Infoserver 150 (Digital Equipment Corporation).

A schematic flow diagram showing how XSORT processed the data associated with a non-scaler event is shown in figure 2.16. The DIM word-count was first checked to see whether at least one VDC signal wire registered a hit[24]. If this was the case the spectrometer time-of-flight (TOF) spectrum was incremented. For every event that fell within the software gate set around the peak of interest in this TOF spectrum, the four paddle pulse-height spectra associated with the left and right photomultiplier tubes of paddles 1 and 2 were also incremented. A FORTRAN subroutine was then called from within the EVAL program to process data in the event buffer relating to the DIM. This subroutine determined which VDC wires registered hits and whether the number of wires that fired constituted an acceptable hit pattern (see appendix C). A second TOF spectrum was then incremented using data associated with the first TOF spectrum which corresponded to valid VDC events. Typical TOF spectra for the two reaction modes are shown in figures 2.17(a) and 2.17(b). For every valid VDC hit-pattern event, the subroutine discussed above passed drift times and associated wire numbers back to the EVAL program. These drift times

[24]This check was not necessary when analysing (d,^{3}He)-mode data because of the "or"-box used.

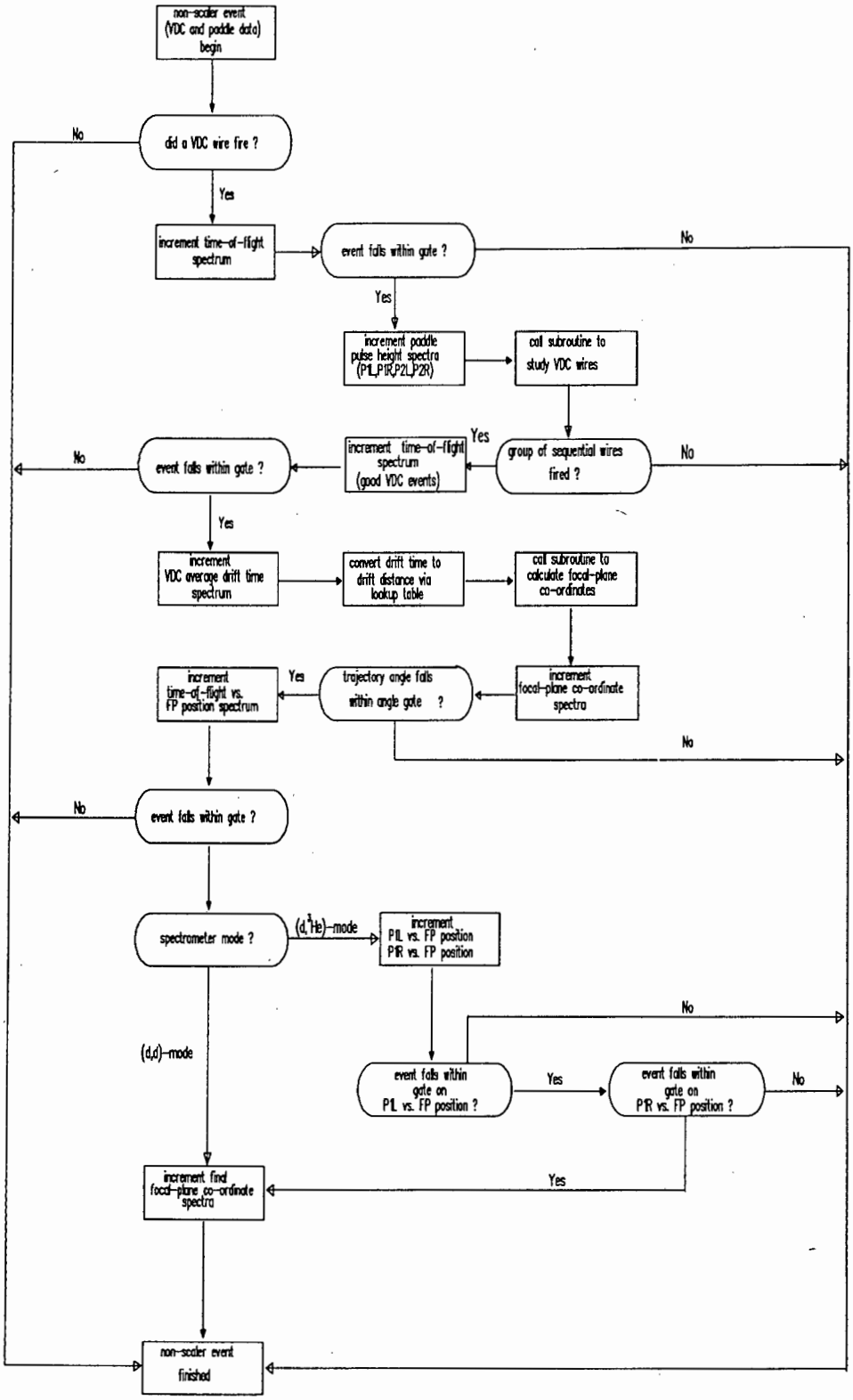

Figure 2.16: *Schematic representation of the event analysis language (EVAL) algorithm used by XSYS's sorting subprocess, XSORT, to process VDC and paddle data. PnL(R) denote the pulse height associated with left(right) photomultiplier of the n'th plastic scintillator paddle.*

were then converted to drift distances by using the integral-time-spectrum method [Bre74, Ber77, Hen87] which makes use of a lookup table.

The calculated drift distances and associated wire numbers were then passed to a second FORTRAN subroutine which calculated the focal-plane position and angle co-ordinates. These co-ordinates were determined by doing a linear least-squares fit to three data points which had as one co-ordinate the drift distance perpendicular to the VDC signal wire-plane, while the second was the distance along this plane (see appendix C). The calculated focal-plane co-ordinates were then used to increment the focal-plane position and angle spectra. In view of a poorer signal-to-noise ratio associated with the $(d,^3\mathrm{He})$-mode further software gates were implemented in order to improve this ratio. These software cuts are described in more detail in section 3.1.

2.9 Experimental procedure

At the start of each data acquisition session, the XSYS process was first initiated on the VAX. This entailed, *inter alia*, the execution of a command procedure which defined the XSYS spectra and allocated associated memory; followed by the loading of the EVAL and DAP programs. A lookup table, which was used to calculate focal plane co-ordinates as discussed above, was then read into memory. The lookup table was generated from the average VDC drift-time spectrum associated with inelastically scattered protons from the $^{12}\mathrm{C}(p,p')(\mathrm{E}^* \sim 30$ MeV) reaction at an incident energy of 66 MeV. This "white" spectrum[25] is shown in figure 2.18(a) while the corresponding lookup table generated from it is shown in figure 2.18(b).

In order to measure accurate relative drift times with the VDC it is necessary that all TDC channels associated with the TDM respond identically to a fixed time interval. In order to align[26] TDC values the DCC's Autotrim feature was used[27]. This feature makes use of a crystal-controlled time mark

[25] So termed because all VDC wires fire.

[26] This was necessary if the CAMAC crates in the spectrometer vault were off-line before the start of a data acquisition session.

[27] A threshold of + 0.7 V was used on all A/D cards during this procedure.

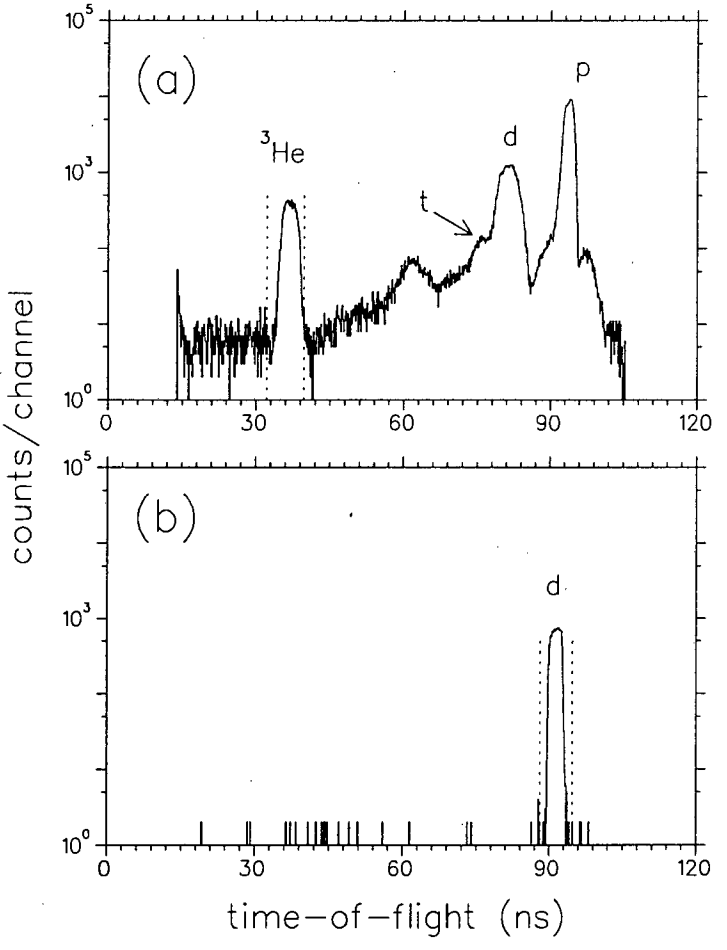

Figure 2.17: *Typical time-of-flight spectra associated with rigidity-selected reaction products that reach the spectrometer focal-plane detector array and result in a satisfactory VDC hit pattern. (a) Spectrum acquired in (d,^{3}He)-mode The predicted locations of the proton, deuteron and triton peaks are shown, along with the expected width of the helion peak. (b) Spectrum acquired in (d,d)-mode with the expected width of the deuteron peak shown.*

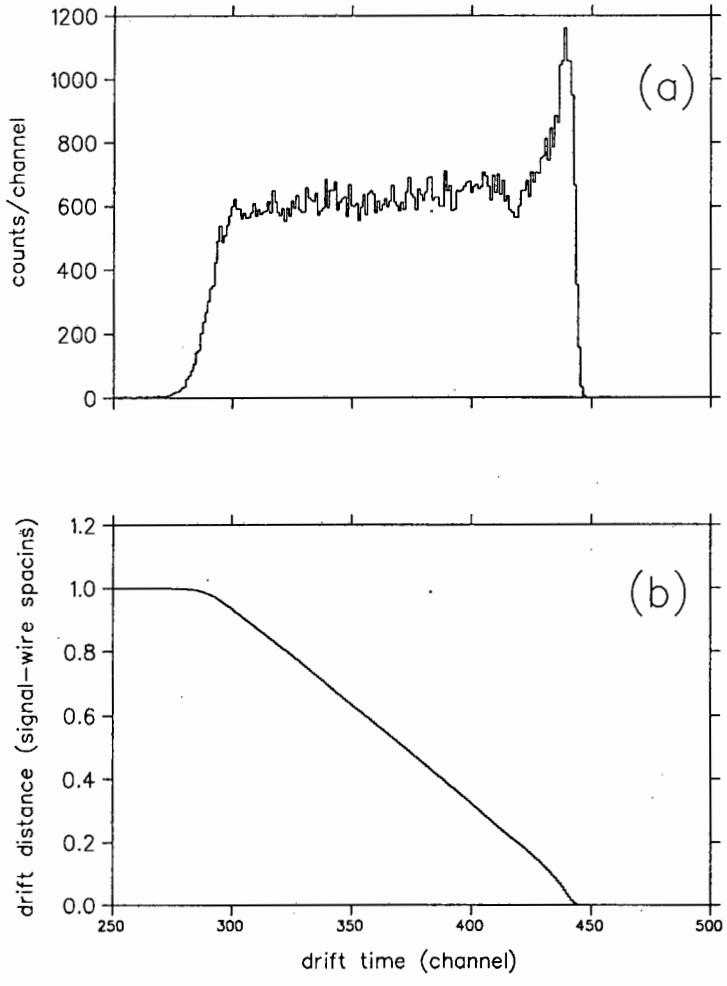

Figure 2.18: *(a) Typical "white" VDC average drift-time spectrum associated with inelastically scattered protons from the $^{12}C(p,p')(E^* \sim 30$ MeV) reaction at an incident energy of 66 MeV and spectrometer angle of 18°. One drift-time channel is equivalent to $\sim$ 0.9 ns. (b) The lookup table, which provides a mapping of drift time to drift distance, generated from the data shown in (a).*

generator to generate alternating zero- and full-scale TDC values which are used to trim the pedestals and gains of all the TDC channels to the same values. This procedure was implemented in a manner which calibrated out all variations in times due to variations in the VDC-mounted A/D cards and differences in the lengths of cables connecting these cards with the TDMs.

Preparations were then made to acquire (d,d)-mode data. This involved changing the event trigger logic to $P_1 \cdot P_2$ and setting the quadrupole and dipole magnetic fields such that deuteron trajectories associated with the ^{55}Mn(d,d)^{55}Mn(g.s.) reaction corresponded closely with the central-momentum trajectory through the spectrometer. The magnetic fields were set remotely from a PC in the dataroom which was connected to the NAC local area network. The required spectrometer magnet currents were calculated by means of a FORTRAN program which utilizes measured two-dimensional median plane field maps of the spectrometer's magnets to calculate the quadrupole and dipole currents necessary to cause a particle of a specific energy to travel along the central-momentum trajectory through the spectrometer. The paddle and VDC high voltages, and target angle were then set remotely from the dataroom. Once the beam was delivered to the spectrometer vault, the beam spot on target was optimized with the aid of the viewer-target and the halo reduced by monitoring the paddle rate (see section 2.2). The spectrometer resolution was then optimized by adjusting the spectrometer's K- and H-coil currents to cancel out the effect of kinematics [NAC92]. This was done with the aid of a two-dimensional correlation spectrum in which the deuterons' time-of-flight (TOF) through the spectrometer was plotted as a function of their position along the focal plane. With the resolution of the spectrometer optimized, it is expected that the focal-plane position of a peak should show no dependence on the associated TOF. In this case straight-line loci parallel to the TOF axis were expected. The effect of coil current adjustments on the TOF versus position spectrum is shown in figure 2.19. K- and H-coil currents were optimized by studying the expected locus of elastically scattered deuterons off ^{55}Mn. Deuteron scattering data were were then acquired using these coil currents. The duration of runs was typically twenty minutes.

The trigger logic was then changed to $P_1 \cdot \overline{P}_2 \cdot O_V$ and spectrometer fields

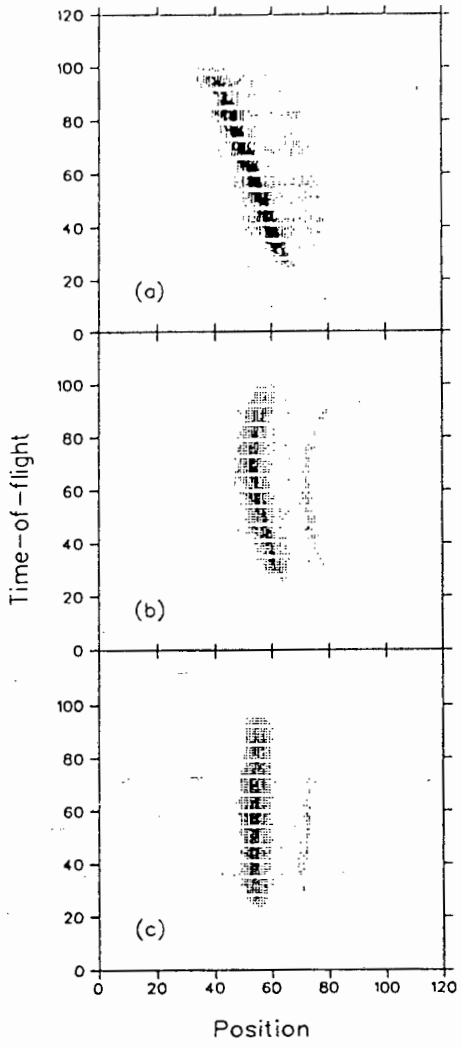

Figure 2.19: *Effect of adjusting the spectrometer K- and H-coils on the time-of-flight versus focal-plane position spectrum. (a) Case where the spectrometer needs a K-coil adjustment. (b) Case where spectrometer needs an H-coil adjustment. (c) Case where K- and H-coils are optimally adjusted. (Reproduced from Ref.[NAC94].)*

set to detect helions associated with the $(d,^3He)$-mode. Fields were set so that helions associated with a ^{54}Cr excitation energy of $\sim$ 3 MeV followed the central-momentum trajectory through the spectrometer. The total ^{54}Cr excitation energy range available with one setting of the spectrometer's magnetic fields in the $(d,^3He)$-mode was therefore $\sim$ 6 MeV, which was sufficient for the purpose of this study. Since the $(d,^3He)$-mode event rate was much lower than the (d,d)-mode event rate it was not feasible to optimize the K- and H-coil currents in the manner described above. Instead the coil currents were kept the same as for the (d,d)-mode. The duration of runs was typically five hours.

After acquiring the $(d,^3He)$-mode data-set the scattering chamber was vented to allow the spectrometer angle to be changed. The spectrometer and target angles were then changed while the quadrupole and dipole fields were being set to acquire the next set of (d,d)-mode data. In this manner the spectrometer modes were cycled.

Chapter 3

Analysis of Pickup Data

Data reduction and analysis of data acquired while operating the spectrometer in the $(d,^3\mathrm{He})$-mode is described in this chapter. The generation of focal-plane position spectra associated with the helions from the $^{55}\mathrm{Mn}(d,^3\mathrm{He})^{54}\mathrm{Cr}$ reaction at an average[1] incident energy of 45.6 MeV is described first. Thereafter the momentum calibration of the spectrometer's focal plane, the identification of $^{54}\mathrm{Cr}$ final states and the calculation of the corresponding pickup differential cross sections are discussed. In concluding the chapter, the extraction of pickup spectroscopic factors from the measured angular distributions by means of a distorted-wave Born approximation (DWBA) formalism is described.

3.1 Data replay

Focal-plane position spectra for helion events acquired in the $(d,^3\mathrm{He})$-mode were generated through off-line replay of event-by-event data using XSYS, the same software package used during data acquisition. The data sorting algorithm used in the EVAL program was almost identical to the one used during data acquisition (section 2.8).

Two of the modifications introduced into the sorting algorithm related to the subroutine which calculates the focal plane co-ordinates. A VDC wire hit-analysis discussed in appendix B showed that for a valid event, the num-

[1] Mean beam energy delivered as discussed in section 2.2.

ber of signal wires which are expected to register hits should range between 5 and 8. On the basis of a study made of the VDC intrinsic efficiency using the deuteron elastic scattering data (see appendix F), this condition was relaxed during final replay so that a VDC event was considered valid only if between 3 and 10 wires registered hits. During data acquisition the focal-plane co-ordinates were determined from least-squares fits to only three data points relating to measured VDC data. In order to improve the resolution in the focal-plane position spectra, fits were made to between three and seven data points during off-line analysis. A more detailed description of the algorithm used to calculate focal-plane co-ordinates can be found in appendix C.

Helion events were selected by means of a software gate set on the helion peak appearing in the raw time-of-flight (TOF) spectrum (see also section 2.6.1). An example of such a gate setting is shown in figure 3.1(a). VDC data corresponding to the selected times-of-flight were then used by a sorting subroutine, which was called from the main EVAL program, to calculate the focal-plane position spectra. One of the criteria used in selecting valid VDC data was whether their drift times fell within an acceptable range. This range was defined by a software gate set on an average VDC drift-time spectrum as shown in figure 3.2. During data acquisition a rough setting of this gate was used. By iteratively applying different gate settings and recording the corresponding helion yield in the focal-plane position spectrum during data replay, the width of this gate was optimized.

In order to improve the signal-to-noise ratio in the $(d,^3\mathrm{He})$-mode focal-plane position spectra, additional spectra were introduced on which software cuts were implemented. The first of these involved the focal-plane angle spectrum. Since the VDC was positioned at an angle of 35.75° w.r.t. the central-momentum trajectory through the spectrometer (see figure 2.6), valid events through the spectrometer should yield an event distribution in the focal-plane angle spectrum with its centroid corresponding to this angle. In order to exclude events which fall outside this distribution, a gate was also set on the focal-plane angle spectrum. A typical setting of such a gate is shown in figure 3.3(a). Software gates were also set on the two-dimensional correlation spectrum in which the pulse heights associated

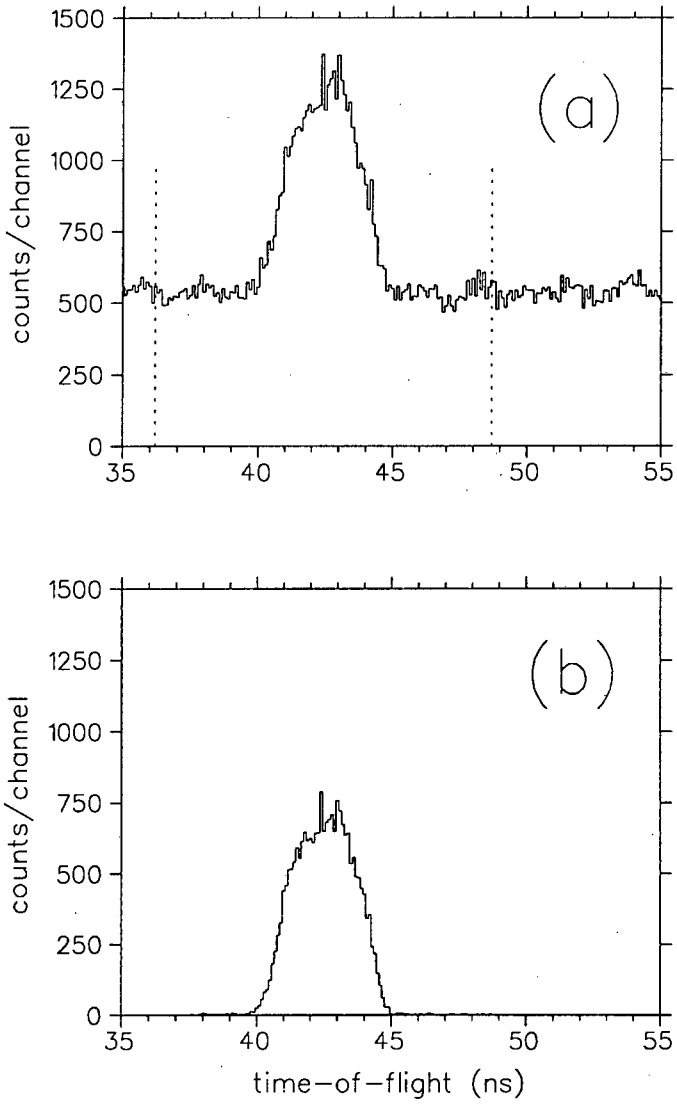

Figure 3.1: *Helion time-of-flight spectra. (a) Raw spectrum with software gate used. (b) Spectrum corresponding to one above associated with valid VDC data.*

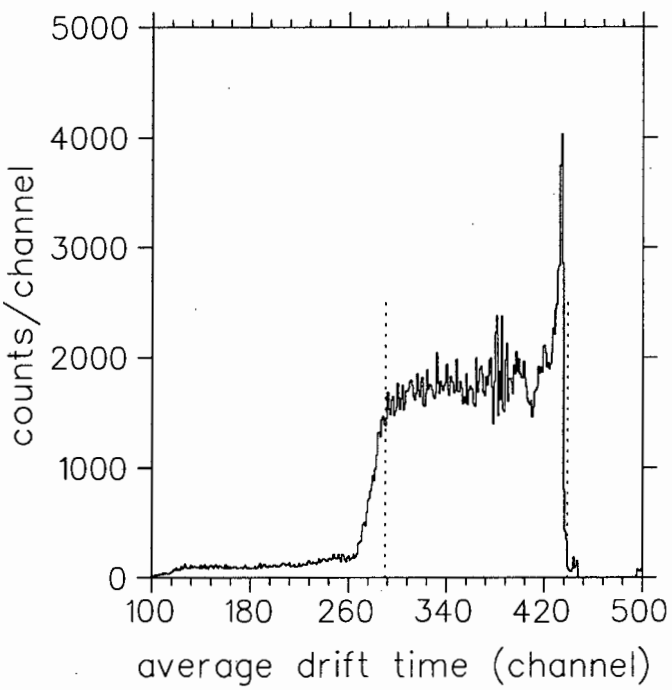

Figure 3.2: *Typical VDC average drift-time spectrum. One drift-time channel is equivalent to* $\sim$ *0.9 ns. A software gate set to encompass an optimal drift-time range is also shown.*

with the left[2] and right photomultiplier tubes of paddle 1 respectively were plotted as a function of focal-plane position. An example of such a spectrum along with the corresponding applied software gate is shown in figure 3.3(b). Finally gates were also set on the two-dimensional spectra in which the pulse heights associated with the photomultiplier tubes of paddle 1 were plotted as a function of TOF through the spectrometer. Figure 3.3(c) shows a typical example of a gate set on one of these spectra.

3.2 Momentum calibration

The momentum calibration of the focal plane was obtained using a similar approach to that used by Niwano *et al.* [Niw82]. In this approach the peak centroids of prominent (more than 100 counts) ^{54}Cr final states were determined followed by a calculation of the helion momenta associated with transitions to these states. A least-squares fit to the centroids and momenta associated with each of these states was then performed to obtain a momentum calibration.

Peak centroids of prominent ^{54}Cr final states were determined by least-squares fitting Gaussian lineshapes to these states as were seen in the focal-plane position spectra. The peak fitting was done using the computer program FIT2.1 [Neu94]. Because of the improvement in the signal-to-noise ratio achieved as a result of the additional software cuts discussed above, the background in the spectra was assumed to be negligible during this procedure. MINUIT [Jam75, Jam89], the non-linear least-squares minimization program selectable from FIT2.1, was used in order to calculate uncertainties in parameters by taking into account parameter correlations. No constraints were placed on fit parameters during the fitting procedure. Examples of typical fits obtained are shown in figure 3.4(a).

The momenta of the helions associated with transitions to these prominent states were calculated using a nonrelativistic kinematics formalism [Mar68, Lu84] which required as input the deuteron beam energy, spectrometer angle, the Q-value associated with the ^{55}Mn(d,^{3}He)^{54}Cr(g.s.) reaction and the excitation energies of known ^{54}Cr final states as most recently

[2]From the perspective of a rigidity-selected particle approaching the focal plane.

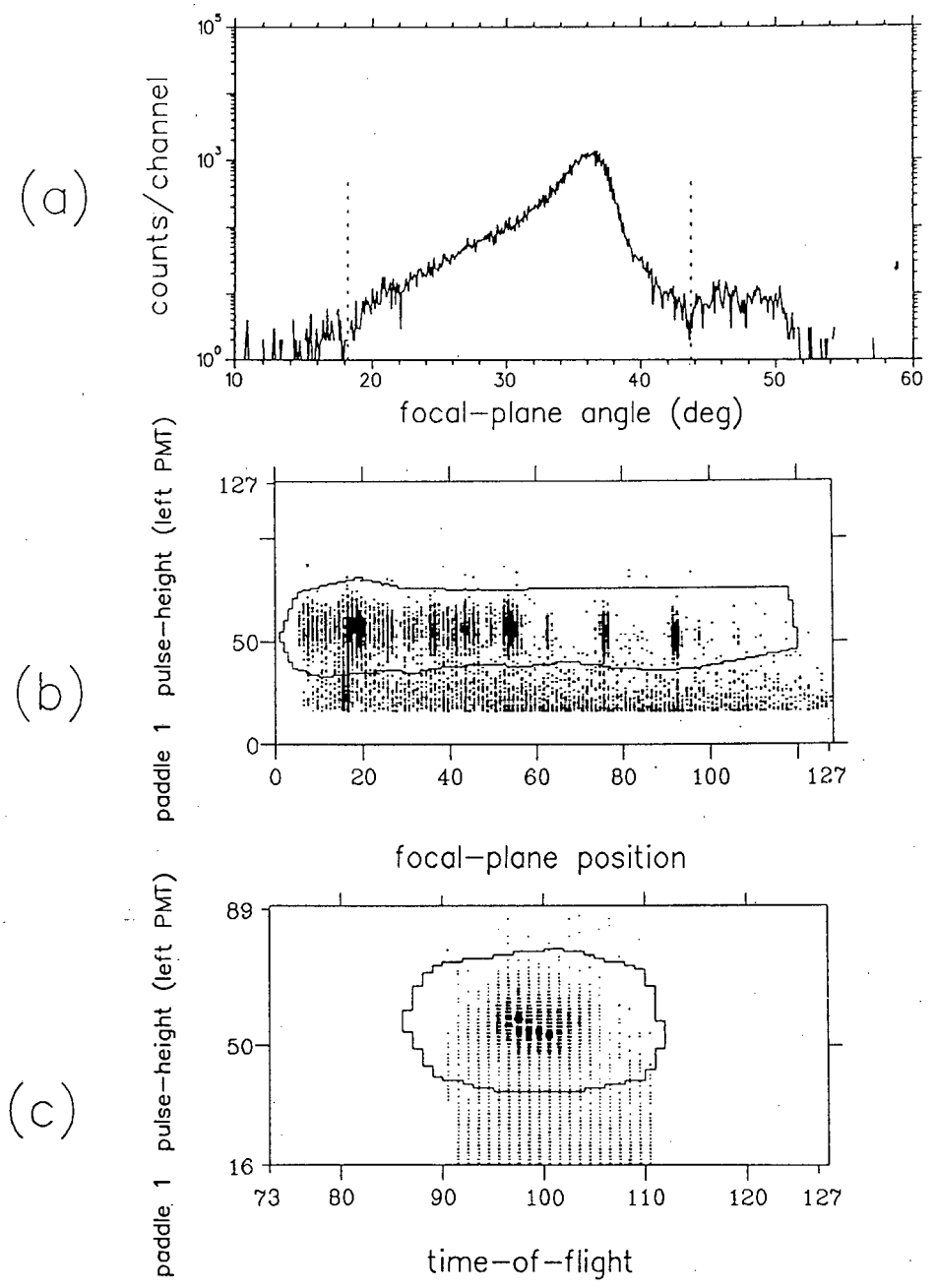

Figure 3.3: *Typical examples of spectra with respective software gate settings used to improve the signal-to-noise ratio in focal-plane position spectra (a) A focal-plane angle spectrum. (b) Density plot of pulse height associated with the left photomultiplier of paddle 1 is plotted versus focal-plane position. (c) Density plot of pulse height associated with the left photomultiplier of paddle 1 versus time-of-flight through the spectrometer.*

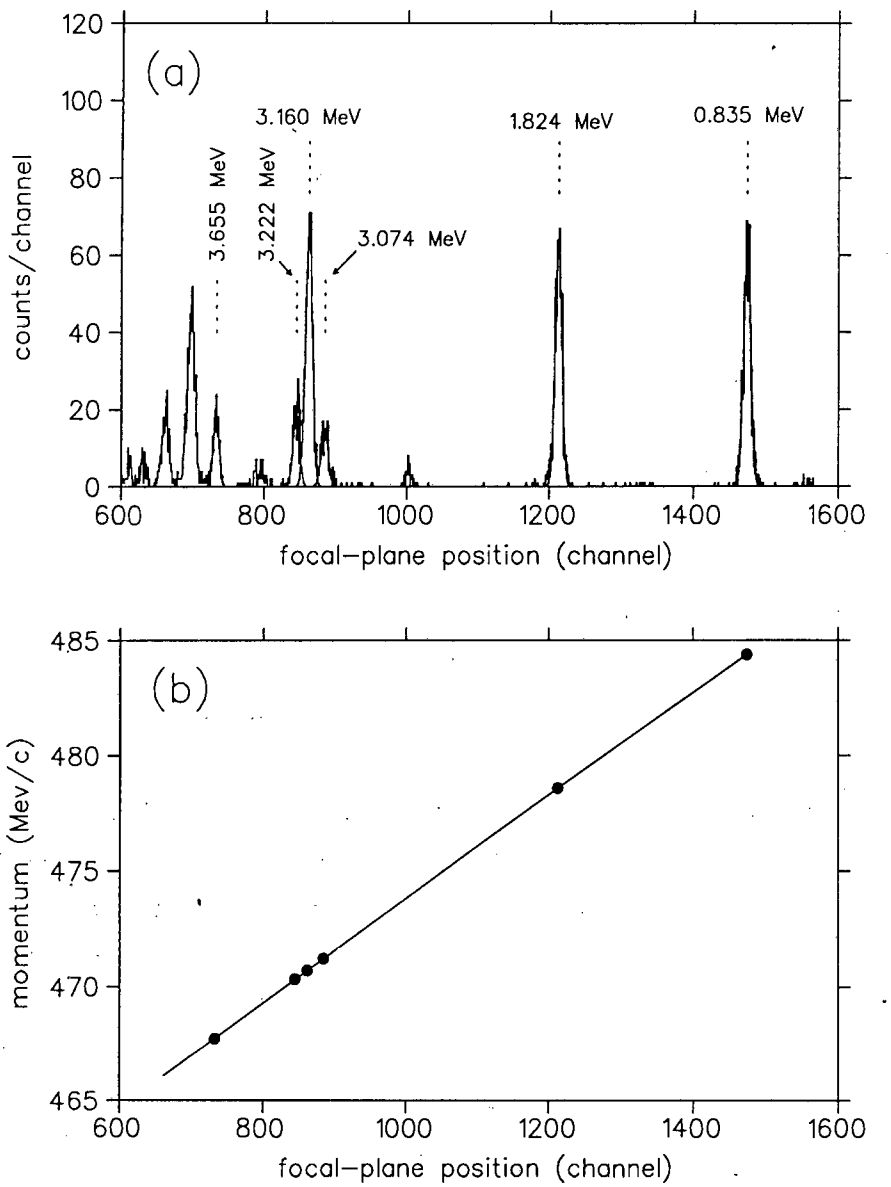

Figure 3.4: *(a) Typical example of a focal-plane position spectrum showing the location of ^{54}Cr final states used to obtain a momentum calibration of the focal plane. Gaussian lineshapes fitted to the identified states in order to determine their centroids are shown. The data shown were acquired at a spectrometer angle of 30°. (b) Quadratic least-squares fit to data associated with the selected states shown in (a).*

reported [Jun93]. Pairs of momentum and centroid co-ordinates were then least-squares fitted to obtain the momentum calibration. F-test analyses of reduced chi-squared (χ^2_ν) values obtained for fits made using polynomials, varying in order between one and three, showed that a polynomial of order two was the optimal function to use in describing the relationship between focal-plane position and momentum. All final fits were therefore performed using a quadratic function. The co-variance matrix associated with each fit was used later in calculating the uncertainty in the excitation energies of states identified (section 3.3).

The ^{15}N(g.s.) peak reached through the ^{16}O(d,^{3}He)^{15}N reaction was clearly seen in almost all the focal-plane position spectra. The first and second excited states in ^{54}Cr were also prominent at all spectrometer angles. A rough momentum calibration using only the ^{54}Cr(1), ^{54}Cr(2) states and the ^{15}N(g.s.) was therefore first determined for each data-set. These calibrations were then used to ascertain whether any other prominent states corresponded, to within a 40 keV uncertainty[3], with any of the ^{54}Cr adopted levels. Additional states in ^{54}Cr identified in this way were then used along with the first two excited states in ^{54}Cr to obtain a final momentum calibration. Typically six prominent ^{54}Cr final states ranging in excitation energy up to $\sim$ 4 MeV were used to obtain final momentum calibrations. An example of a focal-plane position spectrum revealing the states used to obtain a final momentum calibration is shown in figure 3.4(a), while the quadratic fit to the centroids and momenta associated with these states is shown in figure 3.4(b).

In the nonrelativistic approximation the relationship between momentum resolving power, $\frac{\Delta P}{P}$, particle energy E and energy resolution, ΔE, is given by

$$\frac{\Delta E}{E} = \frac{2\Delta P}{P}. \tag{3.1}$$

The energy resolution associated with each focal-plane position spectrum analysed was calculated with equation 3.1, using the momentum calibration obtained from this spectrum and the FWHM of the peak associated with the transition to the ^{54}Cr(1) state seen in the spectrum. The resolution was

[3]This value was chosen since the average spectrometer resolution was $\sim$ 40 keV.

found to vary between 32 and 60 keV, yielding an average energy resolution of $\sim$ 40 keV (FWHM).

3.3 Identifying observed final states

In order to identify less prominent and unresolved states, all peaks in the focal-plane position spectra were fitted with Gaussian lineshapes so as to determine their centroids. The peak-fitting was again performed using the program FIT2.1 together with the assumption that the background in the spectra was negligible. Fits, in which all parameters were allowed to vary, were first made to prominent well-resolved peaks in each spectrum in order to determine an average peak FWHM for that spectrum. Gaussian functions with widths fixed to these average FWHM were then again fitted to less prominent and unresolved states in all spectra. The excitation energies of all states seen in a particular focal-plane position spectrum were then calculated with standard formulae [Mar68, Lu84], using the peak centroids associated with these states as determined from the peak fitting and a corresponding momentum calibration. If a particular ^{54}Cr final state, k, excited through the ^{55}Mn(d,^{3}He)^{54}Cr(k) reaction was observed at the same excitation energy (to within statistical uncertainties) at a minimum of six spectrometer angles, the differential cross sections associated with the transition to this state and the corresponding spectrometer angles, were considered to constitute a pickup angular distribution. Since the counting statistics associated with ^{54}Cr final states observed in spectra for angles $\theta \geq 30°$ were rather poor, only data acquired in the 6°–30° angular region were used to extract spectroscopic factors. The mean excitation energies[4] of the twenty-four ^{54}Cr states which were found to satisfy the criterion stated above from these data are tabulated in table 3.6, while an example of a focal-plane position spectrum showing the location of identified ^{54}Cr final states is shown in figure 3.5.

[4]Note that the values above 3.926 MeV excitation differ by a few keV from those quoted in Ref. [New96]. This is due to an error in the momentum calibration which was discovered and subsequently corrected after the paper was in press.

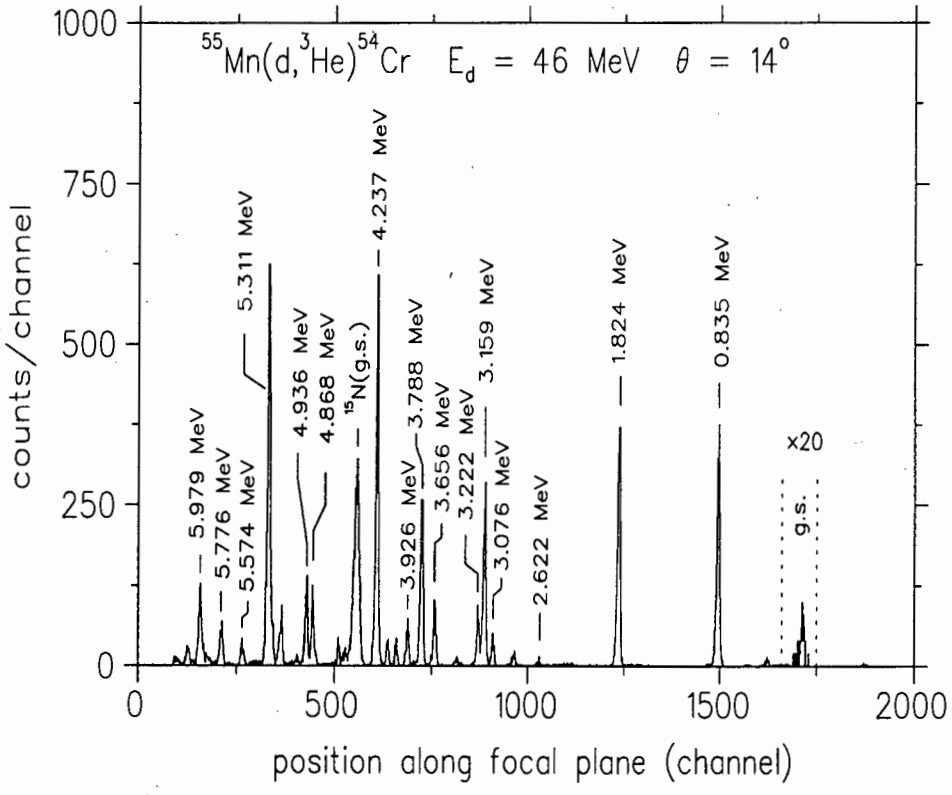

Figure 3.5: *Example of a focal-plane position spectrum associated with the $^{55}Mn(d,^{3}He)^{54}Cr$ reaction showing the location of some of the ^{54}Cr final states observed. The data shown were obtained at a spectrometer angle of 14°. The $^{15}N(g.s.)$ peak is due to $(d,^{3}He)$ reactions on the oxygen nuclei present in the Mylar target-backing used.*

The total uncertainty, ΔE^*, in the mean excitation energy of each of these states was calculated using the relation:

$$\Delta E^* = \sqrt{\Delta E_A^{*2} + \Delta E_B^{*2}} \tag{3.2}$$

where

- ΔE_A^* is the type A (statistical) uncertainty[5] associated with the state's excitation energy and
- ΔE_B^* is the type B (non-statistical) uncertainty associated with this state's excitation energy, evaluated by non-statistical means.

The former uncertainty was assumed to be equal to the standard deviation associated with the mean excitation energy for a particular state, while the latter uncertainty was found by averaging in quadrature over the type B uncertainties (at the $\pm 1\sigma$ level) associated with each excitation energy. The last mentioned uncertainties were calculated using the relation:

$$\Delta E_B^{*2} = f^2(\Delta E_c^{*2} + \Delta E_m^{*2}) \tag{3.3}$$

where

- ΔE_c^* is the energy uncertainty stemming from the uncertainty in the centroid position for each state as determined from the peak-fitting procedure,
- ΔE_m^* is the energy uncertainty stemming from the uncertainty in the parameters obtained from the co-variance matrix associated with each momentum calibration and
- $f = 0.46$ is the numerical factor used to make estimates of standard deviations from a trapezoidal probability distribution (see appendix G).

The total uncertainty in excitation energy of the twenty-four states observed varied between 1 and 11 keV. These uncertainties are also tabulated in table 3.6. Only two states, observed at excitation energies of 5.574 MeV

[5]See appendix G for an overview of treatment of experimental uncertainties adopted in this study.

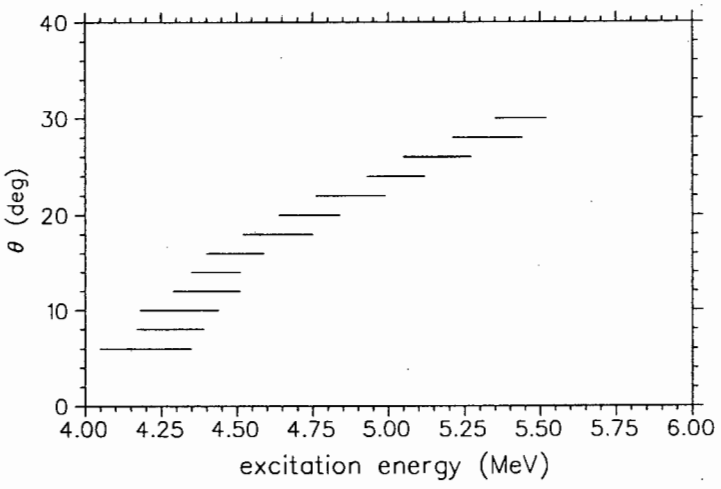

Figure 3.6: *Plot of the ^{54}Cr excitation region screened by the ^{15}N(g.s.) peak versus spectrometer angle. The ^{15}N(g.s.) is reached through $^{16}O(d,^3He)^{15}N$ reactions in the Mylar backing of the target.*

and 5.776 MeV respectively, did not correspond with the adopted levels for ^{54}Cr [Gon87, Jun93] to within the calculated uncertainties.

Impurity states in focal-plane position spectra arising from (d,^{3}He) reactions on impurities in the target were identifiable since their location in relation to ^{54}Cr excitation energy displayed a systematic shift as a function of spectrometer angle. The most significant impurity state seen was the ^{15}N(g.s.) reached by deuteron interactions on oxygen in the Mylar backing. Because the Mylar was relatively thick there was concern that the ^{15}N(g.s.) state would completely screen part of the 0–6 MeV excitation region under study. The excitation region corresponding to the ^{54}Cr residual nucleus which was found to be screened by this state as a function of spectrometer angle is shown in figure 3.6. It is seen from this figure that no excitation region was completely screened for all spectrometer angles.

3.4 Cross sections

The absolute centre-of-mass (c.m.) differential cross section associated with the transition to the kth final state, reached via the ^{55}Mn(d,^{3}He)^{54}Cr(k) reaction, at a spectrometer angle θ and corresponding c.m. angle $\theta_{\text{c.m.}}$, was

calculated using the formula

$$\frac{d\sigma}{d\Omega}(\theta_{\text{c.m.}}) = \frac{J\, Y_k\, cos\frac{\theta}{2}}{N_d\, \Delta\Omega\, n_t\, T_{k600}\, L\, \epsilon_P\, \epsilon_V} \tag{3.4}$$

where

- J is the Jacobian used to transform differential cross sections from the laboratory to the c.m. system,
- Y_k is the number of helions, associated with the reaction, which are detected at the spectrometer's focal plane per unit time interval,
- $cos\frac{\theta}{2}$ is the factor used to correct the target thickness since the target angle was always set to half the spectrometer's angle[6],
- N_d is the number of deuterons incident on the target per unit time interval,
- $\Delta\Omega$ is the solid angle subtended by the entrance collimator to the spectrometer,
- n_t is the number of ^{55}Mn nuclei per unit volume in the target,
- T_{k600} is the transmission efficiency through the k = 600 spectrometer for the helions of interest,
- L is the effective fractional livetime of the data acquisition system,
- ϵ_P is the efficiency of the plastic scintillator at detecting the helions of interest and
- ϵ_V is the VDC efficiency at detecting the helions of interest.

The determination of the quantities delineated above are discussed in more detail below.

[6]See section 2.4.

3.4.1 Jacobian

Jacobians were calculated using standard nonrelativistic kinematics [Mar68, Lu84]. The energy spread in the beam and the uncertainty in scattering angle because of the finite in-plane angular acceptance cause uncertainties in the Jacobian. Assuming a 10 keV spread in the beam energy and a 0.5° uncertainty in θ, the uncertainty in the Jacobian typically amounted to 0.01%.

3.4.2 Yields

Helion yields were determined from the focal-plane position spectra which were generated in the manner described in section 3.1. These yields were determined by means of two approaches, both of which assumed the background in the spectra to be negligible. In the case of free-standing, resolved states (for example the ^{54}Cr states at 0.835 MeV and 1.824 MeV shown in figure 3.4 and the 5.574 MeV and 5.776 MeV states shown in figure 3.7) Y_k was determined by summing the counts in the peak of interest. The yield associated with such peaks was considered to be distributed over j channels, each of which contained $s(j)$ counts, so that

$$Y_k = \sum_j s(j). \tag{3.5}$$

It was assumed that $s(j)$ followed the usual Poisson counting statistics so that the type A (statistical) uncertainty in Y_k was given by $\sqrt{Y_k}$.

In the case of unresolved states the yield associated with each of the states was determined by a combination of the summing procedure described above and the Gaussian peak-fitting procedure described in section 3.3. Gaussian lineshapes having FWHM values fixed to an average value, determined from fits to resolved states in a particular spectrum, were first fitted to these states. A typical fit to a set of unresolved states is shown in figure 3.7. Consider the case in which n Gaussians were fitted to a region of the spectrum spanning m channels. Let the area[7] under the nth Gaussian and the total number of counts in the region of the focal-plane position

[7]The yield associated with a particular Gaussian lineshape parameterized by height A and standard deviation σ is given by $\sqrt{2\pi}\,A\,\sigma$.

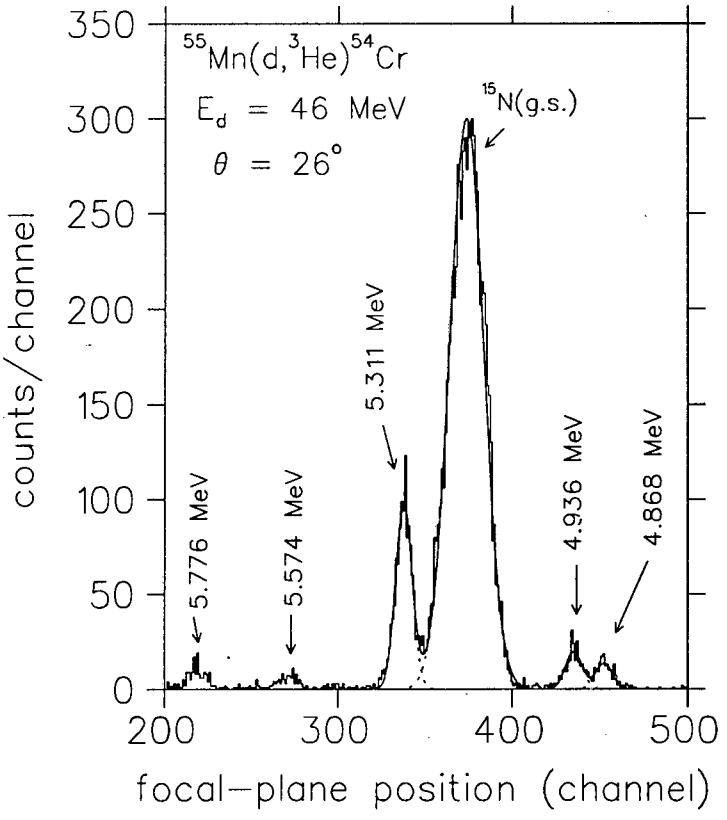

Figure 3.7: *A typical fit to a set of unresolved final states in order to determine helion yields. The widths of the Gaussians lineshapes used to fit ^{54}Cr final states were fixed to an average value determined from fits to resolved ^{54}Cr states observed in the same spectrum. The yield associated with the 5.574 MeV and 5.776 MeV states were determined via a summing procedure (see text for details). The $^{15}N(g.s.)$ is reached via (d,^{3}He) reactions on oxygen present in the Mylar target-backing used.*

spectrum considered be denoted by A_n and Y_{tot} respectively. The yield associated with the kth state, Y_k, was then determined using the relation:

$$Y_k = \frac{A_k\, Y_{tot}}{\sum_n A_n} \tag{3.6}$$

where

$$Y_{tot} = \sum_m s(m).$$

By using the above relation, mismatch between the assumed Gaussian line-shape and the actual peak shape is taken into account when determining yields. The type A uncertainty associated with the Y_k was taken to be equal to the uncertainty associated with A_k. This uncertainty was obtained from the program FIT2.1.

To assess whether helion yield was lost as a result of the additional software cuts used to improve the signal-to-noise ratio (section 3.1), the yield associated with the transition to the ^{54}Cr(1) final state was studied as a function of various cuts. In the worst case the helion yield was found to be reduced by $\sim 4\%$ so that the uncertainty (1σ) associated with yields stemming from the setting of software gates mentioned above was estimated to be $\leq 2\%$ using a trapezoidal probability distribution (see appendix G). The average uncertainties associated with the pickup differential cross sections due to counting statistics ranged between 24% (for the transition to the ^{54}Cr ground state) and 3% (for the transition to the state observed at 3.788 MeV excitation).

3.4.3 Incident flux

N_d, the number of deuterons incident on the target for the same time interval in which Y_k helions were detected was determined from the relation:

$$N_d = \frac{(N_{ci})\,(FS)}{1000\, e} \tag{3.7}$$

where N_{ci} is the number of digital pulses generated by the current integrator in response to the current from the beam-stop, FS is the current integrator full-scale setting set during data acquisition and e is the fundamental unit of electric charge. The current integrator's (see table 2.7) technical specifications state that current can be read to an accuracy of 0.02%. In

order to accommodate any contribution to the uncertainty from calibration adjustments, a maximum type B (non-statistical) uncertainty of 1% was assumed. This was again assumed to be drawn from a trapezoidal probability distribution in order to extract an estimated standard deviation. The uncertainty in the accumulated charge was thus taken to be 0.5%.

3.4.4 Solid angle

Since the distance between the target and the entrance collimator of the spectrometer was much larger than the dimensions of this collimator, the solid angle, $\Delta\Omega$, subtended by this collimator at the target was calculated by dividing the area of the collimator aperture by the target-to-collimator distance [Kno89] (see figures 2.2, 2.8, 2.9 and 2.10). The solid angle was therefore calculated using the relationship:

$$\Delta\Omega = \frac{\pi r^2 + (l - 2r)2r}{L^2} \tag{3.8}$$

where $2r$ is the width of the collimator, l is the length of the collimator slit and L is the distance from the centre of the target to the back of the collimator. For both collimators used in the normal- and the small-angle mode, this solid angle amounted to 1.34 msr. The total uncertainty in $\Delta\Omega$, calculated by propagating the experimentally measured uncertainties associated with the target-collimator distance and collimator dimensions in the normal manner, amounted to 0.3%; while the uncertainty in $\Delta\Omega$ due to beam-spot size was found to be negligible.

3.4.5 Target nuclear density

The number of ^{55}Mn nuclei per unit volume, n_t, was calculated using the relationship

$$n_t = \frac{t\rho N_A}{M} \tag{3.9}$$

where t is the thickness of the ^{55}Mn layer, ρ is the bulk density of ^{55}Mn, N_A is Avogadro's constant and M is the atomic mass of ^{55}Mn. The uncertainty in the n_t stems from the uncertainty associated with thicknesses determined using the computer program RUMP (see section 2.4). The latter uncertainty is estimated to vary between 5% and 10%. A 10% type B uncertainty was

assumed. Using a trapezoidal probability distribution, the uncertainty in n_t at the one standard deviation level amounted to 5%.

3.4.6 K = 600 transmission

In appendix D a study of the transmission through the spectrometer as a function of size of its entrance collimator is described. In this study, conducted by means of a variable-slot collimator, it was found that 100% transmission was still achieved when using a collimator slot which has a width (or height) of less than or equal to 55.0 mm. In view of the collimator geometry used in this study (see section 2.3.3), T_{k600} was therefore taken to be 100% in the evaluation of all differential cross sections.

3.4.7 Livetime

The effective fractional livetime of the data acquisition system was measured using the busy signal associated with the focal-plane electronics as described in section 2.7.4. The busy signal was generated whenever the VDC TDCs were busy digitizing, data was being transferred from the dedicated crate controller to the databus interface module or when there was a paddle signal. The livetimes associated with the data-sets analysed were typically 96% and was never less than 89%. The corresponding deadtimes were accounted for in hardware by inhibiting pulses from the current integrator whenever a busy signal was present.

3.4.8 Paddle efficiency

The efficiency of the paddle at detecting the helions of interest, ϵ_P, can be written as the product [Kno89]

$$\epsilon_P = \epsilon_{P_g} \epsilon_{P_i} \tag{3.10}$$

where ϵ_{P_g} and ϵ_{P_i} are the paddle geometric and intrinsic efficiencies, respectively, for detecting these helions.

The paddle geometric efficiency was checked at $\theta = 18°$ by sweeping the helions associated with the transition to the ^{54}Cr(1) peak across the focal plane by adjusting the magnetic field of dipole 2. A plot of relative

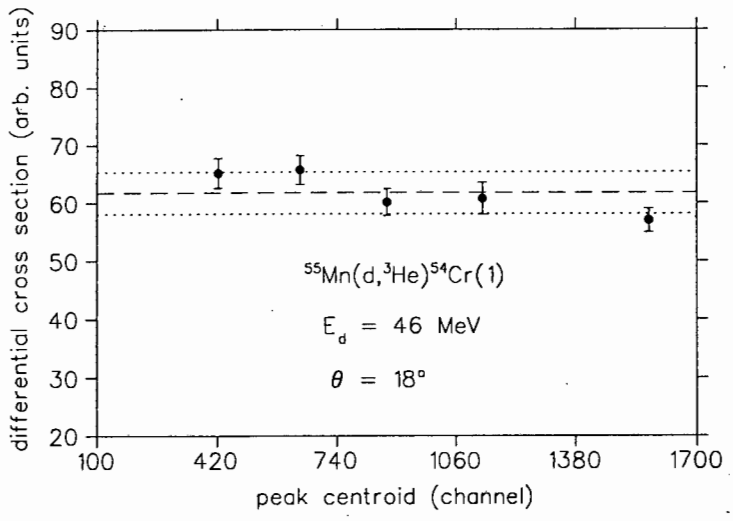

Figure 3.8: *Relative differential cross section for $^{55}Mn(d,^{3}He)^{54}Cr(1)$ (E_d = 46 MeV,θ = 18°) reaction versus centroid of the $^{54}Cr(1)$ state along the focal plane. The dashed line represents the mean value while the dotted lines are located ± 1σ from the mean.*

differential cross section[8] associated with the ^{55}Mn(d,^{3}He)^{54}Cr(1) (E_d = 46 MeV, θ = 18°) reaction as a function of the centroid of the ^{54}Cr(1) peak along the focal plane is presented in figure 3.8. Since the cross sections were found to be consistent to within statistical uncertainties, the paddle geometric efficiency was taken to be 100%. It is rare for primary charged particles not to produce some sort of ionization or excitation interaction in the active detecting material [Kno89]. In view of this and the fact that the thresholds on the constant fraction discriminators which were used to process the paddle signals were set to a minimum, the paddle intrinsic efficiency at detecting helions was assumed to be 100% as well. This was checked by studying the ratio of the photomultiplier-tube count rates as is normally done.

[8]Calculated by dividing the yield associated with the peak in the focal-plane position spectrum, by the product of the integrated current and the VDC efficiency.

quantity	symbol	% uncertainty
yield	Y	3–24 (type A)
		≤ 2 (type B)
solid angle	$\Delta\Omega$	< 1
incident deuteron flux	N_d	< 1
target nuclear density	n_t	5
Jacobian	J	~ 0.01

Table 3.1: *Breakdown of uncertainties associated with quantities appearing in equation 3.4 which were used to calculate the c.m. differential cross sections for the* $^{55}Mn(d,^3He)^{54}Cr$ *(E_d = 45.6 MeV) reaction.*

3.4.9 VDC efficiency

The VDC's efficiency, ϵ_V, is an indication of how efficient (relative to that of the plastic paddles) it is at detecting charged particles at the focal plane. As in the case of the paddles, the VDC efficiency is the product of a geometric and intrinsic efficiency:

$$\epsilon_V = \epsilon_{V_g}\epsilon_{V_i}. \tag{3.11}$$

It was established by means of a horizontal drift chamber (HDC) (located behind the VDC) which measures focal-plane position in the vertical direction, that the rigidity-selected particles are well-focussed[9]. In view of the above and the consistency shown in figure 3.8, the VDC geometric efficiency, ϵ_{V_g}, was taken to be 100%. The intrinsic VDC efficiency was obtained from an analysis of (d,d)-mode data as discussed in section F.1 of appendix F. An average efficiency of 99% was obtained.

3.4.10 Results

A breakdown of the uncertainties associated with the pickup differential cross sections is given in table 3.1. The combined uncertainty (1σ) associated with the target thickness, current integration, solid angle and setting of software gates was estimated to be $\sim$ 6%. The measured c.m. angular

[9]The FWHM of a peak is typically 2.0 cm.

distributions, associated with the transition to the twenty-four ^{54}Cr final states observed, and which were used in the DWBA analyses, are plotted in figures 3.9–3.15 and are tabulated in appendix E. Only the uncertainties contributing to random scatter, obtained by combining in quadrature the uncertainty due to counting statistics and the estimated uncertainty (1σ) in target thickness, are shown in these figures. The latter component was included since two targets were used to measure the angular distributions.

3.5 DWBA analyses

Pickup spectroscopic factors, C^2S_{ijl} (with C denoting the Clebsch-Gordan coefficient), are associated with the transfer of a proton, having orbital and total angular momentum ℓ and j respectively, leading to the ith final state of ^{54}Cr in the ^{55}Mn(d,^{3}He)^{54}Cr(i) reaction. These were determined by normalizing a distorted-wave Born approximation (DWBA) angular distribution to the measured angular distribution. The normalization was done by minimizing χ^2, defined by:

$$\chi^2 = \sum_{\theta_{\text{c.m.}}} \left(\frac{\sigma_{\text{expt}}(\theta_{\text{c.m.}})_i - C^2S_{ijl}\,\sigma_{\text{calc}}(\theta_{\text{c.m.}})_{ijl}}{\Delta\sigma_{\text{expt}}(\theta_{\text{c.m.}})_i} \right)^2, \qquad (3.12)$$

where $\sigma_{\text{expt}}(\theta_{\text{c.m.}})_i$ is the experimentally measured c.m. differential cross section associated with the transition to the ith final state, $\Delta\sigma_{\text{expt}}(\theta_{\text{c.m.}})_i$ is the uncertainty (obtained by combining in quadrature the uncertainty due to counting statistics and estimated uncertainty (1σ) in target thickness) associated with this cross section and $\sigma_{\text{calc}}(\theta_{\text{c.m.}})_{ijl}$ is the corresponding DWBA differential cross section.

DWBA differential cross sections were calculated with the computer code DWUCK4 [Kun93] using a local, zero-range formalism. Non-local and finite-range corrections were not applied since in the first instance the interest is in relative spectroscopic factors which have been shown to be insensitive to the inclusion or omission of these corrections [Cle77, Cle91]. In the case of the (d,^{3}He) reaction, DWBA differential cross sections are related to the corresponding DWUCK4 cross sections via the relation

$$\sigma_{\text{calc}}(\theta_{\text{c.m.}}) = \frac{N_o}{2j+1}\sigma_{\text{DWUCK4}}(\theta_{\text{c.m.}}), \qquad (3.13)$$

where j is the total angular momentum transfer and N_o is the Bassel normalization factor, equal to 2.95 in the case of the (d,^{3}He) reaction [Bru77, Kun93].

3.5.1 Optical-model parameters

Part of the input needed to calculate $\sigma_{\mathrm{DWUCK4}}(\theta_{\mathrm{c.m.}})$ is a specification of the potentials needed to generate the distorted wave-functions for the entrance and exit channels, and to calculate the bound-state wave functions.

An optical potential having a form identical to the one used by Bojowald *et al.* [Boj88] to obtain a global potential for deuteron scattering up to 100 MeV, was used to obtain the distorted wave-functions for the d + ^{55}Mn channel. This potential, which comprised Coulomb, central, imaginary volume, imaginary surface and real spin-orbit terms [Mar70], had the form

$$U(r) = V_c(r) - Vf_v(r,R_v,a_v) - i\Big[W_{vol}f_w(r,R_w,a_w) \qquad (3.14)$$
$$- 4a_wW_{surf}\frac{d}{dr}f_w(r,R_w,a_w)\Big] + V_{l.s}\left(\frac{\hbar}{m_\pi c}\right)^2(\ell\cdot s)\frac{1}{r}\frac{d}{dr}f_{l.s}(r,R_{l.s},a_{l.s}).$$

The nuclear potential formfactors in the expression above had a Saxon-Woods form given by :

$$f_k = \left[1+\exp\left[\frac{r-R_k}{a_k}\right]\right]^{-1} \qquad (3.15)$$

with radius $R_k = r_kA^{\frac{1}{3}}$ and diffuseness a_k. The Coulomb potential had the standard form:

$$V_c(r) = \frac{Z_pZ_te^2[3-(\frac{r}{R_c})^2]}{2R_c}, r < R_c \qquad (3.16)$$
$$= \frac{Z_pZ_te^2}{r}, r > R_c$$

where Z_p is the charge of the projectile, Z_t is the charge of the target and R_c is the Coulomb radius. The values of the parameters used in conjunction with the potential form above are given in table 3.4. These parameters were obtained from an analysis of the angular distribution for the ^{55}Mn(d,d)^{55}Mn(g.s.) (E_d = 45.6 MeV, $6° \leq \theta \leq 48°$) reaction. This analysis which is detailed in appendix F, was performed using the computer code SNOOPY8 [Sch82] which utilizes a chi-square minimization procedure to obtain best-fit optical potential parameters.

parameter	parameterization/value
V	$104.1 + 0.2A$
W_{surf}	$21(1 - e^{-0.09\,A})$
r_v	1.15
r_w	1.25
a_v	0.80
a_w	0.80

Table 3.2: *Trost* et al. *[Tro80] parameterization of a ^{3}He optical-model potential at 41 MeV having the same form as that in equation 3.14 but with W_{vol} and $V_{l.s}$ set to zero (see text for details). A denotes the target nucleus mass. All potential depths are in MeV, and all geometrical parameters are in fm.*

parameter	parameterization/value
V	$179.87 - 0.1526A$
W_{vol}	$19.81 - 0.0137A$
r_v	1.14
r_w	1.60
r_c	1.40
a_v	0.71
a_w	0.875

Table 3.3: *Parameterization by Barr and DelVecchio [Bar77] of a ^{3}He optical-model potential at 39.7 MeV having the same form as that in equation 3.14 but with W_{surf} and $V_{l.s}$ set to zero (see text for details). A denotes the target nucleus mass. All potential depths are in MeV, and all geometrical parameters are in fm.*

As discussed in the introductory chapter, the bound-state potential parameters, especially the radius parameter, strongly affect the magnitude of spectroscopic factors. In this study, a 1% change in the bound-state potential radius was found to cause a 7% change in absolute spectroscopic factors but negligible change in relative spectroscopic factors. A standard bound-state potential comprising a Coulomb, central and Thomas spin-orbit term with $\lambda = 25$ was used. Standard values $a_v = a_{l.s} = 0.650$ fm were used. The potential well-depth was automatically adjusted by DWUCK4 to reproduce the experimental proton separation energies [Wap71]. The bound-state potential radii ($R_v = R_{l.s}$) were adjusted in order to obtain an fp shell proton occupancy of ~ 5 in ^{55}Mn. The bound-state potential parameters used are also shown in table 3.4.

Since helion beams are not available at NAC an optical potential and the corresponding distorted wave-functions for the exit channel could not be determined from an analysis of measured helion elastic scattering data. Instead ^{3}He optical potentials found in the literature were used. Trost *et al.* [Tro80] studied the mass dependence of the helion optical potential for light to medium mass nuclei at a beam energy of 41 MeV. They employed a "physical" potential characterized by a volume integral of the real part $J_R(^{58}\text{Ni}) = 330$ MeV fm^3. This potential has the same form as that given by equation 3.14, but with W_{vol} and $V_{l.s}$ set to zero. The parameterization associated with this potential is given in table 3.2. The other study of ^{3}He optical potentials was by Barr and DelVecchio [Bar77] who studied ^{3}He elastic scattering data at 39.7 MeV on targets ranging from ^{12}C to ^{197}Au. The optical potentials they studied had a form similar to the one in equation 3.14, but with W_{surf} and $V_{l.s}$ set to zero. The parameterization[10] associated with this potential is given in table 3.3.

Since the 6^+ ^{54}Cr final state observed at 3.220 MeV excitation can only be reached via $0f_{\frac{7}{2}}$ transfer, the angular distribution associated with this state was used to assess the relative merits of the potential parameterizations of Trost *et al.* and that of Barr and DelVecchio. DWBA angular distributions associated with the transition were obtained using these parameteriza-

[10]The parameterization of Barr and DelVecchio labelled "Fit G" was used.

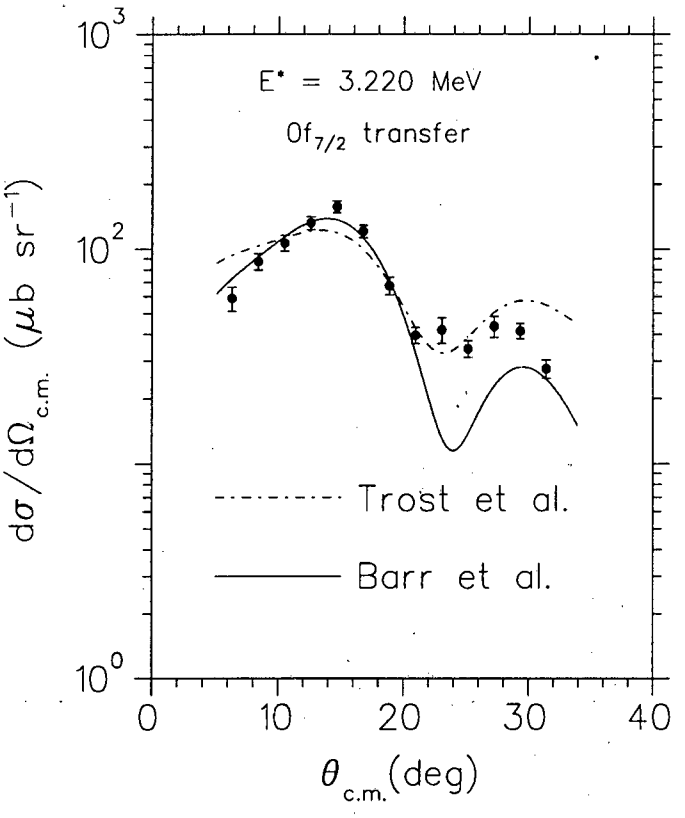

Figure 3.9: *Measured c.m. angular distributions for the* $^{55}Mn(d,^3He)^{54}Cr(E^* = 3.220\ MeV)$ *reaction at an average incident energy of 45.6 MeV. The curves result from DWBA calculations made using the descriptions of Trost* et al. *[Tro80] and Barr and DelVecchio [Bar77] for the exit channel potential, respectively. The potential parameters used to calculate the entrance channel and bound-state wave functions are listed in table 3.4.*

parameter	reaction channel $d + {}^{55}$Mn	^{3}He + ^{54}Cr	p
V	82.14	171.63	[a]
r_v	1.18	1.14	1.21
a_v	0.786	0.71	0.650
W_{vol}	0.079	19.07	
$4W_{surf}$	53.00		
r_w	1.27	1.60	
a_w	0.837	0.875	
$V_{l.s}$	4.73		λ=25
$r_{l.s}$	0.922		1.21
$a_{l.s}$	0.605		0.650
r_c	1.30	1.40	1.30

[a] Well-depth was adjusted by the program DWUCK4 [Kun93] to reproduce the experimental proton separation energies.

Table 3.4: *Potential parameters used in the DWBA analyses of angular distributions for the ^{55}Mn(d,^{3}He)^{54}Cr reaction at an average incident energy of 45.6 MeV. All potential depths are in MeV, and all geometrical parameters are in fm.*

tions along with the entrance channel and bound-state potential parameters shown in table 3.4. The resulting fits to the experimental data are shown in figure 3.9. The parameterization of Barr and DelVecchio was found to be the most suitable, as it resulted in a better fit to experimental points at forward angles which are more important for determining spectroscopic factors. The corresponding parameter values used are shown in table 3.4.

3.5.2 Extraction of spectroscopic factors

For ^{55}Mn it was assumed that proton pickup from the $0f_{\frac{7}{2}}$, $0f_{\frac{5}{2}}$, $1p_{\frac{3}{2}}$, $1p_{\frac{1}{2}}$, $0d_{\frac{5}{2}}$, $0d_{\frac{3}{2}}$ and $1s_{\frac{1}{2}}$ subshells was in principle observable in this study. Since ^{55}Mn has a known ground-state spin and parity of $\frac{5}{2}^{-}$, it is possible to establish the range of ^{54}Cr final-state spins, J', and parities, π', for proton

subshell	ℓ transfer	π'	J'
$0f_{7/2}$	3	+	$1 \leq J \leq 6$
$0f_{5/2}$	3	+	$0 \leq J \leq 5$
$1p_{3/2}$	1	+	$1 \leq J \leq 4$
$1p_{1/2}$	1	+	$2 \leq J \leq 3$
$0d_{5/2}$	2	-	$0 \leq J \leq 5$
$0d_{3/2}$	2	-	$1 \leq J \leq 4$
$1s_{1/2}$	0	-	$2 \leq J \leq 3$

Table 3.5: *Allowed final-state spins and parities for single proton pickup on ^{55}Mn from 0f1p and 0d1s shells. π' and J' denote the final-state parity and spin respectively.*

pickup from these subshells. This was done using the relation between parities

$$\pi' = \pi_{initial}\, \pi_{transfer} \tag{3.17}$$

and the triangular inequality:

$$|J_t - j| \leq J' \leq J_t + j \tag{3.18}$$

where J_t the ground-state spin and j the spin transfer. Table 3.5 summarizes the results. Since for a given ℓ transfer DWBA angular distributions are insensitive to the j transfer [Ver94], it was not possible to uniquely determine the j transfer by fitting the calculated angular distribution to the experimental data. Instead it was further assumed that an $\ell = 1$ transfer implied $1p_{\frac{3}{2}}$ proton transfer for $1 \leq J' \leq 4$, that $\ell = 2$ transfer implied $0d_{\frac{3}{2}}$ proton transfer for $1 \leq J' \leq 4$ and that an $\ell = 3$ transfer implied $0f_{\frac{7}{2}}$ proton transfer for $1 \leq J' \leq 6$.

Mixed transitions involving at most two types of (j,ℓ) transfer, say (j_a,ℓ_a) and (j_b,ℓ_b), were considered possible. Spectroscopic factors associated with each transfer were extracted using equation 3.12, with the expression for $C^2S\sigma_{\rm calc}(\theta_{\rm c.m.})$ now reading

$$C^2S_{a+b}\sigma_{\rm calc}(\theta_{\rm c.m.}) = \tag{3.19}$$

$$2.95\, C^2S_{a+b}\left(\frac{\gamma}{2j_a+1}\sigma_{\rm DWUCK4}(\theta_{\rm c.m.})_{j_al_a} + \frac{(1-\gamma)}{2j_b+1}\sigma_{\rm DWUCK4}(\theta_{\rm c.m.})_{j_bl_b}\right)$$

where $0 \leq \gamma \leq 1$. Spectroscopic factors associated with (j_a,ℓ_a) and (j_b,ℓ_b) transfers to the same final state are thus given by

$$C^2S_{j_a l_a}(\theta_{\text{c.m.}}) = \gamma\ C^2S_{a+b}(\theta_{\text{c.m.}}) \tag{3.20}$$

and

$$C^2S_{j_b l_b}(\theta_{\text{c.m.}}) = (1-\gamma)\ C^2S_{a+b}(\theta_{\text{c.m.}}). \tag{3.21}$$

Fits to each pickup angular distribution measured were made using the corresponding DWBA angular distribution associated with $\ell = 0$, 1, 2 or 3 transfer. Those angular distributions which were not well fitted with just one ℓ transfer were refitted allowing for mixed transitions involving any two of $\ell = 0$, 1, 2 or 3 transfers. By finding the ℓ transfer(s) which yielded the lowest χ^2 the (j,l) transfer(s) associated with that transition could be ascertained. In the final analysis spectroscopic factors associated with measured angular distributions which displayed an $\ell = 3$ transfer signature were calculated by restricting the angular range in equation 3.12 to the forward angles, $\theta_{\text{c.m.}} \leq 20°$, where the cross section peaks.

3.5.3 Results

The fits of the calculated angular distributions to the corresponding measured data are shown in figures 3.10 - 3.15, while the extracted spectroscopic factors are shown in table 3.6. It is stressed here that the pickup normalization was arbitrarily adjusted by appropriately adjusting the bound-state radius parameter as described above in order to reproduce the simple shell-model result of five protons residing in the fp shell in ^{55}Mn. Because of the weighting used in equation 3.12 the uncertainties in the extracted spectroscopic factors stemming from the uncertainties in experimental cross section ranged between 16% and 6% for the transitions to the ground and 3.788 MeV states of ^{54}Cr respectively.

All $\ell = 3$ strength was found to be localized to an excitation region below 4.1 MeV in ^{54}Cr. A relatively small strength of 0.02 was found for the transition to the ^{54}Cr ground state (0^+) which can only be reached by $0f_{\frac{5}{2}}$ transfer. This points to inaccuracies in the study of Colli *et al.* [Col59] in which an order of magnitude larger spectroscopic factor was reported

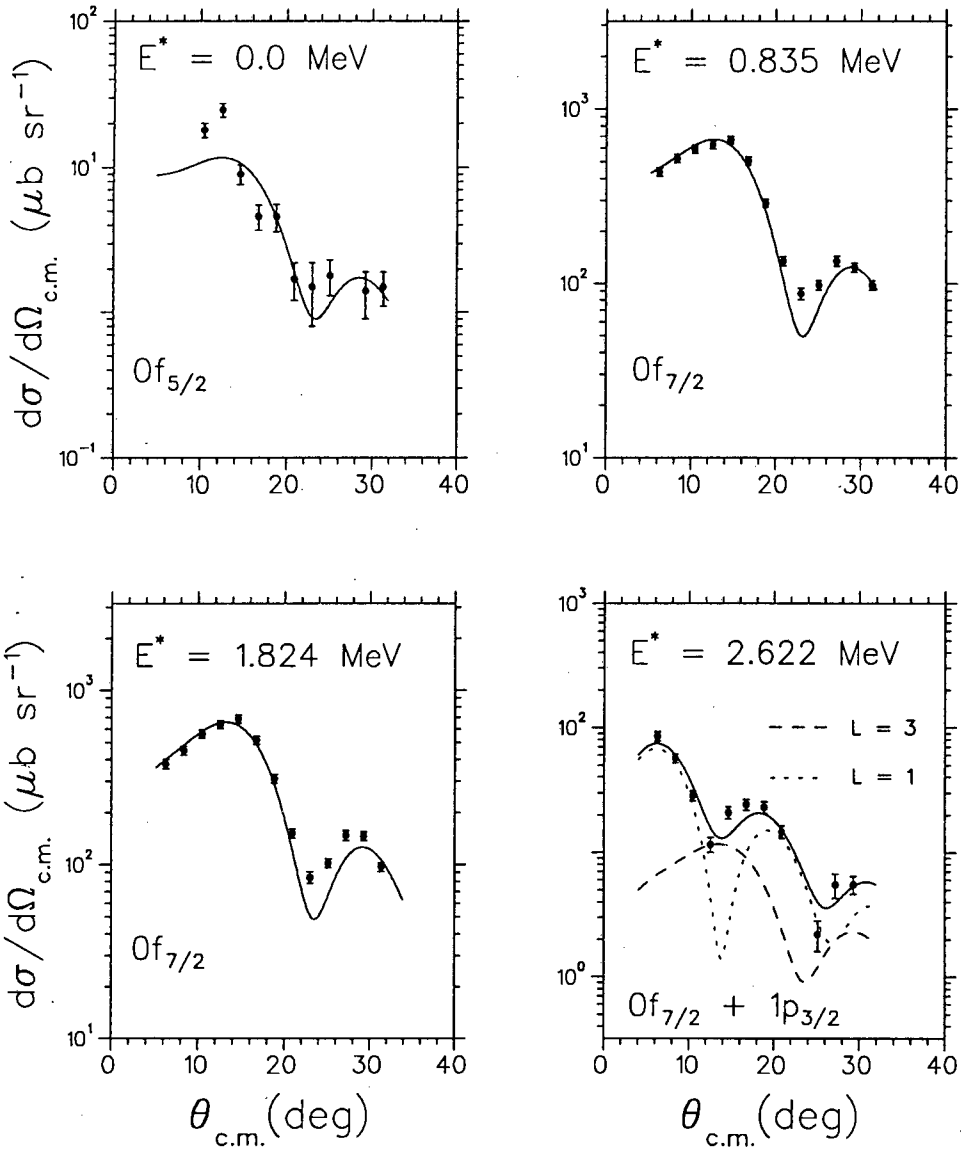

Figure 3.10: *Measured c.m. angular distributions for the $^{55}Mn(d,^3He)^{54}Cr$ reaction for final-state excitation energies, E^*, ranging between 0.0 and 2.622 MeV, at an average incident energy of 45.6 MeV. If not shown the uncertainty (see text for details) in differential cross section is smaller than the size of the plotting symbol. The curves result from DWBA calculations made using the potential parameters shown in table 3.4 and assuming (j,l) transfer(s) as indicated.*

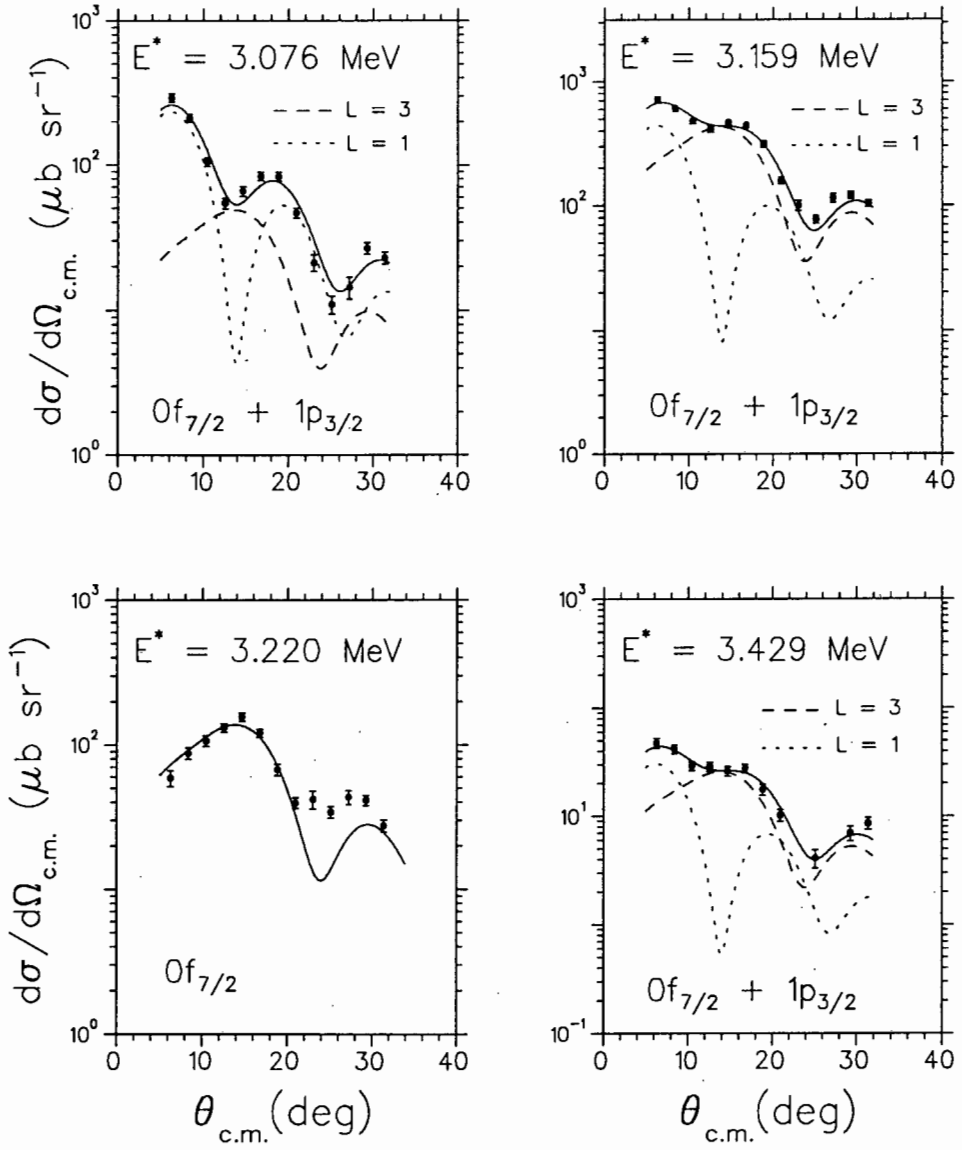

Figure 3.11: *The same as in figure 3.10 but for ^{54}Cr final-state excitation energies ranging between 3.076 and 3.429 MeV.*

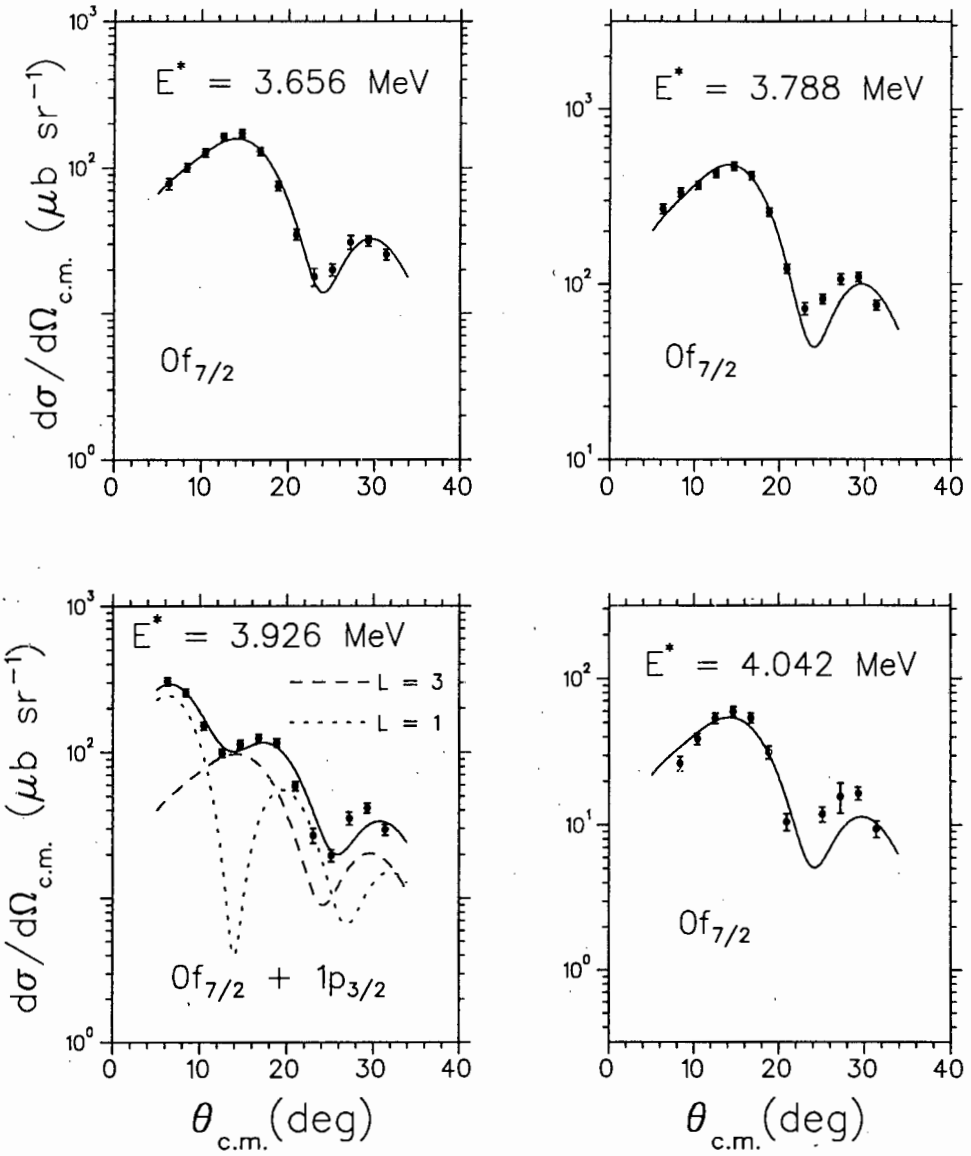

Figure 3.12: *The same as in figure 3.10 but for* ^{54}Cr *final-state excitation energies ranging between 3.656 and 4.042 MeV.*

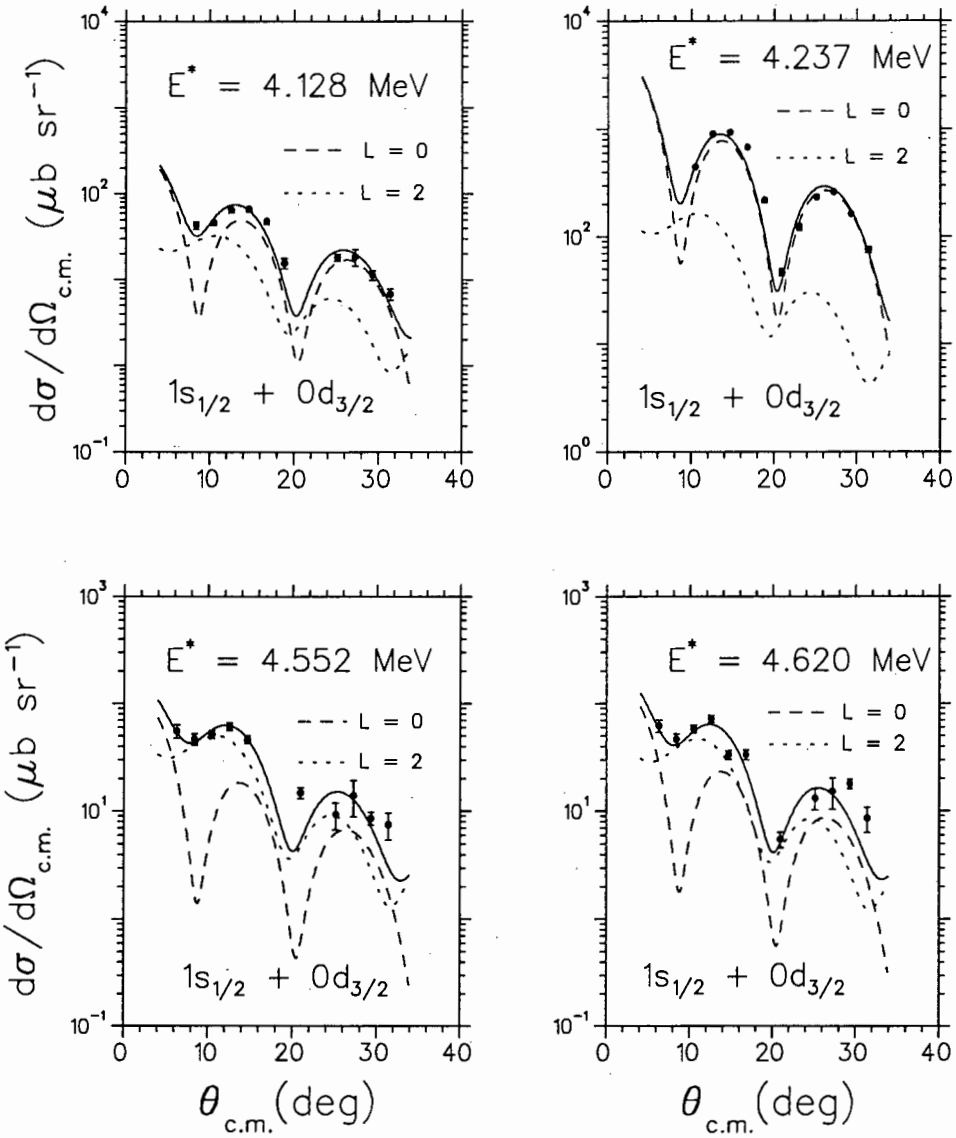

Figure 3.13: *The same as in figure 3.10 but for* ^{54}Cr *final-state excitation energies ranging between 4.128 and 4.620 MeV.*

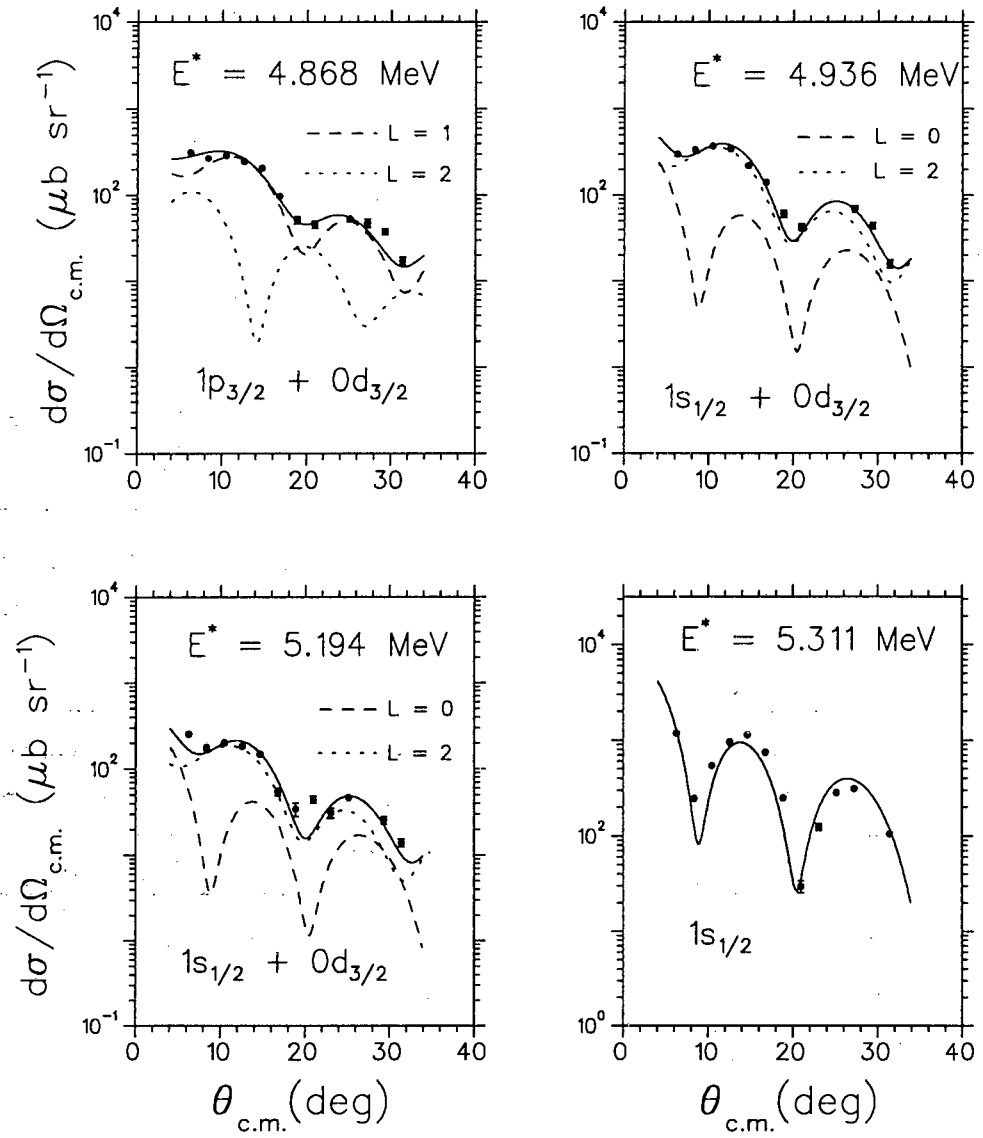

Figure 3.14: *The same as in figure 3.10 but for* ^{54}Cr *final-state excitation energies ranging between 4.868 and 5.311 MeV.*

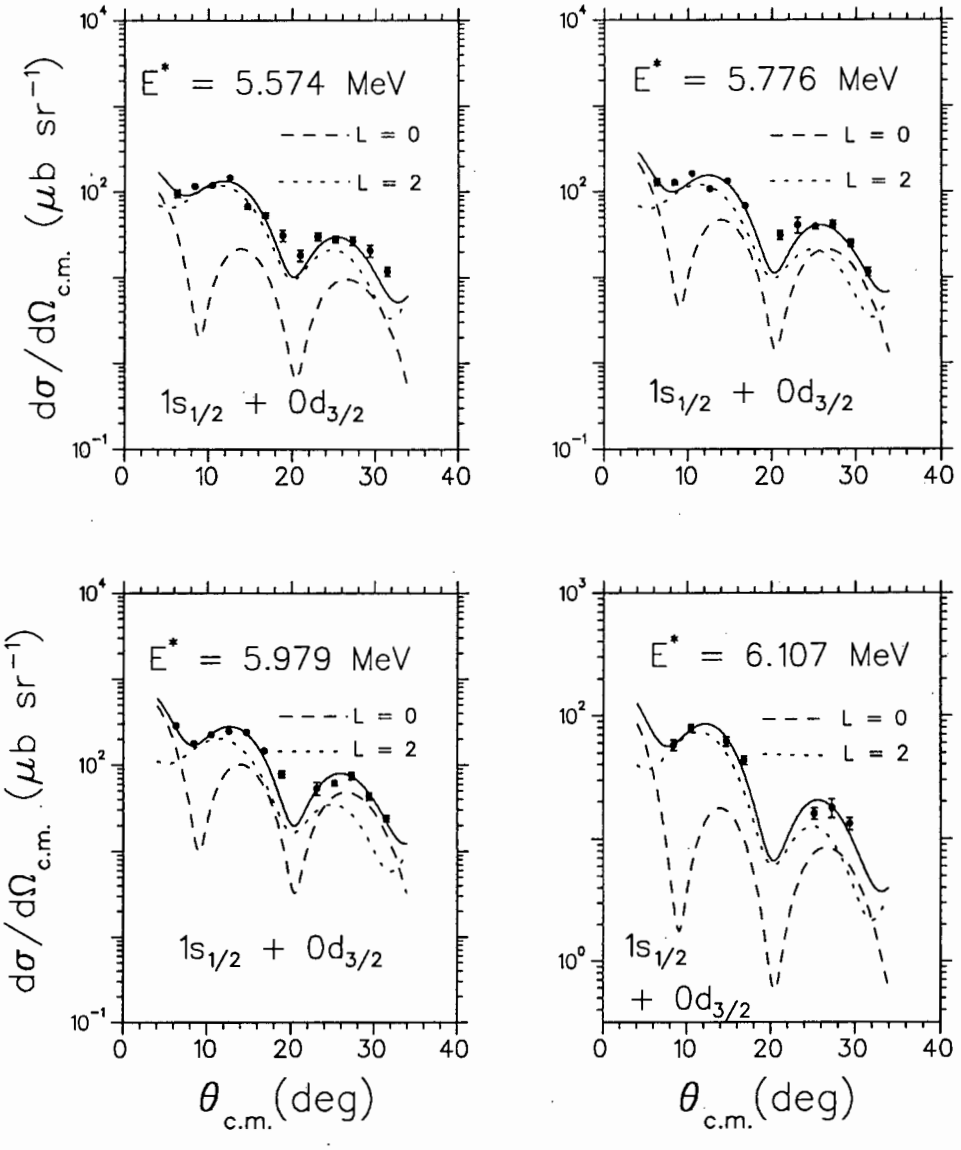

Figure 3.15: *The same as in figure 3.10 but for* ^{54}Cr *final-state excitation energies ranging between 5.574 and 6.107 MeV.*

for the transition to this state reached via the ^{55}Mn$(n,d)^{54}$Cr reaction (see table 1.4). The other 0^+ adopted levels at 2.830 and 4.013 MeV were not seen. These observations support the expectation that the $0f_{\frac{5}{2}}$ proton orbital is essentially unoccupied in ^{55}Mn. This is further supported by results from shell-model calculations which are discussed in section 4.1. Any remaining $\ell = 3$ strength was therefore assumed to be associated with $0f_{\frac{7}{2}}$ transfer.

Pickup from the $1s0d$ shell was also observed, leading to final states beginning with the known 3^- state at an excitation energy of 4.127 MeV. For all such states the best fits to the angular distributions were obtained using a mixture of $\ell = 0$ ($j = \frac{1}{2}$) and $\ell = 2$ (assumed $j = \frac{3}{2}$) pickup. However, wherever the $\ell = 0$ spectroscopic factor was less than 0.05 the improvement over pure $\ell = 2$ was marginal, and it was felt prudent not to assign $J' = (2,3)^-$ to these states on the basis of such small $\ell = 0$ contributions. An assignment of $J' = (1\text{–}4)^-$ is therefore made to these states in table 3.6. However, for the adopted levels at 4.245, 5.321 and 5.981 MeV the $\ell = 0$ contribution to the pickup cross section is much more secure, allowing the assignment $J' = (2,3)^-$ to be made to these states, and hence $J' = 3^-$ to the 4.245 MeV state using prior information. Also, the spin assignment of $J' = (0,1,2)$ to the adopted level at 5.189 MeV can be tightened to $(1,2)^-$.

The observed adopted level at 4.865 MeV has a spin assignment of $(1^-,4^+)$. An optimal fit to the corresponding angular distribution was obtained by allowing for ℓ transfers of 1 and 2, and it is likely that the state observed is a doublet. No new information about the spin assignment for this level was therefore obtained.

As mentioned in section 3.3, two new levels were observed at excitation energies of 5.574 and 5.776 MeV. Their associated angular distributions were fitted well by allowing for $\ell = 0$, 2 transfer, and again assignments of $J' = (1\text{–}4)^-$ were made to these states.

All new spin assignments made on the basis of the DWBA analyses as discussed above, are shown in the last column of table 3.6. The spin assignments of 6^+, 5^+ and 6^+ made to states at observed excitation energies of 3.220, 3.788 and 4.042 MeV, respectively will be discussed in chapter 4 together with the results of shell-model calculations and NEWSR analyses of $0f_{\frac{7}{2}}$ pickup and stripping transfer strength.

From Ref. [Jun93]			This work						
					C^2S				New $J^{'\pi}$
E^* (MeV)	ΔE^* (keV)	$J^{'\pi}$	E^* (MeV)	ΔE^* (keV)	ℓ=0	ℓ=1	ℓ=2	ℓ=3	assignment
0.0		0^+	0.0	0				0.02	
0.835	≤1	2^+	0.835	1				0.85	
1.824	≤1	4^+	1.824	2				0.99	
2.620	≤1	2^+	2.622	4		0.01		0.02	
3.074	≤1	2^+	3.076	3		0.05		0.09	
3.160	≤1	4^+	3.159	1		0.09		0.84	
3.222	≤1	$(6)^+$	3.220	5				0.27	6^+
3.437	≤1	2^+	3.429	8		0.01		0.05	
3.655	≤1	4^+	3.656	4				0.34	
3.786	≤1	$(4,5)^+$	3.788	3				1.06	5^+
3.928	≤1	2^+	3.926	4		0.05		0.22	
4.042	≤1	$(7)^+$	4.042	4				0.13	6^+
4.127	≤1	3^-	4.128	5	0.04		0.07		
4.245	5	$2^+,3^-$	4.237	4	0.61		0.35		3^-
4.561	11		4.552	6	0.02		0.11		$(1\text{-}4)^-$
4.618	6		4.620	6	0.02		0.11		$(1\text{-}4)^-$
4.865	4	$(1^-,4^+)$	4.868	7		0.03	0.67		
4.936	6		4.936	8	0.05		0.87		$(1\text{-}4)^-$
5.189	≤1	(0,1,2)	5.194	11	0.04		0.47		$(1,2)^-$
5.321	10		5.311	8	0.96				$(2\text{-}3)^-$
			5.574	10	0.02		0.33		$(1\text{-}4)^-$
			5.776	9	0.05		0.34		$(1\text{-}4)^-$
5.981	10		5.979	8	0.12		0.59		$(2,3)^-$
6.113	10		6.107	9	0.02		0.22		$(1\text{-}4)^-$

Table 3.6: *Spectroscopic information from the $^{55}Mn(d,^3He)^{54}Cr$ reaction at an average incident energy of 45.6 MeV. New spin assignments shown have been made as discussed in the text. See footnote on p. 63.*

Chapter 4

Shell-model calculations and sum-rule analyses

In this chapter, results from shell-model calculations based on a new effective interaction for $A = 41$–66 nuclei [van94] are first compared with the experimentally measured proton pickup (this work) and stripping ([Mat68]) data on ^{55}Mn, in particular those data for fp-shell transfer. The formalisms based on the non-energy weighted sum rules (NEWSR) are reviewed next, followed by a discussion of the $0f_{\frac{7}{2}}$ transfer spin-distributions for proton transfer on ^{55}Mn. Analyses, based on the standard and symmetric forms of the NEWSR, of these spin distributions are then presented.

4.1 Shell-model calculations

The shell-model calculations assume an inert ^{40}Ca core and a model space consisting of

$$0f_{\frac{7}{2}}^{n}(1p_{\frac{3}{2}}0f_{\frac{5}{2}}1p_{\frac{1}{2}})^{m} + 0f_{\frac{7}{2}}^{n-1}(1p_{\frac{3}{2}}0f_{\frac{5}{2}}1p_{\frac{1}{2}})^{m+1}$$

configurations, with $n+m$ the number of valence nucleons outside the ^{40}Ca core for a given nucleus, n the maximum number of nucleons allowed in the $0f_{\frac{7}{2}}$ orbit by the Pauli principle, and m is the minimum number of valence nucleons outside this orbit. For ^{54}Cr, ^{55}Mn and ^{56}Fe, all the valence protons can be accommodated in the $0f_{\frac{7}{2}}$ orbit, and of the ten valence neutrons in

each case, a maximum of eight can be accommodated in the $0f_{\frac{7}{2}}$ orbit. Thus $m = 2$ for this study.

Spectroscopic factors associated with transitions from the ^{55}Mn ground-state to ^{54}Cr and ^{56}Fe final states were obtained by calculating the overlaps of the ^{55}Mn wave-function with the wave-functions obtained after operating on the ^{54}Cr wave-functions with the creation operator and on the ^{56}Fe wave-functions with the annihilation operator, respectively. The Oxford-Buenos Aires shell-model (OXBASH) code [Val91] was used to perform these calculations with matrix elements of the effective interaction [Hey94] fixed by the requirement of a best fit between experiment and theory for a large set of energy levels in $A = 41$–66 nuclei [van94].

4.1.1 Results

Calculated spectroscopic factors associated with transitions to ^{56}Fe and ^{54}Cr final states reached via single proton transfer on ^{55}Mn are shown in tables 4.1 and 4.2 respectively. No significant $0f_{\frac{7}{2}}$ stripping strength is predicted to lie above 3.737 MeV. This is in good agreement with Matoba's results (see table 4.3) which show the last fragment of $0f_{\frac{7}{2}}$ strength to be located at 3.78 MeV. The shell-model results also show negligible $0f_{\frac{5}{2}}$ and $1p_{\frac{1}{2}}$ pickup strength, thus supporting the assumption used in the DWBA analyses (section 3.5) that $\ell = 3$ and $\ell = 1$ transfers imply $0f_{\frac{7}{2}}$ and $1p_{\frac{3}{2}}$ transfers respectively.

4.2 Sum-rule analyses

4.2.1 Formalism

The sum-rule formalisms, based on the standard and symmetric forms of the NEWSR, which are used to evaluate the consistency of single-nucleon transfer data [Cle91, New95] are discussed next.

J'_k	E*	—— $\left[\frac{J'}{J_t}\right]$C^{2}S ——			
	(MeV)	$0f_{\frac{7}{2}}$	$1p_{\frac{3}{2}}$	$0f_{\frac{5}{2}}$	$1p_{\frac{1}{2}}$
		ℓ=3	ℓ=1	ℓ=3	ℓ=1
2_1	0.888	1.400	0.003	0.002	
4_1	2.107	0.215			
2_2	2.567	0.237	0.003	0.001	
2_3	3.148	0.033	0.007	0.002	0.002
4_2	3.162	0.071	0.011		
1_1	3.197	0.175	0.004		
3_1	3.316	0.016	0.002		
6_1	3.458	0.714			
2_4	3.527	0.004	0.091	0.007	0.025
3_2	3.585	0.041	0.004		
2_5	3.675		0.154	0.007	0.042
6_2	3.737	0.310			
3_3	4.044	0.001	0.173	0.006	0.062
4_3	4.176		0.030		
3_4	4.421	0.004	0.006	0.004	0.016
4_4	4.480		0.026	0.005	
3_5	4.608	0.007	0.450	0.036	0.099
6_3	4.614	0.076			
2_6	4.663	0.017	0.002	0.005	0.016
4_5	4.668	0.003	0.021		
3_6	4.814	0.002	0.090	0.011	0.007
1_2	4.903	0.037	0.158	0.001	
5_1	4.969			0.018	
1_3	5.042	0.006	0.034		
4_6	5.042	0.008	0.242	0.078	
5_2	5.061			0.016	
3_7	5.100	0.002	0.027	0.001	
1_4	5.400		0.034	0.003	

Table 4.1: *Calculated stripping strengths associated with transitions to positive parity states in ^{56}Fe via proton stripping on ^{55}Mn. J_t and J' denote target ground-state spin and final-state spins respectively; while E^* denotes excitation energy in the final nucleus. Results were obtained from a shell-model calculation using a new effective interaction for $A = 41$–66 nuclei [van94]. Shown are only those final states for which the spectroscopic strength associated with any ℓ transfer is ≥ 0.02.*

J_k'	E*	—— C^2S ——			
	(MeV)	$0f_{\frac{7}{2}}$	$1p_{\frac{3}{2}}$	$0f_{\frac{5}{2}}$	$1p_{\frac{1}{2}}$
		ℓ=3	ℓ=1	ℓ=3	ℓ=1
2_1	0.911	0.804	0.004	0.002	
4_1	1.902	1.186	0.002		
2_2	2.352	0.130	0.015		0.001
2_3	2.799	0.034	0.005		
4_2	2.808	1.096	0.021	0.001	
4_3	2.996	0.016	0.003	0.001	
6_1	3.049	0.278			
3_1	3.230	0.151	0.006		
3_2	3.438	0.046	0.001		
5_1	3.521	1.075		0.001	
4_4	3.602	0.050		0.001	
6_2	3.754	0.159			
4_5	4.278	0.087	0.001		
3_3	4.557	0.018	0.003		
5_2	4.701	0.034			
3_4	4.738	0.015			
6_3	4.990	0.026			

Table 4.2: *Calculated pickup strengths associated with transitions to positive parity states reached in ^{54}Cr via proton pickup on ^{55}Mn. The notation is the same as for table 4.1. Results were obtained from a shell-model calculation using a new effective interaction for $A = 41$–66 nuclei [van94]. Shown are only those final states for which the spectroscopic strength associated with any ℓ transfer is ≥ 0.02.*

Standard form

The starting point for this discussion is the standard form of the exact, model-independent NEWSR represented by

$$S^{+}_{J_n}(j) + (-1)^{2J_t+1}[J_n]\sum_{J_\alpha}\left\{\begin{array}{ccc} J_n & j & J_t \\ J_\alpha & j & J_t \end{array}\right\} S^{-}_{J_\alpha}(j) = \frac{[J_n]}{[J_t]} \qquad (4.1)$$

where

- $-$ and $+$ denotes pickup and stripping respectively;
- j and J_t are the total angular-momentum transfer and target ground-state spin, respectively;
- $[x] = 2x + 1$;
- J_α and J_n are the spins of final states reached by pickup and stripping, respectively;
- $\left\{\begin{array}{ccc} J_n & j & J_t \\ J_\alpha & j & J_t \end{array}\right\}$ is the $6j$ symbol, related to the Racah coefficient, W, via [Ros57]:

$$W(J_n j j J_\alpha; J_t J_t) = (-1)^{J_n+j+j+J_\alpha}\left\{\begin{array}{ccc} J_n & j & J_t \\ J_\alpha & j & J_t \end{array}\right\};$$

- and S_J denotes the partial spectroscopic sum[1] which is determined by summing all spectroscopic factors associated with transitions to the same final-state spin, J.

Equation 4.1 is then modified by the introduction of two renormalization constants, n^+ and n^-, to take into account possible errors in the absolute normalization of stripping and pickup spectroscopic factors respectively, as determined by DWBA analyses of the transfer data. This modified form of the standard NEWSR reads

$$n^{+}S^{+}_{J_n}(j) + (-1)^{2J_t+1}[J_n]\sum_{J_\alpha}\left\{\begin{array}{ccc} J_n & j & J_t \\ J_\alpha & j & J_t \end{array}\right\} n^{-}S^{-}_{J_\alpha}(j) = \frac{[J_n]}{[J_t]}. \qquad (4.2)$$

[1] So for example the partial sum S^{+}_{1} is obtained by summing all stripping spectroscopic factors associated with transitions to $J = 1$ final states.

The renormalization constants, n^+ and n^-, are related by the total sum rule:

$$n^+S^+(j) + n^-S^-(j) = n^+ \sum_{J_n} S^+_{J_n}(j) + n^- \sum_{J_\alpha} S^-_{J_\alpha}(j) = [j] \qquad (4.3)$$

which is obtained from equation 4.2 by summing over J_n. Equation 4.2 represents a set of $N = \min\{[J_t],[j]\}$ linear relations involving $2N$ partial sums $S^-_{J_\alpha}$ and $S^+_{J_n}$.

In applications of the sum rules, the uncertainty, ΔS, in a spectroscopic factor S is assumed proportional to S itself [Cle73, Cle91], with proportionality constant σ, the relative error parameter, so that

$$\Delta S = \sigma S. \qquad (4.4)$$

A measure of the goodness-of-fit to the sum rule corresponding to spin J_n is given by Q_{Jn} with expectation value zero, where

$$Q_{J_n} = n^+S^+_{J_n}(j) + (-1)^{2J_t+1}[J_n] \sum_{J_\alpha} \left\{ \begin{array}{ccc} J_n & j & J_t \\ J_\alpha & j & J_t \end{array} \right\} n^-S^-_{J_\alpha}(j) - \frac{[J_n]}{[J_t]}. \qquad (4.5)$$

Equation 4.4 and the standard error propagation formula (for example, [Mül84]) results in an uncertainty ΔQ_{J_n} in Q_{J_n} given by:

$$(\Delta Q_{J_n})^2 = \sigma^2 \left(\left(n^+S^+_{J_n}(j)\right)^2 + [J_n]^2 \sum_{J_\alpha} \left\{ \begin{array}{ccc} J_n & j & J_t \\ J_\alpha & j & J_t \end{array} \right\}^2 \left(n^-S^-_{J_\alpha}(j)\right)^2 \right). \qquad (4.6)$$

The above expressions lead to a condition for an acceptable overall fit to the N linear relations constituting the standard NEWSR, in which no sum rule is overemphasized at the expense of another [Cle91]. Setting $Q^2_{J_n} = \Delta Q^2_{J_n}$, dividing by $[J_n]$, and summing over J_n yields

$$\sum_{J_n} \frac{(Q_{J_n})^2}{[J_n]} = \sum_{J_n} \frac{(\Delta Q_{J_n})^2}{[J_n]} = \sigma^2 \left(\sum_{J_n} \frac{\left(n^+S^+_{J_n}\right)^2}{[J_n]} + \sum_{J_\alpha} \frac{\left(n^-S^-_{J_\alpha}\right)^2}{[J_\alpha]} \right). \qquad (4.7)$$

As a next step n^+ is written in terms of n^- using the total sum rule of equation 4.3, and σ^2 emerges as a function of the input spectroscopic factors and of n^-. The latter can then be varied to determine the minimum value of $\sigma = \sigma_{min}$. The smaller σ_{min} is, the better the fit to the sum rules is. A value

of $\sigma_{min} = 0.00$, for example, indicates that a perfect fit to the sum rules was obtained for unique values of n^- and n^+. For an acceptable fit [Cle91]

$$\sigma_{min} \leq 0.10. \tag{4.8}$$

If this criterion is satisfied it indicates that both stripping and pickup spin-distributions are consistent with the sum rules, to within the assumed uncertainties. The values of n^+_{min} and n^-_{min} determined via equation 4.7 can then be used to obtain estimates of absolute stripping and pickup spectroscopic factors. On the other hand a failure to fit the NEWSR points to inaccuracies in the stripping and/or pickup spin-distributions.

Symmetric form

An equivalent formalism to the one above based on a symmetric form of the NEWSR was recently developed and has been successfully used to analyse $0f_{\frac{7}{2}}$ transfer data on ^{51}V and ^{59}Co [New95]. The symmetric sum rules are represented by

$$\sum_{J'}(-1)^{J_t+j+J'} \left\{ \begin{array}{ccc} J & J_t & J_t \\ J' & j & j \end{array} \right\} \left\{ S^+_{J'} + (-1)^J S^-_{J'} \right\} = [j]^{\frac{1}{2}} [J_t]^{-\frac{1}{2}} \delta_{J0} \tag{4.9}$$

where J' now denotes final-state spin and J is constrained by

$$0 \leq J \leq (N-1). \tag{4.10}$$

Equation 4.9 represents a set of $N = \min\{[J_t], [j]\}$ linear relations in the partial sums $S^+_{J'}$ and $S^-_{J'}$. Unlike in the case of the standard NEWSR, the total sum rule (equation 4.3) is recovered by using only one of the N linear relations, namely the one for which $J = 0$. The remaining $N-1$ relations are thus decoupled from the total sum rule, thereby removing a bias which was present in the standard NEWSR formalism, i.e. that the observed strength necessarily exhausts the total sum rule.

The same steps which were used to establish the standard NEWSR formalism were followed in establishing the symmetric NEWSR formalism. The symmetric NEWSR of equation 4.9 are first modified by introducing the renormalization constants n^+ and n^-, to read:

$$\sum_{J'}(-1)^{J_t+j+J'} \left\{ \begin{array}{ccc} J & J_t & J_t \\ J' & j & j \end{array} \right\} \{ n^+ S^+_{J'} + (-1)^J n^- S^-_{J'} \} = [j]^{\frac{1}{2}} [J_t]^{-\frac{1}{2}} \delta_{J0}. \tag{4.11}$$

By putting $n = \frac{n^+}{n^-}$ in equation 4.11 for cases where $J > 0$, the $(N-1)$ linearly independent relations

$$\sum_{J'}(-1)^{J_t+j+J'} \left\{ \begin{array}{ccc} J & J_t & J_t \\ J' & j & j \end{array} \right\} \left\{ nS^+_{J'} + (-1)^J S^-_{J'} \right\} = 0 \qquad (4.12)$$

can then be used to assess the consistency of the experimentally obtained partial sums with the NEWSR by again introducing a quantity Q_J, which is defined as:

$$Q_J = \sum_{J'}(-1)^{J_t+j+J'} \left\{ \begin{array}{ccc} J & J_t & J_t \\ J' & j & j \end{array} \right\} \left\{ nS^+_{J'} + (-1)^J S^-_{J'} \right\} \qquad (4.13)$$

and which has zero expectation value. Once again, some scatter in the Q_J values is expected because the spectroscopic partial sums, $S^+_{J'}$ and $S^-_{J'}$, are themselves subject to some scatter about their true values. This scatter in Q_J, denoted by ΔQ_J, can be calculated using equations 4.4, 4.13 and the error propagation formula to give

$$(\Delta Q_J)^2 = \sum_{J'} \left\{ \begin{array}{ccc} J & J_t & J_t \\ J' & j & j \end{array} \right\}^2 \sigma^2 \left\{ n^2 (S^+_{J'})^2 + (S^-_{J'})^2 \right\}. \qquad (4.14)$$

To assess the accuracy of the transfer spin-distributions a goodness-of-fit indicator, χ^2, which is similar in form to the expression for the reduced chi-square (equation 3.12 divided by the number of degrees of freedom), is introduced. This goodness-of-fit indicator has the form

$$\chi^2 = \frac{1}{(N-2)} \sum_{J>0} \frac{Q_J^2}{(\Delta Q_J)^2}. \qquad (4.15)$$

The fit can now be optimized by varying n, thus determining the minimum value of $\chi^2 = \chi^2_{min}$, and the corresponding value of $n = n_{min}$. With $\sigma = 0.10$, a value of $\chi^2_{min} \leq 1$ implies that, using $n = n_{min}$, the set of $(N-1)$ linear relations of equation 4.12 are fitted to within 10% fractional uncertainties in the partial sums $S^+_{J'}$ and $S^-_{J'}$. Any such fit, obtained using only the seen strength below ~ 5 MeV excitation energy, implies that any unseen strength also satisfies equation 4.12, since the total strength must

certainly do so. It then follows [New95] that once n_{min} has been obtained, the total sum rule, together with an estimate of the fraction, γ, of unobserved strength total strength, can then be used to determine n^+ and n^- as is done below in section 4.2.4. Further, it should be noted that, given the structure of equation 4.12, a likely spin distribution for any unseen strength is one with $S_{J'} \propto [J']$ [New95]. Importantly, such unseen strength then makes no contribution to the dipole sum rule of equations 4.17 (see section 4.2.4).

4.2.2 $0f_{\frac{7}{2}}$ transfer spin-distributions

For the remainder of this chapter the $0f_{\frac{7}{2}}$ transfer strength is focussed on. The establishment of stripping and pickup spin-distributions which are required for the sum-rule analyses is discussed first.

Stripping

For the stripping strength a summary of the $\ell = 3$ spectroscopic information from Matoba's study [Mat68] which was previously given in table 1.3 is presented in table 4.3, together with the most recent adopted levels ($E^* < 4.0$ MeV) [Jun87, Jun92]. Except for the transition to the ^{56}Fe ground state (0^+), it was assumed that the $\ell = 3$ strength seen by Matoba is associated with $0f_{\frac{7}{2}}$ proton transfer. The negligible $0f_{\frac{5}{2}}$ strength below 4.0 MeV excitation predicted by the shell model (see table 4.1), supports this assumption.

The ^{56}Fe excited states at excitation energies of 0.85, 2.09 and 2.66 MeV as reported by Matoba correspond unambiguously with the adopted levels at 0.847, 2.085 and 2.658 MeV respectively. These three states have spins of 2^+, 4^+ and 2^+ respectively.

The mapping of the next three states reported by Matoba to the presently adopted ^{56}Fe levels is ambiguous because of a relatively large uncertainty of 40 keV associated with the excitation energies of these states. Matoba found an $\ell = 3$ stripping strength of 0.08 to be associated with the state-complex at (2.97 + 3.15) MeV. By considering only excitation energies, this strength could be associated with transitions to adopted levels at energies of 2.942 ($J' = 0^+$), 2.960 ($J' = 2^+$), 3.070 ($J' = (3^-)$), 3.120 ($J' = (1^+)$) or 3.123

— from Refs. [Jun87, Jun92] —			— from Ref. [Mat68] —			
E^* (MeV)	ΔE^* (keV)	J'^π	E^* (MeV)	ΔE^* (keV)	ℓ	$\frac{[J']}{[J_t]} C^2S$
0.0		0^+	0		3	0.01
0.847	< 1	2^+	0.85		3	1.45
2.085	< 1	4^+	2.09		3	0.36
2.658	< 1	2^+	2.66		3	0.14
2.942	< 1	0^+				
2.960	< 1	2^+				
			[a]2.97	40	3	0.04
3.070	30	(3^-)				
3.120	< 1	(1^+)				
3.123	< 1	4^+				
			[a]3.15	40	3	0.04
3.370	< 1	2^+				
3.388	< 1	6^+				
			3.40	40	3	0.90
3.748	5	2^+				
3.756	< 1	6^+				
3.760	10	(2-6)				
			3.78	40	3	0.25
3.832	< 1	2^+				

[a] Member of the state-complex at (2.97 + 3.15) MeV with combined $\ell = 3$ strength of 0.08.

Table 4.3: *Spectroscopic information on ℓ = 3 transfer stripping strength from the $^{55}Mn(\alpha,t)^{56}Fe$ reaction as reported by Matoba [Mat68]. The possible ^{56}Fe adopted levels [Jun87, Jun92] which correspond with observed states reached via ℓ = 3 transfer are shown. J_t and J' denote target ground- and final-state spin respectively. Note that the state-complex at (2.97 + 3.15) MeV is not indicated in Refs. [Jun87, Jun92] (see table 1.3).*

stripping			pickup		
J'	E^* (MeV)	$\frac{[J']}{[J_t]}\, C^2S$	J'	E^* (MeV)	C^2S
2^+	0.847	1.45	2^+	0.835	0.85
4^+	2.085	0.36	4^+	1.824	0.99
2^+	2.658	0.14	2^+	2.622	0.02
2^+	2.960	[a]0.027	2^+	3.076	0.09
1^+	3.120	[a]0.027	4^+	3.159	0.84
4^+	3.123	[a]0.027	[d]6^+	3.220	0.27
[b]6^+	3.388	0.90	2^+	3.429	0.05
2^+	3.748	[c]0.125	4^+	3.656	0.34
6^+	3.756	[c]0.125	[d]5^+	3.788	1.06
			2^+	3.926	0.22
			[d]6^+	4.042	0.13

[a] Strength of 0.08 distributed equally over final-state spins of 1^+, 2^+ and 4^+ as discussed in text.

[b] Assignment made on basis of Matoba's suggestion [Mat68], sum-rule analyses and shell-model calculations as discussed in text.

[c] Strength of 0.25 distributed equally over final-state spins 2^+ and 6^+ as discussed in text.

[d] Spin assignments made as discussed in text.

Table 4.4: *Spectroscopic factors for $0f_{\frac{7}{2}}$ proton transfer on ^{55}Mn associated with final states of spin J' at excitation energy E^* in the final nucleus. The partial sums $S^+_{J'}$, $S^-_{J'}$, used in the text are obtained by summing over final states of the same spin J'. The excitation energies of final states reached via stripping were obtained from Refs. [Jun87, Jun92] while those for pickup final states were obtained from this study.*

($J' = 4^+$) MeV. ^{55}Mn has a ground-state spin $\frac{5}{2}^-$, and if it is assumed that an $\ell = 3$ transfer implies a transfer of a proton to the $0f_{\frac{7}{2}}$ subshell, the only possible transitions are to the 2.960, 3.120 and 3.123 MeV states. The small stripping strength of 0.08 was therefore shared equally amongst final-state spins of 1^+, 2^+ and 4^+.

The state seen by Matoba at 3.40 MeV could correspond to adopted levels at excitation energies of 3.370 MeV ($J' = 2^+$) or 3.388 MeV ($J' = 6^+$), with the latter being the one suggested by Matoba [Mat68]. If it is assumed that this is a 2^+ state, a significant deterioration in the quality of NEWSR fits results. Furthermore the shell-model results shown in table 4.1 indicate the presence of a strong transition to a 6^+ ^{56}Fe final state at an excitation energy of 3.458 MeV. It was therefore assumed that this state corresponds to the adopted level at 3.388 MeV. The spectroscopic strength of 0.90 was therefore associated with a 6^+ final state.

The state seen by Matoba at 3.78 MeV could correspond with adopted levels at excitation energies of 3.748 ($J' = 2^+$), 3.756 ($J' = 6^+$) or 3.760 (J' = (2–6)) MeV. In view of this and the uncertainties in parity assignments to the 3.760 MeV state, the strength of 0.25 associated with Matoba's state at 3.78 MeV was shared equally between 2^+ and 6^+ final states.

Pickup

For the particle occupancy in ^{55}Mn of proton orbits other than the $0f_{\frac{7}{2}}$, table 3.6 shows that the summed $1p$ strength observed in the ^{55}Mn(d,^{3}He)^{54}Cr reaction is 0.24. Further, the weak excitation of the ^{54}Cr ground state (0^+) in this reaction strongly suggests a similarly small $0f_{\frac{5}{2}}$ occupancy. These observations are in line with the shell-model findings that for ^{55}Mn the $1p_{\frac{3}{2}}$ proton occupancy is 0.06, and that the $1p_{\frac{1}{2}}$ and $0f_{\frac{5}{2}}$ proton occupancies are negligible.

For the $0f_{\frac{7}{2}}$ pickup strength, as shown in table 3.6, three ^{54}Cr final states observed which are reached via $\ell = 3$ transfer have uncertain spin assignments. An $\ell = 3$ pickup strength of 0.13 was found for the transition to the ^{54}Cr state observed at 4.042 MeV. This state corresponds with the adopted level at 4.042 MeV which has an uncertain spin assignment of $(7)^+$.

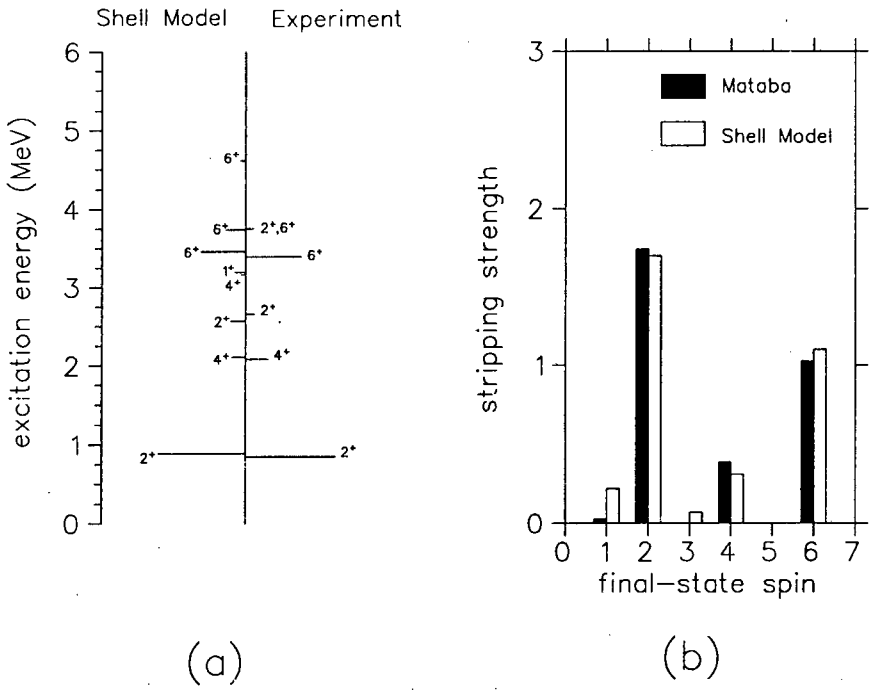

Figure 4.1: *Comparison of results from a recent 0f1p shell-model calculation with the $0f_{\frac{7}{2}}$ proton stripping spectroscopic strength shown in table 4.4. In (a) spectroscopic strength is plotted versus ^{56}Fe excitation energy while the summed spectroscopic strength is plotted versus ^{56}Fe final-state spin in (b). Only those final states for which spectroscopic strength is > 0.05 are shown.*

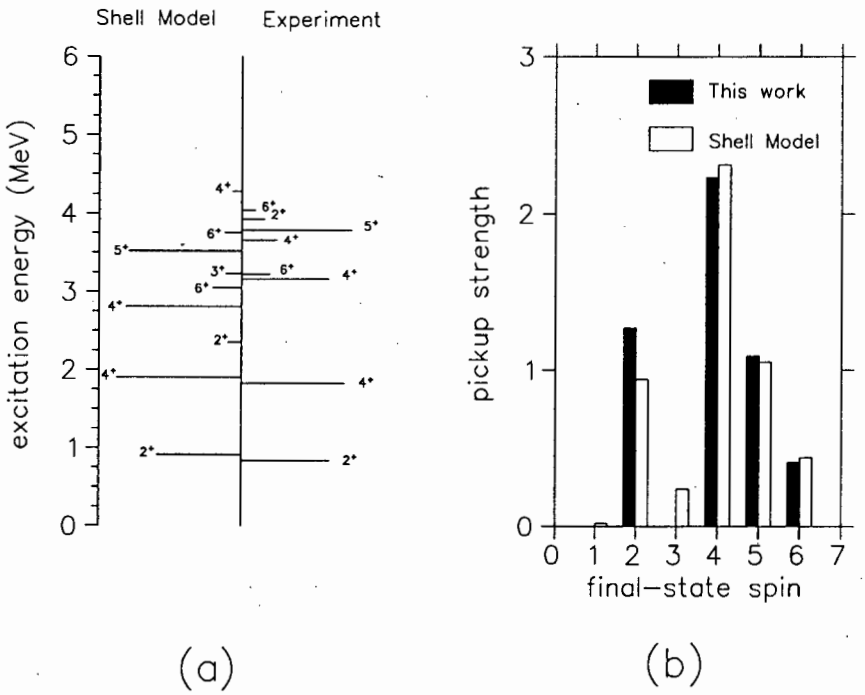

Figure 4.2: *Comparison of results from a recent 0f1p shell-model calculation with the $0f_{\frac{7}{2}}$ proton pickup spectroscopic strength shown in table 4.4. In (a) spectroscopic strength is plotted versus ^{54}Cr excitation energy while the summed spectroscopic strength is plotted versus ^{54}Cr final-state spin in (b). Only those final states for which spectroscopic strength is > 0.05 are shown.*

However, the angular distribution for pickup to this state is unambiguously $\ell = 3$, and this limits the spin of this state to $1^+ \leq J' \leq 6^+$. It is therefore unlikely that the 4.042 MeV state has a spin of 7^+. Gamma decay selection rules favour a large value of the spin. The shell-model results shown in table 4.2 indicate a 6^+ state at 3.754 MeV with a pickup strength of 0.16. In view of the above a spin assignment of 6^+ was made to the 4.042 MeV state.

The next uncertain spin assignment was the one associated with the state observed at an excitation energy of 3.788 MeV. This excitation energy is consistent with that of the adopted level at 3.786 MeV which has a $(4,5)^+$ spin assignment. There is also a ^{54}Cr adopted level at 3.799 MeV $\sim$ 13 keV away from the 3.786 MeV state which could not be resolved experimentally. However, this level is known to have a spin of 4^+, so that the pickup strength of 1.06 must be associated solely with final-state spins of 4^+ or 5^+. The shell-model calculations predict a significant fragment of strength (1.08) to be located in a 5^+ state at an excitation of 3.521 MeV. Also, unless it is assumed that the bulk of the experimentally observed strength is associated with a 5^+ final state, very poor fits to the NEWSR are obtained. A spin assignment of 5^+ was thus made to the adopted level state at 3.786 MeV, and the 4^+ state at 3.799 MeV was assumed not to have been seen. The possibility that the 3.799 MeV state is excited but is not resolved will be explored further below.

Finally, the adopted level observed at 3.220 MeV in this study has an uncertain spin assignment of $(6)^+$. This level, which has an associated strength of 0.27, most likely corresponds to the shell-model level 6^+ state at 3.049 MeV which has an associated strength of 0.278. Changing this spin assignment would also result in a significant deterioration of the sum-rule fits.

A summary of all the spin assignments made to ^{56}Fe and ^{54}Cr final states as discussed above, are tabulated in table 4.4, and are compared with the corresponding results of the shell-model calculation in figures 4.1 and 4.2. Figures 4.1(a) and 4.2(a) compare the experimental and shell-model distributions of the $0f_{\frac{7}{2}}$ proton spectroscopic strength as a function of final-state excitation energy and spin, while figures 4.1(b) and 4.2(b) compare

the corresponding summed strengths as a function of final-state spin. The overall agreement is good, particularly in the latter case.

4.2.3 Results

The results of the NEWSR analyses of the $0f_{\frac{7}{2}}$ transfer spin-distributions discussed above are shown graphically in figures 4.3 (standard form) and 4.4 (symmetric form).

There is a clear minimum in curve I of σ versus the pickup renormalization constant, n^-, (figure 4.3) obtained for the pickup spin-distribution given in table 4.4. A minimum σ of 12% was obtained while the corresponding value of n^- was 0.98. The sum rule fit criterion, $\sigma \leq 0.10$, was therefore not satisfied with this spin distribution. Distinct minima are also seen in figure 4.4 in which the curves of χ^2 as a function of the ratio of renormalization constants, $n(=\frac{n^+}{n^-})$ are shown. Here again curve I corresponds to the pickup spin-distribution given in table 4.4. The minimum value of χ^2 was found to be 3.6 for $n = 0.89$. The minimum value of χ^2 exceeds the fit criterion by a factor of ~ 4. Although the fits obtained are poorer than those obtained in previous studies [Cle91, New95], they are still reasonable. This is illustrated in figure 4.5 where the sensitivity of the NEWSR to an arbitrary change in the stripping spin-distribution is shown.

It should be stressed here that the standard NEWSR analyses employ a different fit criterion to the one used in the symmetric NEWSR analyses. In the former, the criterion on the value of σ^2 obtained from equation 4.7 damps out the effect of an anomalously poorly fitted sum rule, whereas in the symmetric sum-rule analyses the standard χ^2 test of equation 4.15 retains any such effect. Thus in the symmetric sum-rule analysis, it is the sum rule with $J = 3$ in equation 4.12 which makes an anomalously large contribution to the value of χ^2 as given by equation 4.15.

As pointed out earlier, a failure to satisfy the NEWSR is indicative of inaccuracies in the spin distributions of transfer strength. These inaccuracies can arise from one or more of the following:

- wrongly assigning spectroscopic strength because of the ambiguity stemming from the fact that one ℓ transfer can be associated with

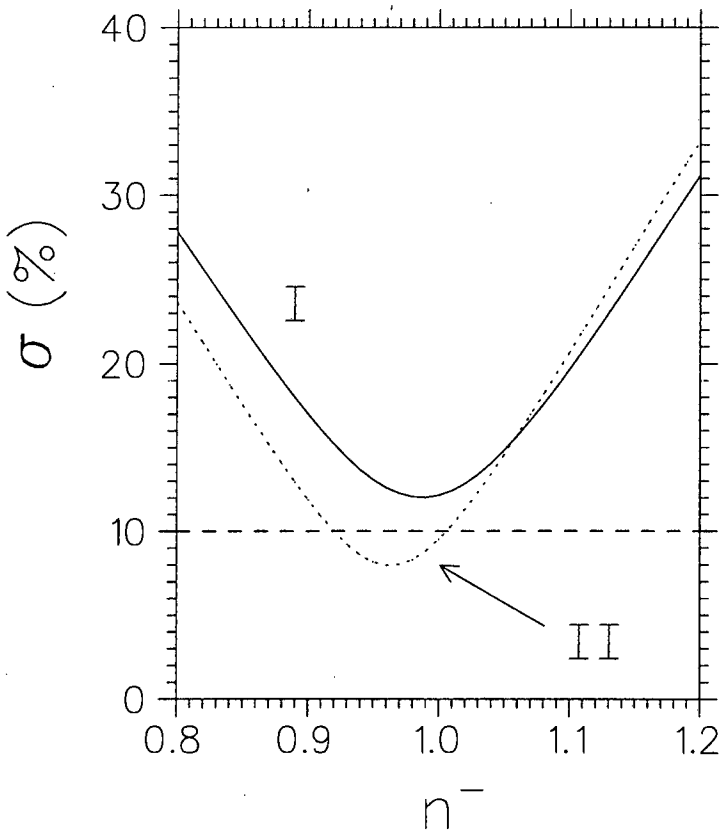

Figure 4.3: *Plot of relative spectroscopic factor error parameter, σ, versus renormalization constant, n^-. Curve I was obtained using the data shown in table 4.4 while curve II was obtained after relocating 17% of the pickup strength associated with the 3.786 MeV 5^+ final state to the 3.799 MeV 4^+ final state (see text for details).*

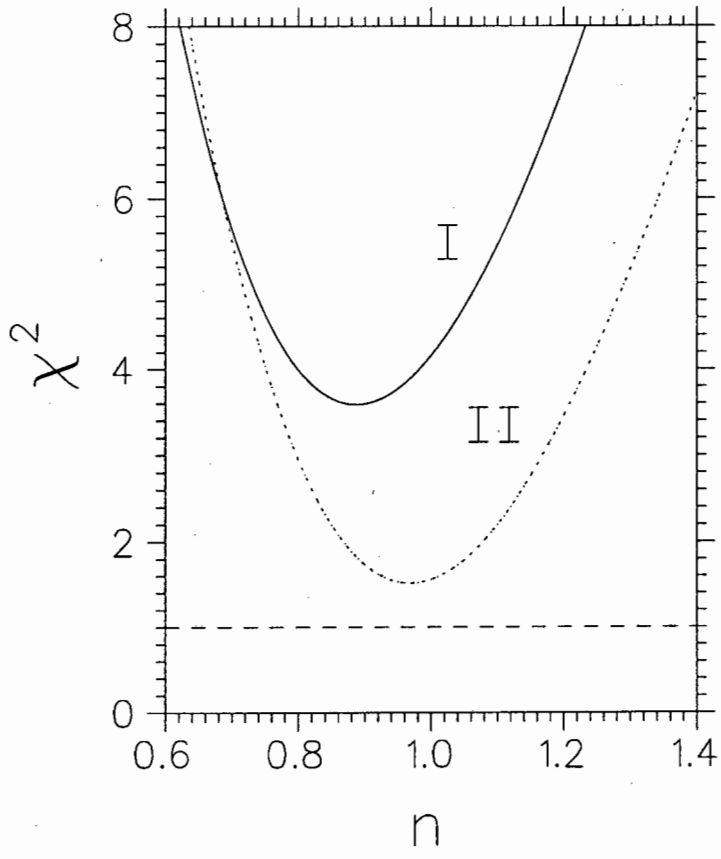

Figure 4.4: *Plot of goodness-of-fit indicator, χ^2, versus normalization n. Curve I was obtained using the data shown in table 4.4 while curve II was obtained after relocating 17% of the pickup strength associated with the 3.786 MeV 5^+ final state to the 3.799 MeV 4^+ final state (see text for details).*

more than one j transfer,

- the location of significant transfer spectroscopic strength at excitation energies greater than $\sim$ 5.0 MeV.
- scatter at more than the 10% level in pickup and/or stripping relative spectroscopic factors, or
- one or more inaccurate spin assignments to final states reached by pickup or stripping.

Although possible, it is unlikely that the $\ell = 3$ stripping strength was wrongly associated with $0f_{\frac{7}{2}}$ rather than $0f_{\frac{5}{2}}$ transfer. The small strength of 0.01 associated with the transition to the ^{56}Fe ground state (0^+) and the absence of excitation of the 0^+ state ($E^* = 2.941$ MeV) supports this assumption. As pointed out in the previous chapter, a similar argument involving the ^{54}Cr ground state (0^+) and the 0^+ states at 2.830 MeV and 4.013 MeV excitation, holds for the pickup case. It is therefore unlikely that the first possible source of inaccuracy listed above is playing a role in this work.

Although some spin assignments were made by comparing experimental with shell-model spectroscopic information and NEWSR analyses, the majority of spin assignments were made using the adopted levels for ^{54}Cr and ^{56}Fe. Although possible, it is unlikely that errors exist in spin assignments to final states which have unique, unambiguous spin assignments according to the adopted levels. This possibility will therefore not be further explored.

The sensitivity of the sum rules to the manner in which the 0.08 and 0.25 stripping strength was shared amongst 1^+,2^+,4^+ and 6^+ states, as described above was investigated using the standard form of the NEWSR. This was done using pickup spin-distribution given in table 4.4 and

- allocating all the 0.08 strength to either 1^+,2^+ or 4^+ final states and
- allocating all the 0.25 strength to either 2^+ or 6^+ final states.

A study of all possible permutations of the above, has yielded minimum values of σ varying between 11% and 14%. The "equal sharing" of stripping strength as described above is therefore not critical.

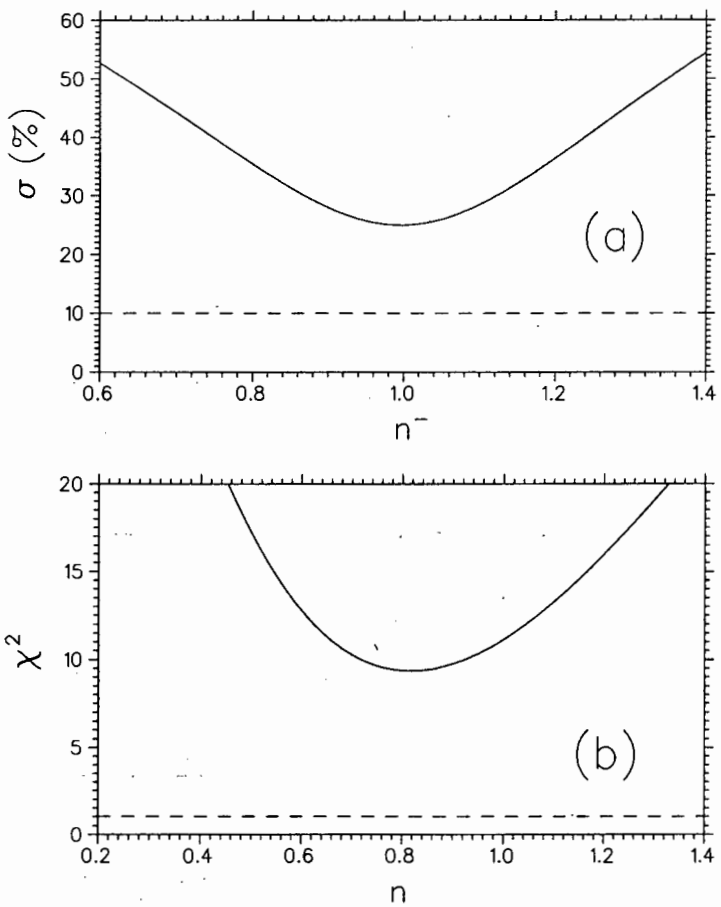

Figure 4.5: *Plots illustrating the sensitivity of the NEWSR to the spin distribution. The curves shown were obtained after arbitrarily assigning all the stripping strength associated with 4^+ final states, amounting to $\sim$ 5% of the total sum-rule strength, to 3^+ final states. (a) Plot of relative error parameter, σ, versus pickup renormalization constant, n^-. (b) Plot of goodness-of-fit indicator, χ^2, versus normalization n.*

However, the fit to the sum rules turns out to be particularly sensitive to a transfer of strength from the partial sum S_5^- to the partial sum S_4^-. Of course, other possibilities of reducing the original discrepancy exist, but a virtue of applying the sum rules is to focus attention on likely candidates. In the present case, the obvious focus is on S_4^- and S_5^- partial spectroscopic sums. In this regard the possibility that the strong 5^+ state seen at 3.788 MeV excitation in ^{54}Cr could be masking some strength to the 3.799 MeV (4^+) state, was investigated. This was done by attempting to deconvolute the yield which in the analysis above was assumed to be associated with the 3.786 MeV $(4,5)^+$ adopted level. Pickup data for which the resolution was the highest, namely 32 keV, were used. As a first step a Gaussian function was fitted to the region of interest in ^{54}Cr spectrum, with its width and centroid parameters fixed. The width was fixed to a mean width determined from fits to resolved states in the vicinity of 3.786 MeV excitation, while the position was fixed to that expected for the 3.786 MeV adopted level using the momentum calibration. The resulting fit with an associated reduced χ^2 of 4.43 is shown in figure 4.6. Two Gaussian functions were then fitted to the region of interest using the same width parameters. The positions were fixed at 3.786 and 3.799 MeV. In this case a reduced χ^2 of 2.78 was obtained. The fit obtained is also shown in figure 4.6. Using these fits, it was possible to establish the relative intensity of the state at 3.799 MeV excitation w.r.t. the 3.786 MeV state. An intensity ratio of 20:100 was obtained. Although the reduced χ^2 obtained is lower using two Gaussians, the full-width at half maximum (FWHM) of the superposition is bigger than the average FWHM for this run. It does however fall within three standard deviations of the average FWHM. Since the FWHM obtained using two Gaussians is consistent to within statistical uncertainty, with that obtained using only one Gaussian, it is unlikely that the 3.799 MeV state is excited. In view of this, the intensity ratio was taken to represent an upper limit. No lower limit on the relative intensities could however be established.

The quoted intensity ratio was nevertheless used to relocate[2] 17% of the pickup strength (1.06) initially assumed to be associated with the transition

[2]It has been argued above that the 3.786 MeV $(4,5)^+$ is a 5^+ state.

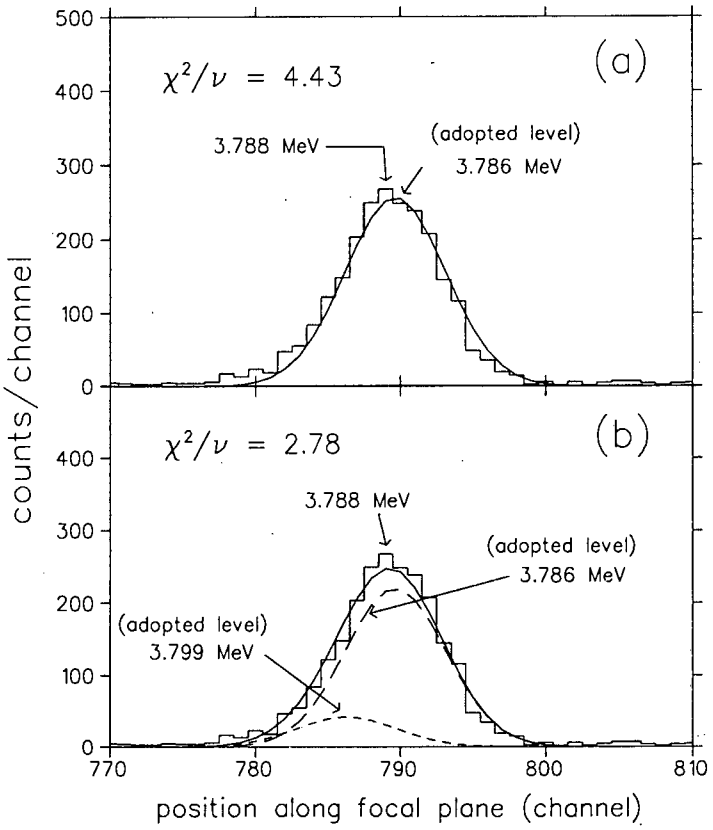

Figure 4.6: *(a) Gaussian fit to the ^{54}Cr final state observed at 3.788 MeV excitation. (b) A fit to the same peak using two Gaussian functions. The solid curve represents a superposition of these Gaussians (see text for discussion).*

to 3.786 MeV adopted level, from 5^+ to 4^+ final states. Fits to both the standard and symmetric sum rules improve when using the pickup spin-distribution given in table 4.4 modified in this manner. The NEWSR results are shown graphically in figures 4.3 and 4.4 as curves II. With this distribution a minimum σ of 8.0% for $n^- = 0.96$ is obtained, thus satisfying the fit criterion associated with the standard NEWSR formalism. The corresponding symmetric sum rule results show a minimum χ^2 of 1.6 for $n = 1.06$, just failing to satisfy the symmetric NEWSR fit criterion. The sum rule results therefore suggest that the ^{54}Cr level at 3.799 MeV excitation will be observed if the total instrumental resolution is sufficiently good (~15 keV) in order to resolve it from the level at 3.786 MeV. However

because of the absence of a lower limit on the ratio of intensities of the 3.786 to 3.799 MeV states, no conclusive statement can be made about whether the 3.799 MeV state is seen.

4.2.4 Estimate of absolute normalizations

With n_{min} determined from the symmetric NEWSR analyses described above, estimates of the absolute normalizations required for the stripping and pickup data of table 4.4 can be extracted [New95], given an estimate of the fraction, γ, of the total $0f_{\frac{7}{2}}$ proton strength that resides outside the excitation energy region probed by the transfer experiments. These normalization factors, which will be denoted as $n^{+}_{\rm abs}$ and $n^{-}_{\rm abs}$ respectively, were estimated using a modified form of the total sum rule (equation 4.3):

$$n^{+}_{\rm abs}S^{+} + n^{-}_{\rm abs}S^{-} = [j](1-\gamma) \qquad (4.16)$$

where $n_{min} = \frac{n^{+}_{\rm abs}}{n^{-}_{\rm abs}}$.

Analyses of $(e,e'p)$ data have suggested that γ could be as large as $\sim$ 50% [Wag90]. More recent analyses of $(e,e'p)$ data [Jin92] and theoretical considerations [Mah91] point to γ being smaller at $\sim$ 30% and possibly still smaller, while dipole sum rule fits to transfer data [Cle91] and studies of the decay of analogue states [van89] indicate γ to be $\sim$ 10%. For this study γ was taken as 0.2 ± 0.1 in order to straddle the various estimates. With $n_{min} = 0.89$ from curve I of figure 4.4 and this value of γ, it was found that the stripping and pickup data of table 4.4 should be multiplied by $n^{+}_{\rm abs} = 0.74 \pm 0.09$ and $n^{-}_{\rm abs} = 0.83 \pm 0.10$ respectively. In order to assess the accuracy of these normalizations, the diagonal contributions of the $0f_{\frac{7}{2}}$ proton orbit to various one-body observables was calculated, in particular J^{c}_{t}, the contribution to J_t, the maximum z-projection of the spin of the ^{55}Mn ground state. This was done using the dipole sum rule [Cle91], which in the case of pickup data, is given by

$$J^{c}_{t} = \frac{1}{2(J_t+1)} \sum_{J'} \left\{ J_t(J_t+1) + j(j+1) - J'(J'+1) \right\} n^{-}_{\rm abs} S^{-}_{J'} \qquad (4.17)$$

where, once again, J_t is the target ground-state spin ($J_t = 2.5$ in the case of ^{55}Mn), J' is the final-state spin, j is the spin of the orbital involved in

γ	J_t^c		
	pickup	stripping	average
0.2 ± 0.1	2.34 ± 0.29	1.76 ± 0.22	2.05 ± 0.21

Table 4.5: *Results of dipole sum-rule analyses of $0f_{\frac{7}{2}}$ proton transfer data (see table 4.4) on ^{55}Mn.*

the nucleon transfer and $n^-_{\rm abs}S^-_{J'}$ is the absolutely normalized spectroscopic partial sum associated with spin J'. The corresponding sum rule for the stripping case has an identical form. By averaging the results obtained for the cases of pickup and stripping, a value of $J_t^c = 2.05 \pm 0.21$ was obtained (see table 4.5). As far as other fp valence orbits are concerned, results indicate that their contribution to J_t^c is negligible. By equation 4.16, for a given n_{min}, increasing $(1-\gamma)$ results in corresponding fractional increases of $n^+_{\rm abs}$ and $n^-_{\rm abs}$, and thus of J_t^c by equation 4.17. A value of $\gamma \sim 0$ would then reproduce $J_t^c \sim 2.5$.

Thus, in common with other sum-rule analyses in the lower fp shell [Cle91], the transfer data is consistent with the simple picture in which the $0f_{\frac{7}{2}}$ orbit is being preferentially filled, with the low-lying spectroscopic strength close to the corresponding shell-model values. This is at odds with the spectroscopic factors for pickup from valence orbits determined using the $(e,e'p)$ reaction on medium-mass nuclei [den88b, Kra89]. Although some enhancement of the latter may be in order [Udí93, Udí95], it should also be kept in mind that the estimate of $\gamma \sim 0$ from the dipole sum rule (equation 4.17) is model dependent, in particular in the spin distribution assumed for the unseen strength (see section 4.2.1).

Chapter 5

Conclusion

In conclusion, the main results obtained from this study of single proton transfer on ^{55}Mn are first summarized and discussed. Thereafter possible complementary further studies are suggested.

5.1 Summary

Angular distributions for the ^{55}Mn(d,^{3}He)^{54}Cr and ^{55}Mn(d,d)^{55}Mn(g.s.) reactions were measured at an average incident energy of 45.6 MeV. Analyses of the pickup angular distributions made using the distorted-wave Born approximation (DWBA) formalism have yielded spectroscopic factors associated with the twenty-four ^{54}Cr states observed up to 6.107 MeV excitation. An optical-model analysis of the deuteron elastic scattering data has been performed to yield optimum values of the potential parameters used in obtaining the distorted wave-functions for the entrance channel in the DWBA calculations.

The $0f_{\frac{7}{2}}$ pickup spin-distribution required for the non-energy weighted sum-rule (NEWSR) analyses, was obtained using the $\ell = 3$ strength observed below 4.2 MeV excitation, in conjunction with the spins of adopted ^{54}Cr levels. Three of the adopted levels seen had uncertain spin assignments. Sum-rule fits and comparisons with the shell-model results were used to make spin assignments of 6^+, 5^+ and 6^+ to these levels which are located

at excitation energies of 3.222 ($(6)^+$), 3.786($(4,5)^+$) and 4.042 ($(7)^+$) MeV respectively.

Stripping spectroscopic factors for $0f_{\frac{7}{2}}$ transfer were obtained from a study by Matoba [Mat68] while corresponding ^{56}Fe final-state spins were obtained from the adopted levels. Because of relatively large uncertainties associated with the excitation energies of final states seen by Matoba, it was not possible to uniquely assign the $0f_{\frac{7}{2}}$ stripping spin-distribution. However, the relatively large strength (0.90) associated with a state seen at 3.40 MeV, was shown to most likely associated with the excitation of the 6^+ ^{56}Fe level at 3.388 MeV.

The results of shell-model calculations using a new effective interaction for $A = 41$–66 nuclei [van94] are in good agreement with the $0f_{\frac{7}{2}}$ transfer spin-distributions used. NEWSR analyses, using both the standard and symmetric forms of the spectroscopic sum rules, were made using these spin distributions. Acceptable fits to the NEWSR were obtained, but the quality of fits were poorer than for those obtained in previous studies [Cle91, New95].

5.2 Possible further studies

An examination of pickup spectra in the vicinity of the ^{54}Cr adopted level at 3.786 MeV excitation has not excluded the possibility that the 4^+ level at 3.799 MeV is excited but not resolved. If it is assumed that this state is indeed present and that 17% of the spectroscopic strength associated with the observed state at 3.788 MeV excitation is assigned to this 4^+ state, significant improvement in the quality of the NEWSR fits are observed. Higher resolution ($\sim$ 15 keV) measurements of proton pickup data on ^{55}Mn will be instrumental in addressing this uncertainty.

An additional set of stripping spectroscopic factors for proton transfer on ^{55}Mn will facilitate a further assessment of the assumptions made in this study regarding the $0f_{\frac{7}{2}}$ stripping spin-distribution. In this regard high resolution studies of the ^{55}Mn(α,t)^{56}Fe and ^{55}Mn(^{3}He,d)^{56}Fe reactions are possibilities.

The use of a polarized beam would allow the assignment of unique total angular momentum transfer, j, in contrast to the approach used in this

study where it was assumed that an $\ell = 3$ signature was sufficient to assign a j transfer of $\frac{7}{2}$. Although the observed weakness of transitions to 0^+ final states is consistent with a small $0f_{\frac{5}{2}}$ occupancy in ^{55}Mn, measurements with a polarized beam would facilitate the direct determination of this occupancy. It is however unlikely that a focal-plane polarimeter for the NAC k = 600 spectrometer will be available in the foreseeable future.

As discussed in the introductory chapter, the number of sum rules and thus the efficiency in comparing the theoretical and observed spin distributions of transfer strength, depends on the target ground-state spin (J_t) and j. ^{47}Ti is the sole remaining target in the lower fp shell with $J_t \geq \frac{5}{2}$ and a study of single proton (and/or neutron) transfer on this nucleus will thus represent the completion of a major program of experimental and theoretical work which has been dedicated to studying $0f_{\frac{7}{2}}$ nucleon transfer on fp-shell nuclei. It would then be possible to draw global conclusions concerning the $0f_{\frac{7}{2}}$ occupancies for these nuclei.

Finally, there is scope for some improvement in the symmetric NEWSR formalism, particularly in relation to the assumption that the error associated with a relative spectroscopic factor is proportional to the latter. This is at present being investigated.

Appendix A

VDC Spatial Resolution

The position accuracy, σ_x, obtainable with a single drift cell is the usual figure-of-merit reported for a VDC [Ber77]. It is a factor which contributes to the overall position resolution achievable with the spectrometer and also determines the angle accuracy, σ_θ, which can be achieved with the VDC.

A schematic representation of a charged particle trajectory traversing a VDC, having a signal-wire spacing s is shown in figure A.1. In the trajectory shown, six primary ionizations in the gas-filled VDC were caused, each associated with a separate drift cell. The drift time from the point of primary ionization to the point where avalanching occurs in each cell is measured experimentally. By using the time-to-position relationship provided by a lookup table it is possible to determine the position along the drift cell where the primary ionization occurred. It is therefore possible to reconstruct trajectories of particles across the VDC wire-plane. Since the trajectories of particles in the vicinity of the VDC are to a good approximation straight lines, the slope of each trajectory should be constant. This property of the trajectories was used to determine σ_x.

The slope of the trajectory shown in figure A.1 can be calculated in a number of ways. One way in which this can be done is to use the drift distances associated with two adjacent wires, say wires a and b. In this case the trajectory slope, S, is given by:

$$S_{a,b} = \frac{d_b - d_a}{s}, \tag{A.1}$$

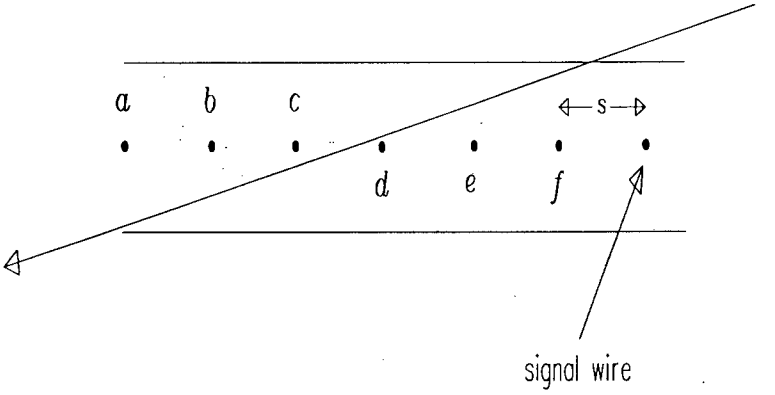

Figure A.1: *Schematic representation of a trajectory associated with a charged particle intersecting the VDC resulting in a six-wire event.*

where d denotes drift distance. The slope could also be determined using the drift distances associated with for example wires e and f. Since the slope should be constant, the difference between the two slopes, denoted by D, given by

$$D = S_{a,b} - S_{e,f} \tag{A.2}$$

should ideally be zero. However because of statistical fluctuations a distribution centered around zero is obtained when one calculates the difference in slope for a number of events. Let us denote the standard deviation of this distribution by σ_d. By applying the general law of error propagation to equation A.2, with covariances assumed to be zero, one obtains:

$$\Delta D^2 = \Delta d_a^2 + \Delta d_b^2 + \Delta d_e^2 + \Delta d_f^2. \tag{A.3}$$

If each Δ appearing in equation A.3 is replaced by its mathematical expectation, namely a standard deviation, and it is assumed that

$$\Delta d_a = \Delta d_b = \Delta d_e = \Delta d_f, \tag{A.4}$$

σ_d is then related to the intrinsic cell accuracy, σ_c, by [Ber77]

$$\sigma_c = 2\sigma_d. \tag{A.5}$$

The relationship between intrinsic cell accuracy and the cell position accuracy is given by [Ber77]

$$\sigma_x = \frac{\sigma_c}{\sqrt{n}}, \tag{A.6}$$

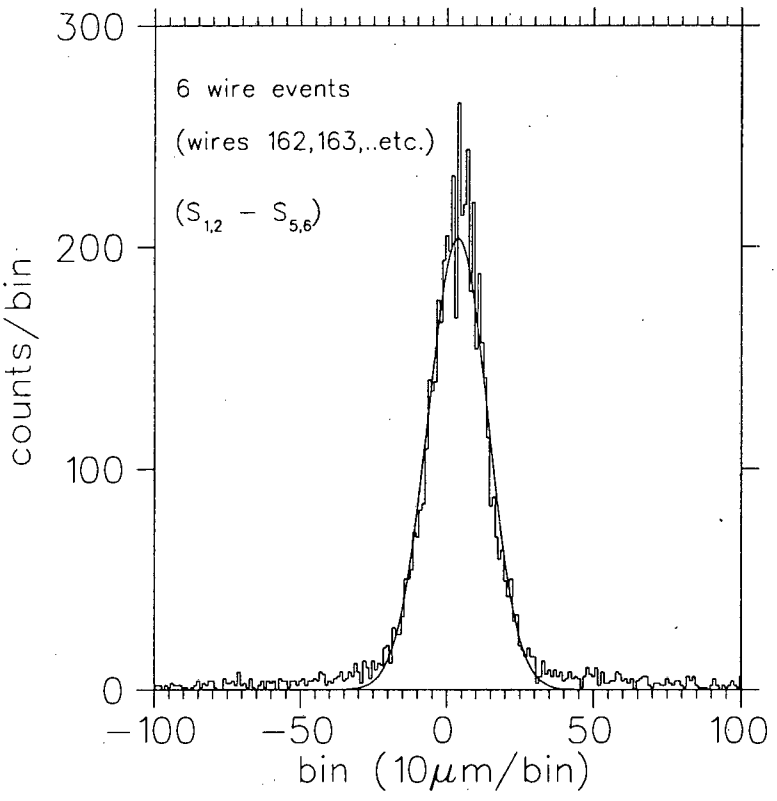

Figure A.2: *Typical result obtained after fitting a Gaussian lineshape to a distribution of differences in slope D.*

distribution no.	FWHM (μm)	type B uncertainty (%)
1	239.5	1.3
2	220.2	1.3
3	239.0	1.3

Table A.1: *FWHM($= 2.35\sigma_d$) associated with the three distributions of D, obtained by fitting Gaussians lineshapes to the distributions as described in the text. The type B (non-statistical) uncertainty quoted was obtained using the MINOS subroutine in MINUIT [Jam75, Jam89].*

where n is the number of points used to determine the trajectory.

For this analysis 6000 events associated with the ^{55}Mn(d,d)^{55}Mn(g.s.) reaction at a beam energy of 46 MeV and $\theta = 16°$ were used. These data were acquired with the VDC operated in the manner detailed in section 2.3.1. Each event selected was a six-wire event. Three distributions of D were obtained. The first was obtained using $S_{1,2}$ and $S_{5,6}$, the second using $S_{2,3}$ and $S_{4,5}$ and third using $S_{1,2}$ and $S_{4,5}$. Each distribution was fitted with a Gaussian lineshape in order to determine its associated standard deviation, σ_d. A typical fit to one of the distributions is shown in figure A.2. The results obtained from the fitting procedure are summarized in table A.1. Taking the average of these results one obtains, via equation A.5, a mean intrinsic cell accuracy (σ_c) of 198.2 $\pm$ 9.4 $\pm$ 2.6 μm, where the uncertainties are of types A (statistical) and B (non-statistical) respectively. From equation A.6 it is seen that the position accuracy is dependent on the number of drift cells, n, used to reconstruct the trajectory. In this work n varied between 3 and 10 (see appendices B and C). An average cell position accuracy (σ_x) achievable with the VDC was calculated by assuming that six drift cells were used to calculate the focal plane position. By using this assumption the mean position accuracy was found to be $\sim$ 80.9 μm.

Appendix B

VDC Wire Hit-analysis

In order to select valid VDC events it was necessary to know how many VDC signal wires are expected to register hits when a charged particle of interest traverses the focal plane. The expected number of wires firing is a function of:

- the geometry of the entrance collimator to the spectrometer,
- the angle of a particle's trajectory w.r.t. the spectrometer focal plane,
- the VDC geometry and
- the VDC operating high voltages used.

A schematic representation of the VDC geometry used is shown in figure B.1. In this figure $\theta_{\text{f.p.}}$ denotes the angle which the charged particle trajectory makes w.r.t. the VDC, s denotes the VDC signal wire spacing, l denotes half the separation between the aluminium high voltage (HV) planes and w denotes the effective signal-wire cell width. For the VDC used in this work (detailed in section 2.3.1), s and l were 4.0 mm and 8.0 mm respectively.

The angles which particle trajectories made w.r.t. the focal plane were determined by means of ion-optical simulations of trajectories from the target to the focal plane using computer program TRACK [Geo91]. A central-momentum trajectory corresponding to a 42 MeV deuteron was chosen. The deuterons with extreme momenta which are expected to impinge on

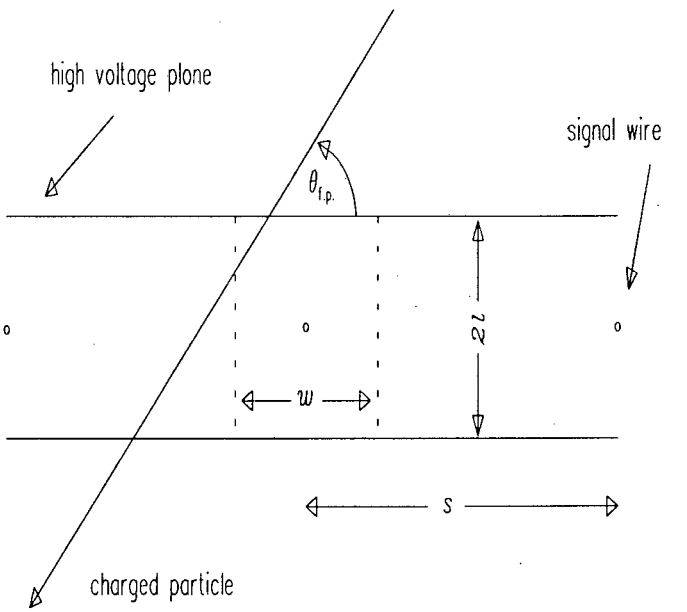

Figure B.1: *Schematic top-view of a charged particle's trajectory intersecting the VDC which has its wire plane positioned along the k = 600 spectrometer focal plane. The notation is described in the text.*

the VDC when the field settings are such that the central trajectory makes an angle of 35.75° w.r.t. the focal plane, were also ray-traced through the spectrometer. These extreme momenta were determined using the relations

$$\delta^+ = \frac{P_{max} - P_{central}}{P_{central}} \tag{B.1}$$

and

$$\delta^- = \frac{P_{min} - P_{central}}{P_{central}}. \tag{B.2}$$

where P denotes momentum and max and min denote the maximum- and minimum-momentum trajectories through the spectrometer. δ^+ and δ^- were empirically determined from TRACK calculations to be 3.8% and 5.0% respectively for the NAC spectrometer. Allowance was made for an angular divergence of ±9.5 mrad at the target thereby taking into account the geometry of the collimator used and its distance from the target (see section 2.3.3). For each extreme momentum two additional trajectories were thus simulated. The simulated trajectories from the target to the focal plane are shown in figure B.2. The angle, $\theta_{f.p.}$, which each of these trajectories

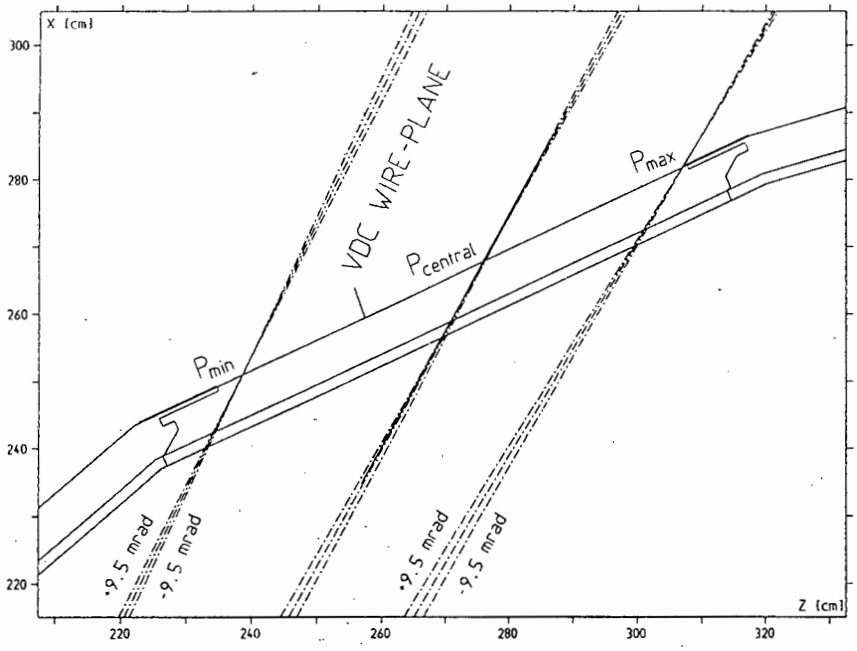

Figure B.2: *Simulated trajectories through the NAC k = 600 spectrometer shown in the vicinity of the focal plane. The simulations were made using the computer program TRACK [Geo91].*

made w.r.t. the VDC were then determined from TRACK. The minimum and maximum values of $\theta_{\text{f.p.}}$ were found to be 32.8° and 40.1° respectively. If the axis parallel to the VDC is denoted as the x-axis, the projection, x_p, of a given trajectory onto the VDC is given by:

$$x_{\text{p}} = \frac{2l}{\tan(\theta_{\text{f.p.}})}. \tag{B.3}$$

For the VDC and collimator geometry used the minimum and maximum values of x_{p} projections are therefore 19.0 mm and 24.9 mm respectively. These extreme projections in conjunction with the VDC signal-wire spacing (s) and the effective signal-wire cell width (w) were then used to determine

the minimum and maximum number of VDC wires expected to register a hit.

The effective signal-wire cell widths were calculated with the drift-chamber computer simulation program GARFIELD [Vee93] which allowed the shape of electric field lines inside the VDC to be predicted. For this study the VDC was operated with negative high voltages of 3.50 kV and 550 V applied to the aluminium HV planes and the guard wires respectively. The lines of equipotential for a VDC having a geometry identical to that used in this study, and operated at voltages as described above, are shown in figure B.3. From this figure the effective signal-wire cell width was estimated to be 2.28 mm.

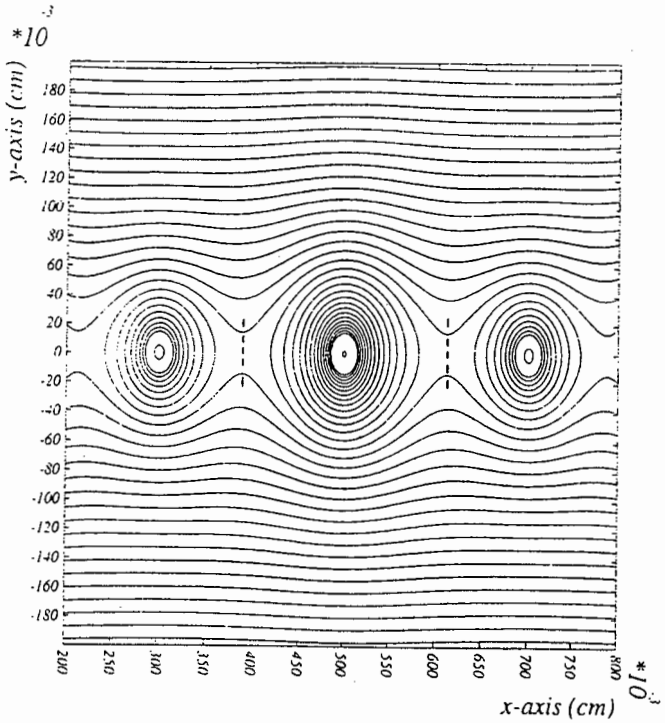

Figure B.3: *Simulated lines of equipotential for a VDC having the same geometry as the one used for this study with negative high voltages of 3.50 kV and 550 V applied to the aluminium HV planes and guard wires respectively. A signal wire is shown flanked by two guard wires. The dashed lines demarcate the effective signal-wire cell width. The simulation was made using the computer program GARFIELD [Vee93].*

x_p	
19.0 mm	24.9 mm
n_{min}	n_{max}
6	7

Table B.1: *Results of the VDC wire hit-analysis.* n_{min} *and* n_{max} *represent the minimum and maximum number of wires, respectively, expected to register hits. The projections of 19.0 mm and 24.9 mm are associated with trajectories which make angles of 40.1° and 32.8° respectively w.r.t. the focal plane as discussed in the text.*

By utilizing the calculated trajectory projections, x_p, and effective signal-wire cell width, it was then possible to determine the minimum and maximum number of signal wires which were expected to register hits. The hit analysis results are given in table B.1. It was found that the expected number of VDC wires registering hits ranged between 5 and 8.

Appendix C

Calculation of Focal-plane Co-ordinates

The procedure used to calculate the focal-plane position and angle co-ordinates for each VDC event using knowledge of which wires registered hits as well as drift times associated with these wires, is discussed below.

A VDC event was considered valid if:

- there was at least one minimum drift time amongst all the drift times associated with the event,
- the number of VDC signal wires which registered hits varied between 3 and 10 (see appendices B and F) and
- not more than one drift time fell outside a valid drift-time range which was specified by setting a software gate (as detailed in section 3.1) on the average drift-time spectrum[1].

Drift times associated with valid events were then scrutinized to ascertain whether drift times were monotonically decreasing and increasing to the left and right of the wire associated with the minimum drift time. A plot of drift time versus wire number for an event satisfying this criterion forms a "V"-like pattern (see figure C.1(a)). The corresponding plot of drift distance versus wire number is shown in figure C.1(b). The absolute

[1] Invalid drift times were not used to calculate the focal plane co-ordinates.

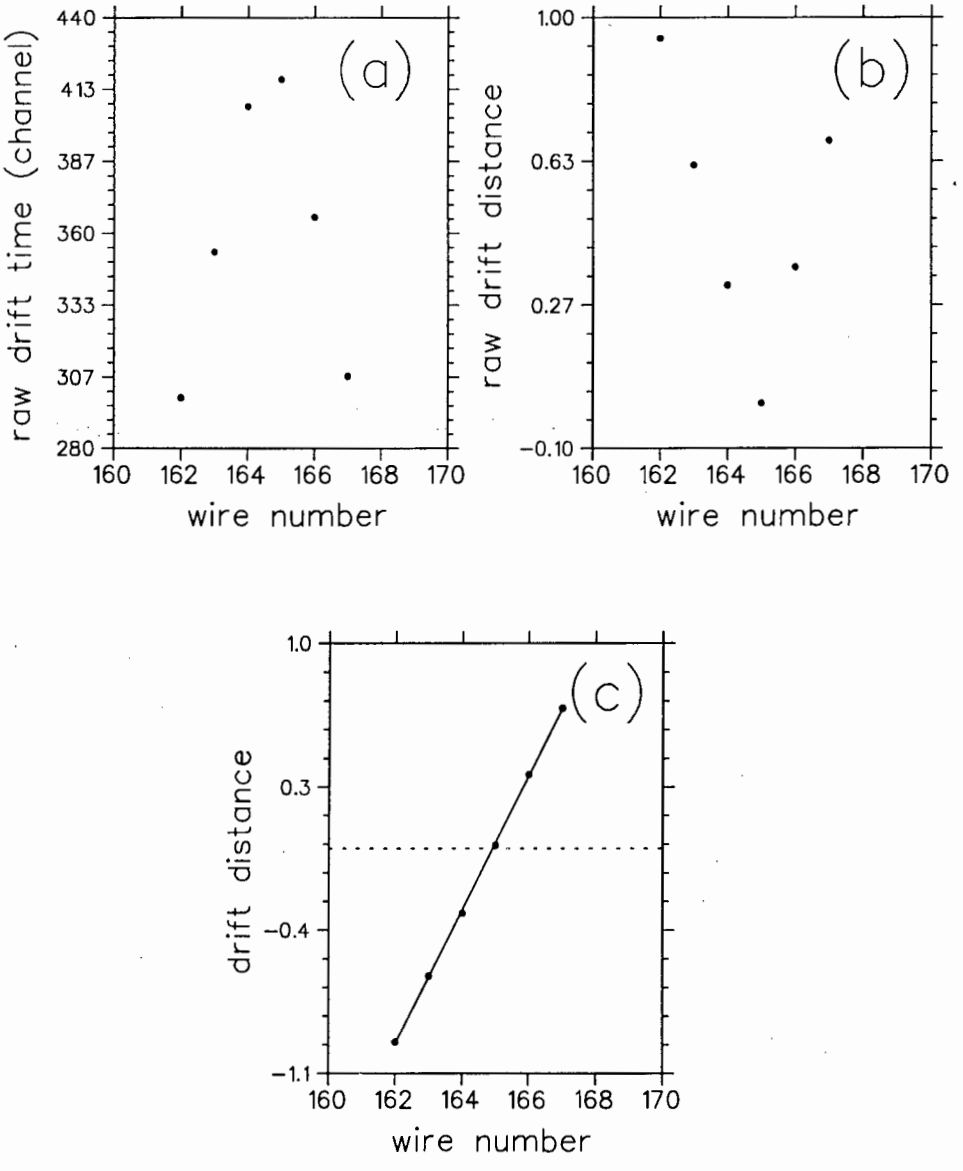

Figure C.1: *(a) Plot of raw drift time versus wire number for a VDC event in which drift times monotonically decrease/increase to left/right of the wire registering the minimum drift time. One drift-time channel is equivalent to* $\sim$ *0.9 ns. (b) Plot of of raw drift distance (in units of signal-wire spacing) versus wire number corresponding to (a) above. (c) Plot of drift distance versus wire number (corresponding to (a) and (b) above) after* $+$ *and* $-$ *signs have been assigned to drift times (see text for details). The resulting linear least-squares fit through these data are shown.*

values of drift times were then converted to drift distances via a lookup table generated using the integral-time-spectrum method [Ber77] as mentioned in section 2.8. After the wire with a minimum drift time was found, + and − signs were assigned to the drift distances based on geometric considerations in conjunction with the assumption that the electron drift velocity was constant. So, for example, the corresponding plot of raw drift distance versus wire number shown in figure C.1(b) is modified to a straight-line pattern as shown in figure C.1(c). Drift distances and corresponding wire numbers forming the points constituting straight-line patterns were then least-squares fitted with a linear function [Bev69]. An example of such a fit is shown in figure C.1(c). The intercept of the fitted line with the zero horizontal axis (dashed curve) yielded the intersection of trajectories with the VDC signal-wire plane and hence the focal-plane position. The trajectory angles relative to the focal plane, $\theta_{\text{f.p.}}$, were calculated from the slopes obtained from the fitting procedure.

During data replay the linear correlation coefficients associated with least-squares fits were studied in order to optimize the resolution. The linear correlation coefficient for a fit to the point associated with the minimum drift time and the points associated with wires on either side of this wire was first calculated. If this linear correlation was found to be worse than for the corresponding coefficient found by fitting all the points other than the point associated with the minimum drift time, the focal-plane co-ordinates were calculated from a fit to all points besides this point.

Appendix D

Spectrometer Transmission

One of the concerns related to the horizontal transmission through the spectrometer was the possibility that, for a collimator having a specific width, particles which are supposed to move through the spectrometer hit instead the spacers (shown in figure 2.2) separating the yokes of the spectrometers's magnets, thereby resulting in a loss of yield at the focal plane. A schematic two-dimensional representation of the trajectory associated with a particle moving from the target through the spectrometer magnets to the focal plane is shown in figure D.1. With respect to the vertical transmission, concern surrounded the possibility that, for a collimator having a specific height, particles which are supposed to move through the spectrometer hit the top or the bottom of the dipole magnets and/or the H-coil, also resulting in a yield loss at the focal plane.

The horizontal and vertical transmission through the spectrometer was studied using a 51.0 mm thick brass collimator which comprised seven slots, each of which could be independently blanked or opened. The location and dimensions of these slots on the collimator are shown schematically in figure D.2. In order to check the horizontal transmission the collimator was positioned inside the collimator carousel with its slots orientated horizontally (i.e. as shown in figure D.2) and the spectrometer tuned for H(p,p) (E_p = 66 MeV, $\theta = 20°$) elastic reaction using a CH_2 target. Relative differential cross sections associated with this reaction were then measured with first the extreme left slot and then the extreme right slot open. The centre of

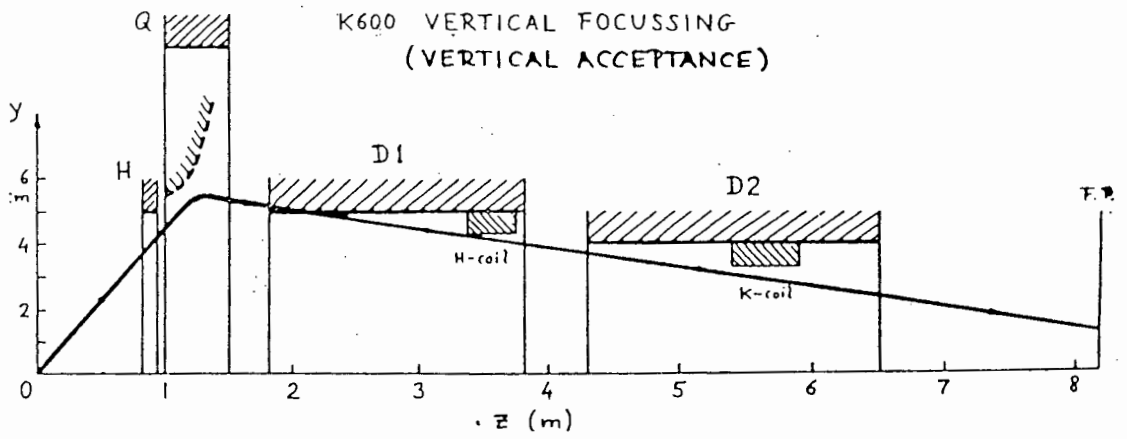

Figure D.1: *Schematic two-dimensional representation of the trajectory associated with a particle moving from the target to the $k = 600$ spectrometer focal plane. (Reproduced from Ref. [Sch86].)*

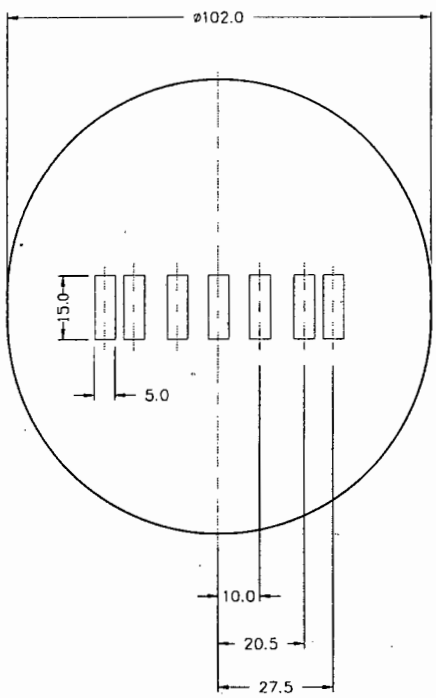

Figure D.2: *Drawing of the 51.0 mm thick variable-slot collimator used to study the spectrometer transmission. All dimensions shown are in mm.*

each of these slots was 27.5 mm from the centre of the collimator. The collimator was then rotated through 90° resulting in the slots being orientated vertically. Measurements of the same cross section were then made with first the extreme top slot and then the extreme bottom slot open in order to check the vertical transmission (all other experimental parameters remained unchanged).

collimator orientation	open slot	differential cross section (arb. units)
horizontal	extreme right	327.6 ± 3.2
	extreme left	323.8 ± 3.4
vertical	extreme top	328.3 ± 3.3
	extreme bottom	331.0 ± 3.3

Table D.1: *Results for the measurement of the relative differential cross sections associated with the H(p,p) (E_p = 66 MeV,θ = 20°) elastic reaction using extreme slots and different orientations of the variable-slot collimator (see figure D.2). Only type A (statistical) uncertainties associated with yields are quoted.*

The results of these measurements are shown in table D.1. All four relative differential cross sections are consistent to within the quoted statistical uncertainties. Given this, and in particular the fact that the two cross sections measured using extreme left and right slots respectively were consistent, no loss of yield due to particles of interest hitting the spacers or the edges of the magnets was indicated. The horizontal transmission for a collimator having a width of $\leq$ 55.0 mm should therefore be 100%. Furthermore since the two cross sections measured using the extreme top and bottom slots respectively were consistent, no loss of transmission in the vertical direction due to particles of interest hitting the dipole magnets or the H-coil when using a collimator of height $\leq$ 55.0 mm was indicated.

In view of the above analyses and the collimator geometry used (see section 2.3.3) during data acquisition, the spectrometer transmission was assumed to be 100% in the evaluation of the proton pickup and deuteron

elastic differential cross sections as detailed in sections 3.4 and F.1 respectively.

Appendix E

Cross-section Tables

Measured c.m. differential cross sections associated with the ^{55}Mn(d,^{3}He)^{54}Cr (E_d = 45.6 MeV) reaction which were used in the DWBA analyses (detailed in section 3.5) are tabulated below. The uncertainties quoted were obtained by combining in quadrature the uncertainties contributing to random scatter associated with the helion yields and the target thickness (see section 3.4). E^* denotes the excitation energy[1] in the final-state nucleus.

[1]See footnote on p. 63.

$\theta_{c.m.}$	$\frac{d\sigma}{d\Omega}(\theta_{c.m.})$ (μb sr^{-1})			
(degrees)	E* = 0.0 MeV	E* = 0.835 MeV	E* = 1.824 MeV	E* = 2.622 MeV
6.3		439 ± 26	377 ± 23	85.2 ± 7.4
8.4		522 ± 29	450 ± 25	56.7 ± 4.7
10.5	18.0 ± 2.0	591 ± 31	560 ± 30	28.5 ± 2.6
12.6	24.7 ± 2.6	626 ± 33	636 ± 34	11.6 ± 1.6
14.7	9.0 ± 1.4	665 ± 35	686 ± 36	20.9 ± 2.3
16.8	4.63 ± 0.94	506 ± 27	517 ± 28	24.3 ± 2.4
18.9	4.61 ± 0.99	290 ± 16	310 ± 17	23.0 ± 2.4
21.0	1.65 ± 0.50	135.0 ± 8.1	151.6 ± 9.0	14.7 ± 1.7
23.0	1.50 ± 0.67	87.1 ± 6.7	84.3 ± 6.6	
25.1	1.77 ± 0.50	97.8 ± 6.1	101.9 ± 6.3	2.17 ± 0.55
27.2		134.9 ± 9.1	147.6 ± 9.7	5.5 ± 1.2
29.3	1.41 ± 0.45	124.4 ± 7.5	145.9 ± 8.6	5.50 ± 0.92
31.4	1.48 ± 0.43	97.6 ± 6.0	96.9 ± 6.0	

$\theta_{c.m.}$	$\frac{d\sigma}{d\Omega}(\theta_{c.m.})$ (μb sr^{-1})			
(degrees)	E* = 3.076 MeV	E* = 3.159 MeV	E* = 3.220 MeV	E* = 3.429 MeV
6.3	292 ± 19	712 ± 40	58.83 ± 7.5	47.4 ± 5.1
8.4	212 ± 13	610 ± 33	87.5 ± 7.8	41.8 ± 3.8
10.5	104.9 ± 7.0	484 ± 26	106.6 ± 9.0	29.2 ± 2.7
12.6	54.4 ± 4.5	413 ± 23	132.2 ± 9.0	28.7 ± 2.8
14.7	65.8 ± 5.2	471 ± 26	157 ± 10	26.1 ± 2.7
16.8	83.3 ± 5.9	445 ± 24	121 ± 7.9	27.7 ± 2.6
18.9	82.9 ± 6.1	314 ± 18	67.4 ± 6.4	17.6 ± 2.1
21.0	46.6 ± 3.7	157.5 ± 9.5	39.6 ± 3.4	10.2 ± 1.3
23.0	21.2 ± 2.7	99.7 ± 9.6	41.9 ± 5.8	
25.1	11.0 ± 1.5	77.3 ± 5.4	34.2 ± 3.1	4.07 ± 0.77
27.2	14.4 ± 2.5	114.3 ± 8.9	43.4 ± 4.9	
29.3	26.6 ± 2.5	120.3 ± 7.6	41.4 ± 3.4	7.0 ± 1.1
31.4	22.9 ± 2.2	103.9 ± 6.6	27.6 ± 2.7	8.6 ± 1.1

$\theta_{c.m.}$	$\frac{d\sigma}{d\Omega}(\theta_{c.m.})$ (μb sr^{-1})			
(degrees)	E* = 3.656 MeV	E* = 3.788 MeV	E* = 3.926 MeV	E* = 4.042 MeV
6.3	77.7 ± 7.0	269 ± 17	305 ± 19	
8.4	100.2 ± 7.1	336 ± 20	256 ± 15	26.5 ± 3.1
10.5	126.5 ± 7.9	369 ± 20	151.8 ± 9.2	38.9 ± 3.3
12.6	161.2 ± 9.9	429 ± 23	99.1 ± 6.7	53.6 ± 4.3
14.7	172 ± 10	473 ± 26	113.7 ± 7.5	59.4 ± 4.6
16.8	129.2 ± 8.0	418 ± 23	124.7 ± 7.8	53.8 ± 4.1
18.9	75.0 ± 5.4	258 ± 15	116.7 ± 7.6	31.5 ± 3.2
21.0	34.7 ± 2.9	122.7 ± 7.5	58.9 ± 4.2	10.5 ± 1.4
23.0	17.9 ± 2.5	72.2 ± 5.9	26.9 ± 3.1	
25.1	19.9 ± 1.9	82.2 ± 5.3	19.7 ± 1.9	11.9 ± 1.4
27.2	30.8 ± 3.3	106.7 ± 7.6	35.4 ± 3.6	15.7 ± 3.7
29.3	31.4 ± 2.6	109.8 ± 6.8	41.5 ± 3.2	16.4 ± 1.7
31.4	25.4 ± 2.2	75.6 ± 4.9	29.4 ± 2.4	9.4 ± 1.2

$\theta_{c.m.}$	$\frac{d\sigma}{d\Omega}(\theta_{c.m.})$ (μb sr^{-1})			
(degrees)	E* = 4.128 MeV	E* = 4.237 MeV	E* = 4.552 MeV	E* = 4.620 MeV
6.3	43.3 ± 4.5		55.2 ± 7.7	61.9 ± 8.1
8.4			46.6 ± 5.4	46.5 ± 5.4
10.5	47.2 ± 3.7	444 ± 25	51.4 ± 4.3	57.7 ± 4.6
12.6	66.1 ± 5.0	900 ± 47	60.7 ± 4.8	71.9 ± 5.4
14.7	67.0 ± 5.0	935 ± 49	46.1 ± 3.9	33.3 ± 3.1
16.8	48.6 ± 3.8	680 ± 36		33.3 ± 3.3
18.9	15.6 ± 2.2	219 ± 13		
21.0		46.6 ± 3.5	14.8 ± 1.7	5.53 ± 0.95
23.0		122.9 ± 8.6		
25.1	18.2 ± 1.8	234 ± 13	9.3 ± 2.6	13.2 ± 3.0
27.2	18.6 ± 4.2	261 ± 16	14.0 ± 5.2	15.3 ± 5.0
29.3	11.3 ± 1.4	164 ± 9.5	8.6 ± 1.2	18.0 ± 1.8
31.4	6.77 ± 0.97	75.8 ± 4.9	7.5 ± 2.1	8.6 ± 2.3

$\theta_{c.m.}$	$\frac{d\sigma}{d\Omega}(\theta_{c.m.})$ (μb sr^{-1})			
(degrees)	E* = 4.868 MeV	E* = 4.936 MeV	E* = 5.194 MeV	E* = 5.311 MeV
6.3	314 ± 21	299 ± 20	254 ± 17	1180 ± 64
8.4	269 ± 17	338 ± 20	179 ± 13	245 ± 15
10.5	289 ± 17	371 ± 21	202 ± 12	540 ± 29
12.6	247 ± 14	345 ± 21	184 ± 11	957 ± 50
14.7	207 ± 13	220 ± 14	148.1 ± 9.5	1137 ± 59
16.8	97.1 ± 6.8	140.8 ± 9.1	54.4 ± 5.3	742 ± 39
18.9	51.2 ± 5.0	60.6 ± 5.5	34.3 ± 6.1	248 ± 15
21.0	45.6 ± 4.2	42.4 ± 3.8	46.4 ± 3.4	29.6 ± 4.2
23.0			31.1 ± 4.0	125 ± 11
25.1	53.1 ± 4.2		46.4 ± 3.4	282 ± 16
27.2	47.6 ± 5.1	69.6 ± 6.3		311 ± 18
29.3	37.8 ± 3.3	44.0 ± 3.7	25.4 ± 2.4	
31.4	17.2 ± 1.8	15.8 ± 1.7	13.9 ± 1.5	105.2 ± 6.4

$\theta_{c.m.}$	$\frac{d\sigma}{d\Omega}(\theta_{c.m.})$ (μb sr^{-1})			
(degrees)	E* = 5.574 MeV	E* = 5.776 MeV	E* = 5.979 MeV	E* = 6.107 MeV
6.3	96 ± 10	131 ± 12	286 ± 19	
8.4	116.7 ± 7.9	129.0 ± 9.7	178 ± 12	57.8 ± 5.6
10.5	120.5 ± 7.6	163 ± 10	226 ± 14	78.8 ± 5.9
12.6	147.6 ± 9.2	108.2 ± 7.2	249 ± 15	
14.7	68.6 ± 5.1	133.6 ± 8.5	241 ± 16	61.8 ± 5.1
16.8	53.5 ± 4.3	68.7 ± 4.9	146 ± 10	43.2 ± 3.5
18.9	31.1 ± 4.7		78.4 ± 6.9	
21.0	18.3 ± 2.8	31.1 ± 3.8		
23.0	30.3 ± 3.4	41.0 ± 8.3	54.0 ± 9.4	
25.1	27.9 ± 2.4	39.6 ± 3.0	62.5 ± 4.8	16.0 ± 1.7
27.2	26.9 ± 3.0	41.6 ± 4.0	75.4 ± 7.2	17.8 ± 3.1
29.3	20.7 ± 3.3	25.1 ± 2.3	43.4 ± 4.4	13.3 ± 1.5
31.4	11.8 ± 1.4	11.6 ± 1.3	24.1 ± 2.1	

Appendix F

Analysis of (d,d)-Mode Data

The generation of the ^{55}Mn(d,d)^{55}Mn(g.s.) angular distribution (E_d = 45.6 MeV, $6° \leq \theta \leq 48°$) and the subsequent extraction of optimized values of optical model parameters for the entrance channel of the ^{55}Mn(d,^{3}He)^{54}Cr reaction in the DWBA calculations (see section 3.5), is discussed below.

F.1 Generation of angular distribution

Focal-plane position spectra associated with deuteron events were generated from off-line analyses of event-by-event data acquired while operating the spectrometer in (d,d)-mode (see section 2.5). In the discussion below only those software gates specific to the analysis of (d,d)-mode data will be discussed[1].

Deuteron events were selected by setting a software gate on the deuteron peak appearing in the spectrometer time-of-flight (TOF) spectrum. A typical gate setting on this spectrum is shown in figure F.1. VDC data (the numbers of wires registering hits and associated drift times) associated with each event which fell in the TOF gate were then checked to ascertain whether, amongst others, drift times fell within an acceptable range and whether these data constituted a satisfactory hit pattern (see appendices B and C). The drift times and wire numbers for valid VDC events were then used to calculate the position where the deuteron trajectories intersected the

[1]The reader is referred to section 3.1 for a more general discussion on software gates.

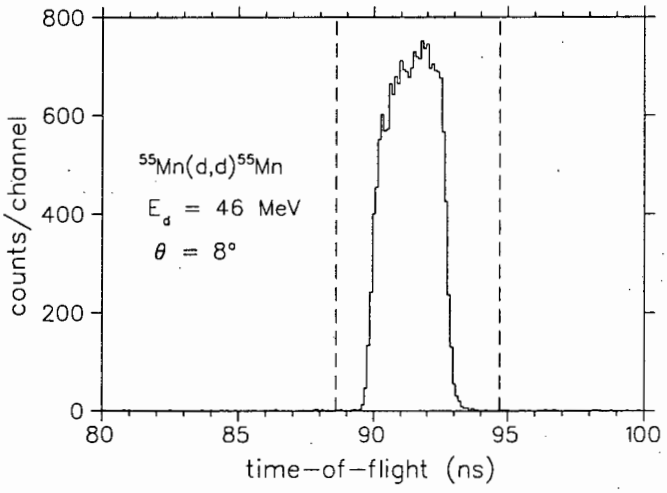

Figure F.1: *Typical time-of-flight spectrum associated with rigidity-selected reaction products that reach the k = 600 focal-plane detector array with the spectrometer operated in (d,d)-mode. The timing start-signal was derived from the paddle plastic scintillation detectors while the stop-signal was generated from the cyclotron RF signal. The peak shown is associated with deuterons as discussed in chapter 2. A typical software gate set on this peak during data reduction, is shown.*

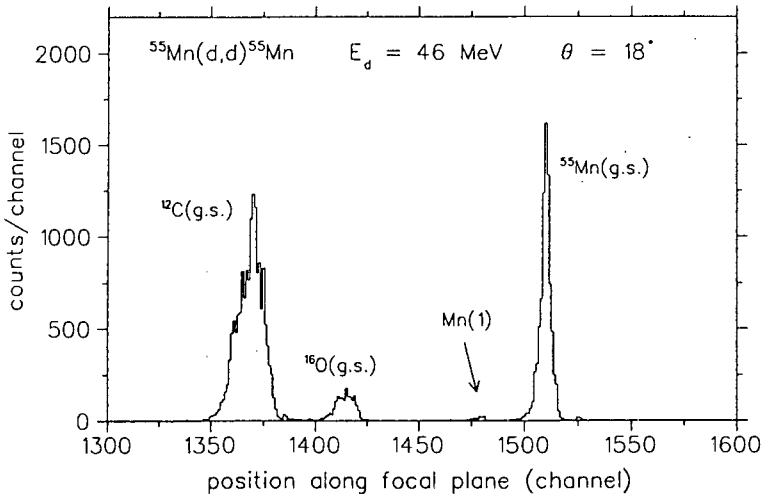

Figure F.2: *Typical focal-plane position spectrum generated from (d,d)-mode data. The $^{16}O(g.s.)$ and $^{12}C(g.s.)$ peaks are due to the elastic scattering of deuterons on the oxygen and carbon nuclei present in the 1.5 μm thick Mylar target backing used. The data shown were acquired at a spectrometer angle of 18°.*

focal plane as described in appendix C. A typical example of a focal-plane position spectrum generated is shown in figure F.2.

Because of the target-backing[2] used, peaks associated with the $^{16}O(d,d)^{16}O$ and $^{12}C(d,d)^{12}C$ reactions were also seen in the focal-plane position spectrum as shown in figure F.2. Due to kinematics the separation between these peaks and the ^{55}Mn(g.s.) peak decreased as θ, the spectrometer angle, was reduced. This caused the ^{55}Mn(g.s.) peak to be partially obscured by the ^{16}O(g.s.) peak for $6° < \theta < 12°$. It was however possible to deconvolute these peaks by setting a gate on a two-dimensional spectrum in which the time-of-flight through the spectrometer was plotted versus focal-plane position[3]. Since the spectrometer K- and H-coil field settings were optimized for detecting deuterons associated with the (d,d) reaction on ^{55}Mn and not on ^{16}O and ^{12}C, the loci for events arising from $^{55}Mn(d,d)^{55}Mn$ reactions appearing in this spectrum were straight while the loci associated

[2] i.e. Mylar.

[3] This is the same spectrum used to optimize the K- and H-coil fields in order to obtain optimum spectrometer resolution (see section 2.9).

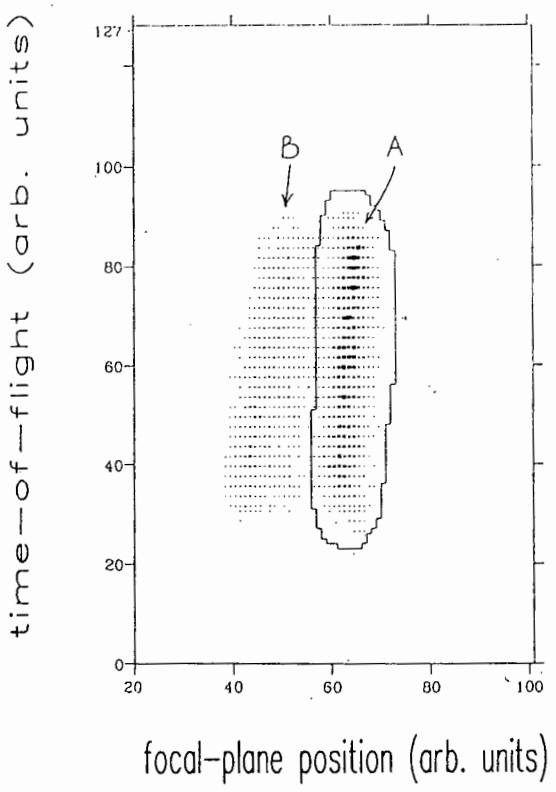

Figure F.3: *Typical software gate setting on a density plot of time-of-flight versus focal-plane position which was used to deconvolute the* $^{55}Mn(d,d)^{55}Mn(g.s.)$ *peak (locus* **A***) from the* $^{16}O(d,d)^{16}O(g.s.)$ *and* $^{12}C(d,d)^{12}C(g.s.)$ *peaks (locus* **B***) in the small-angle mode. The data shown were acquired at a spectrometer angle of 8°.*

with the scattering off ^{16}O and ^{12}C were slanted (see also figure 2.19). A gate could therefore be set around the ^{55}Mn(g.s.) locus, as shown in figure F.3, in order to select the events of interest. Only events falling inside this gate were then used to generate a second focal-plane position spectrum from which yields associated with the ^{55}Mn(d,d)^{55}Mn(g.s.) reaction could be determined. Typical focal-plane position spectra in the vicinity of the ^{55}Mn(d,d)^{55}Mn(g.s.) peak before and after the introduction of this gate are shown in figure F.4.

The absolute centre-of-mass (c.m.) differential cross section associated with the ^{55}Mn(d,d)^{55}Mn(g.s.) reaction, at a c.m. angle $\theta_{\text{c.m.}}$, was calculated

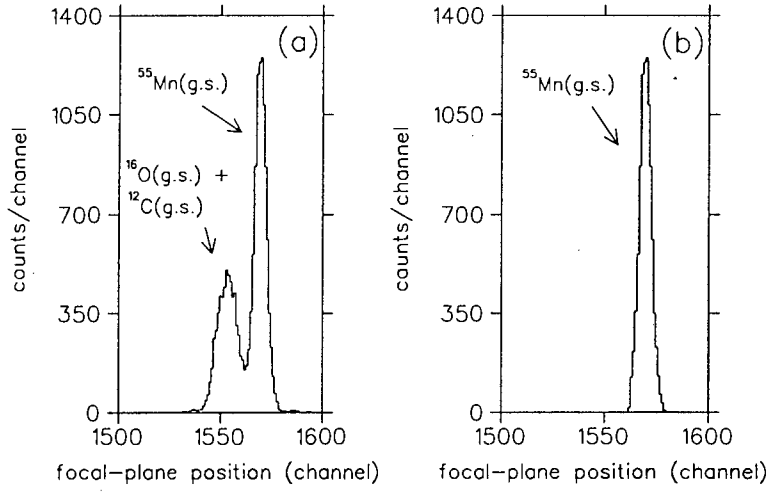

Figure F.4: *Focal-plane position spectra before (a) and after (b) the introduction of a software gate on the spectrum shown in figure F.3 for the spectrometer operated in the (d,d) small-angle mode.*

using the formula

$$\frac{d\sigma}{d\Omega}(\theta_{\text{c.m.}}) = \frac{J\,Y\,cos\frac{\theta}{2}}{N_d\,\Delta\Omega\,n_t\,T_{k600}\,L\,\epsilon_P\,\epsilon_V} \qquad \text{(F.1)}$$

which has an identical form to equation 3.4. Therefore only those factors specific to the (*d*,*d*)-mode appearing in equation F.1 will be discussed below. L, the effective livetime of the data acquisition system while acquiring (*d*,*d*)-mode data was $\geq$ 90% (typically 96%). The yield associated with the transition to the ^{55}Mn ground-state, Y, was determined from the focal-plane position spectrum. Since counts in the ^{55}Mn(g.s.) peak could always be well separated from the counts in the ^{55}Mn(1),^{16}O(g.s.) and ^{12}C(g.s.) peaks, and in view of negligible background in the spectra (as shown in figure F.2 for example), yields were determined by summing the counts in the ^{55}Mn(g.s.) peak like that done with resolved helion peaks (section 3.4.2). It was assumed that the usual Poisson counting statistics applied so that the uncertainty in Y was simply $\sqrt{Y}$. Consistency checks have shown that the contribution to the uncertainties in yields stemming from the setting of software gates were less than 1%.

The efficiency of the paddles at detecting the deuterons of interest, ϵ_P,

can be written as the product

$$\epsilon_P = \epsilon_{P_g} \epsilon_{P_i} \tag{F.2}$$

where ϵ_{P_g} and ϵ_{P_i} are the paddle geometric and intrinsic efficiencies [Kno89] respectively for detecting the deuterons of interest. In the (*d*,*d*)-mode, the spectrometer magnetic fields were set so that the deuterons associated with the transition to the ^{55}Mn(g.s.) were always located near the centre of the focal plane. The deuterons of interest therefore always traversed the VDC close to its centre. The paddles located behind the VDC could therefore always be reached by these deuterons (i.e. there was no obstruction or absence of scintillator material) and ϵ_{P_g} was therefore assumed to be 100%. This assumption was checked at $\theta = 18°$ by sweeping the ^{55}Mn(g.s.) peak across the focal plane by adjusting the central-trajectory energy tune. A plot of relative differential cross section associated with the ^{55}Mn(*d*,*d*)^{55}Mn(g.s.) (E_d = 46 MeV, $\theta = 18°$) reaction as a function of the central-trajectory energy tune is shown in figure F.5, displaying the consistency of, *inter alia*, ϵ_{P_g} across the focal plane. It is rare for primary charged particles not to produce some sort of ionization or excitation interaction in the active detecting material [Kno89]. In view of this, the fact that the deuterons deposited relatively large energies[4] and the fact that the thresholds on the constant fraction discriminators used to process the paddle signals (section 2.7.1) were set to a minimum, ϵ_{P_i} was assumed to be 100% as well.

The VDC's efficiency, ϵ_V, is an indication of its efficiency (relative to that of the plastic paddles) at detecting charged particles that pass through the spectrometer onto the focal plane where they intersect the VDC and the paddles. As in the case of the paddles, the VDC efficiency can be written as the product of a geometric and intrinsic efficiency:

$$\epsilon_V = \epsilon_{V_g} \epsilon_{V_i} \tag{F.3}$$

Since the ^{55}Mn(g.s.) peak was always located at the centre of the focal plane, there were no factors which could cause a geometric inefficiency in horizontal direction (parallel to the length of the VDC). In tests with a

[4]See section 2.5.

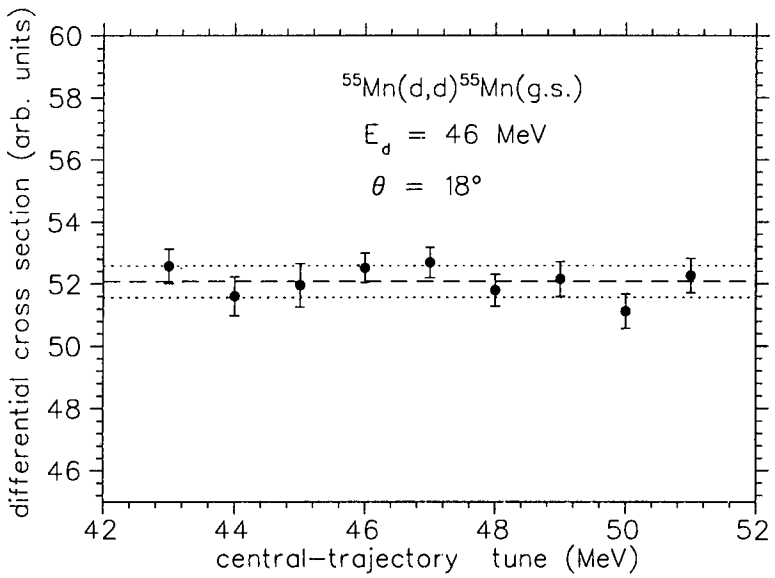

Figure F.5: *Relative differential cross section for the $^{55}Mn(d,d)^{55}Mn(g.s.)$ (E_d = 46 MeV, θ = 18°) reaction plotted as a function of spectrometer central-trajectory energy tune. The $^{55}Mn(g.s.)$ peak was moved by changing only the magnetic field of dipole 2. The dashed line represents the mean value while the dotted lines are located ± 1σ from the mean.*

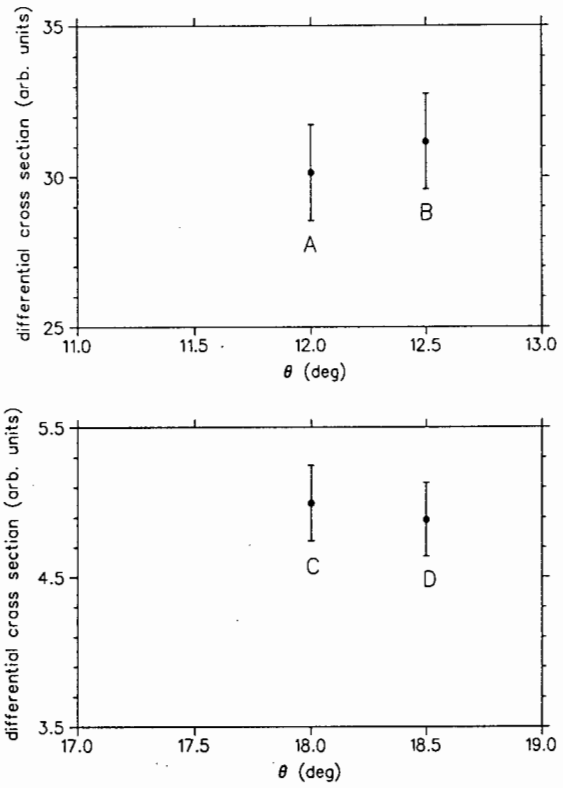

Figure F.6: *Measured overlap differential cross sections for* $^{55}Mn(d,d)^{55}Mn(g.s.)$ *(E_d = 46 MeV, θ = 12°,18°) reaction plotted versus spectrometer angle. One point at each angle is offset by 0.5° for purposes of clarity. The uncertainties shown were obtained by combining in quadrature the statistical uncertainties associated deuteron yields and the uncertainty (1σ) associated with the target thickness. (a) Point* **A** *was measured using a graphite beam-stop located in the scattering chamber while point* **B** *was measured using a graphite beam-stop located in the steel chamber used to house the collimator in the spectrometer small-angle mode (see figures 2.8 and 2.9) (b) Point* **C** *was measured using the normal external beam-stop while point* **D** *was measured using a graphite beam-stop located inside the scattering chamber.*

horizontal drift chamber (located behind the VDC) which measured position in the vertical direction it was observed that the rigidity-selected particles were well-focussed[5] in the vertical direction. In view of the above and the consistency shown in figure F.5, the VDC geometric efficiency, ϵ_{V_g}, was taken to be 100%.

The VDC intrinsic detection efficiency, ϵ_{V_i}, was defined as follows:

$$\epsilon_{V_i} = \frac{N_{\text{f.p.}}}{N_{\text{g}}} \tag{F.4}$$

where $N_{\text{f.p.}}$ is the total number of counts recorded in the focal-plane position spectrum after setting two gates. The first of these were set on the spectrometer time-of-flight spectrum while the second was set on the two-dimensional spectrum in which the summed pulse height for paddle 1 was plotted versus the summed pulse height for paddle 2. The former was set to encompass only a thin central slice of the full time-of-flight peak, while the latter was set to encompass only a central portion of the locus relating to elastic events in order to minimize the possibility of including background events in the determination of ϵ_{V_i}. N_g in equation F.4 represents the number of counts located inside the two-dimensional gate associated with a particular gate set on the TOF spectrum. In view of the criteria characterizing valid VDC events (detailed in appendix C), $N_{f.p.}$ and N_g are related via:

$$N_{\text{g}} = N_{\text{f.p.}} + N_{\geq max} + N_{\leq min} + N_{\geq 1 n_i} \tag{F.5}$$

where:

- max (min) is the maximum (minimum) number of VDC wires expected to register hits,
- n_i is the number of invalid drift times associated with a particular event,
- $N_{\geq max}$ ($N_{\leq min}$) is the number of events for which $\geq max$ ($\leq min$) wires registered hits,
- $N_{\geq 1 n_i}$ is the number of events in which $\geq n_i$ ($= 1$, for this study) drift time is outside a valid drift-time range.

[5] See section 3.4.9.

quantity	symbol	% uncertainty
yield	Y	≤ 4 (type A)
		≤ 1 (type B)
solid angle	$\Delta\Omega$	< 1
incident deuteron flux	N_d	< 1
target nuclear density	n_t	5
Jacobian	J	~ 0.01

Table F.1: *Breakdown of uncertainties associated with quantities appearing in equation F.1, which was used to calculate c.m. differential cross sections for the $^{55}Mn(d,d)^{55}Mn(g.s.)$ (E_d = 45.6 MeV) reaction.*

According to the VDC wire hit-analysis (appendix B) $max = 8$ and $min = 5$. However checks with various values of max and min have shown that ϵ_{V_i} is optimum if $max = 10$ and $min = 3$. These values were therefore used during the final data replay. Each data set used to generate the deuteron elastic angular distribution was analysed in the manner described above in order to obtain a value of ϵ_{V_i} required for calculating the differential cross section at that angle. An average VDC intrinsic efficiency of 99% was obtained.

As mentioned in section 2.3.2, three methods were used to measure the integrated current for $6° \leq \theta \leq 48°$. In order to assess the relative accuracy of these charge collection techniques, overlap differential cross sections were measured at laboratory angles of 12° and 18°. The first differential cross section at 12° was measured using a graphite beam-stop located inside the scattering chamber (see figure 2.8), while the second was measured using a beam-stop located inside the special chamber designed to house the collimator in the spectrometer small-angle mode (see figure 2.9). These cross sections which are plotted in figure F.6(a) (offset by 0.5° for purposes of clarity) were found to be consistent. The first cross section at 18° was measured using the external beam-stop while the second was measured using a graphite internal beam-stop. These cross sections were also found to be consistent (see figure F.6(b) where the two points were also offset by 0.5°). There was therefore no need to introduce any corrections due to the charge-

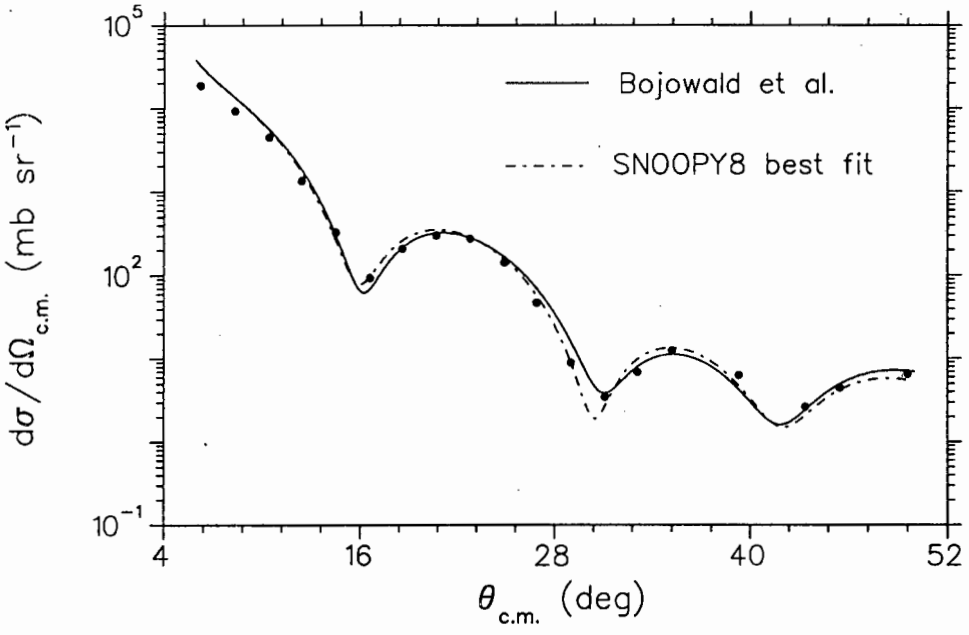

Figure F.7: *Measured c.m. angular distribution for the $^{55}Mn(d,d)^{55}Mn(g.s.)$ reaction at an average incident energy of 45.6 MeV. The uncertainty (see text) in differential cross section is smaller than the size of the plotting symbol. The solid curve is a prediction based on the global parameterization by Bojowald* et al. *[Boj88], while the broken line results from a calculation based on a potential having the same form as that of Bojowald* et al., *but with parameters optimized using the code SNOOPY8 [Sch82].*

collection technique.

The uncertainties associated with the (d,d) cross sections due to counting statistics were $\leq 4\%$ while the combined uncertainty (1σ) associated with the target thickness, current integration and solid angle was estimated to be $\sim 5\%$ (see table F.1 for a breakdown). The experimentally measured ^{55}Mn$(d,d)^{55}$Mn(g.s.) c.m. angular distribution is plotted in figure F.7, while the respective values of the differential cross sections and c.m. angles are tabulated in table F.2. In view of the fact that the measured angular distribution was least-squares fitted in order to extract optical-model parameters and since data were acquired on two targets, the uncertainties (1σ) associated with the yield and target thickness (combined in quadrature) were utilized in calculating the weights used in the fitting procedure (see equation F.6). Only these uncertainties are shown in figure F.7 and tabulated in table F.2.

The solid curve shown in figure F.7 is a calculated[6] angular distribution obtained using the global parameterization of deuteron optical potentials obtained by Bojowald *et al.* as given in table F.3. They used a potential comprising Coulomb, real volume, imaginary volume, imaginary surface and real spin orbit terms. The form of the potential is given by equation 3.14. In figure F.7 it is seen that the Bojowald *et al.* parameterization generally gives a good fit to the measured data. In order to check the absolute normalization, a portion of the measured angular distribution, consisting of the measured differential cross sections at c.m. angles of 22.8°, 24.9° and 26.9°, were normalized to the corresponding calculated points using a χ^2 minimization procedure. A normalization factor of 1.06 was obtained. Therefore, in view of the magnitude of the total experimental uncertainty associated with the measured differential cross sections, no normalization factor was introduced.

A closer inspection of figure F.7 shows that the theoretical angular distribution is consistently higher than the measured data for $\theta_{\text{c.m.}} \leq 14°$. In view of this these data were re-analysed. Analysing only a subset of the data at each angle resulted in the same deviation, thereby ruling out the

[6]The DWBA computer code DWUCK4 [Kun93] was used.

$\theta_{\text{c.m.}}$ (degrees)	$\frac{d\sigma}{d\Omega}(\theta_{\text{c.m.}})$ (mb sr^{-1})
6.2	18864 ± 987
8.3	9320 ± 478
10.4	4479 ± 226
12.4	1335.3 ± 68.2
14.5	330.1 ± 17.3
16.6	93.05 ± 4.77
18.6	208.5 ± 10.5
20.7	300.9 ± 15.1
22.8	275.0 ± 14.4
24.9	142.34 ± 7.15
26.9	47.26 ± 2.51
29.0	8.874± 0.473
31.1	3.457 ± 0.210
33.1	6.834 ± 0.414
35.2	12.423 ± 0.667
39.3	6.296 ± 0.355
43.4	2.630 ± 0.140
45.5	4.461 ± 0.245
49.6	6.508 ± 0.337

Table F.2: *Measured c.m. differential cross sections associated with the $^{55}Mn(d,d)^{55}Mn(g.s.)$ reaction at an average incident energy of 45.6 MeV. The uncertainties quoted were obtained by combining in quadrature the statistical uncertainties associated with the deuteron yields and the uncertainty (1σ) associated with the target thickness.*

possibility of a time-dependent effect. The raw count rates for these data were extracted by dividing the total number of events in the time-of-flight spectrum by the run time, yielding a highest count rate of 100 counts s^{-1}. A deadtime problem was therefore also excluded. Since the target used in obtaining these data was the same as the one used to obtain some of the data for $\theta_{c.m.} > 14°$, the possibility of the discrepancy being attributable to an erroneous target thickness was also ruled out. Finally, since the measured overlap differential cross sections discussed above were consistent, there was no reason to doubt the charge-collection technique in the small-angle mode. Therefore no correction factors were introduced.

F.2 Analysis of angular distribution

In order to optimize the optical-model potential parameters for the entrance channel of the ^{55}Mn(d,^{3}He)^{54}Cr reaction, the deuteron elastic scattering angular distribution (table F.2), was analysed with the aid of a χ^2 minimization procedure using the nonrelativistic optical-model code SNOOPY8 (version 6/01/82) [Sch82]. The code searches for the best-fit optical potential parameters using a combination of the Oak Ridge/Oxford and Saclay χ^2 minimization methods.

Optimized potential parameters were obtained by minimizing a quantity, χ^2, defined as

$$\chi^2 = \sum_{\theta_{c.m.}} \left(\frac{\sigma_{expt}(\theta_{c.m.}) - \sigma_{calc}(\theta_{c.m.})}{\Delta\sigma_{expt}(\theta_{c.m.})} \right)^2 \qquad \text{(F.6)}$$

where $\sigma_{expt}(\theta_{c.m.})$ is the measured c.m. differential cross section associated with the ^{55}Mn(d,d)^{55}Mn(g.s.) (E_d = 45.6 MeV) reaction at c.m. angle $\theta_{c.m.}$, $\Delta\sigma_{expt}(\theta_{c.m.})$ is the uncertainty associated with this cross section and $\sigma_{calc}(\theta_{c.m.})$ is the corresponding differential cross section calculated with the SNOOPY8 code. The latter cross section was calculated using an optical potential having the same form as that used by Bojowald *et al.* (equation 3.14), while the initial values of the associated potential parameters were identical to those tabulated in column 3 of table F.3.

A maximum of three parameters were allowed to vary in each SNOOPY8 "SEARCH" routine in order to avoid parameter correlations become signifi-

potential parameter	Bojowald *et al.* parameterization	specialization to this work	SNOOPY 8 best fit
V	$81.32 + 1.43ZA^{-\frac{1}{3}} - 0.24E_d$	79.80	82.14
r_v	1.18	1.18	1.18
a_v	$0.636 + 0.035A^{\frac{1}{3}}$	0.769	0.786
W_{vol}	0 ($E_d \leq 45.0$)		
	$0.132(E_d - 45.0)$ ($E_d \geq 45.0$)	0.079	0.079
W_{surf}	$7.80 + 1.04A^{\frac{1}{3}} - 0.712W_{vol}$	11.70	13.25
r_w	1.27	1.27	1.27
a_w	0.850	0.850	0.837
$V_{l.s}$	6.00	6.00	4.73
$r_{l.s}$	0.925	0.925	0.922
$a_{l.s}$	0.925	0.925	0.605
r_c	1.30	1.30	1.30

Table F.3: *Parameterization of a global optical-model potential for deuterons having a form as given by equation 3.14 taken from the study of Bojowald* et al. *[Boj88]. A and Z denote the target-nucleus mass and charge respectively. The parameter values tabulated in column 3 were calculated with this parameterization, for the $^{55}Mn(d,d)^{55}Mn(g.s.)$ (E_d = 45.6 MeV) reaction, and were used as starting values in the search for best-fit parameters (column 4) performed with the code SNOOPY8 [Sch82] (see text for details). All potential depths are in MeV, and all geometrical parameters are in fm.*

cant when four to six parameters are allowed to vary simultaneously [Sch82]. The minimization procedure, which is similar to the one adopted by Barnard *et al.* [Bar68], entailed first varying the well-depths V, $V_{l.s}$ and W_{surf} to find a first minimum χ^2, χ^2_{min}. These well-depths were fixed at the best-fit values after which the radius parameters r_r, $r_{l.s}$ and r_w were allowed to vary[7] to find a new χ^2_{min}. With the potential depth and radius parameters fixed at the best-fit values, the diffuseness parameters a_v, a_w and $a_{l.s}$ were then allowed to vary to find a final χ^2_{min} . The best-fit parameters[8] obtained from the minimization procedure are tabulated in table F.3 (column 4) while the angular distribution generated using these parameters is shown superimposed on the measured angular distribution in figure F.7.

[7]The imaginary volume well depth W_{vol} and the Coulomb radius r_c were not varied.

[8]The dependence of the best-fit parameters on the sequence in which parameters were varied was also investigated. A maximum variation of 0.2% was found in any best-fit parameter obtained using a different sequence.

Appendix G

Treatment of Uncertainties

The treatment of uncertainties suggested in Refs. [Mül79, Mül84] was adopted in this study. The main feature of the adopted approach is the distinction between

- type A uncertainties which can be evaluated via statistical means and
- type B uncertainties which have to be evaluated via other means.

In order to make estimates of standard deviations associated with type B uncertainties a trapezoidal probability distribution was used. For this distribution [ISO92]:

$$\sigma = a\sqrt{\frac{1+\beta^2}{6}} = af \tag{G.1}$$

where

- a is the half-width of the distribution,
- $0 \leq \beta \leq 1$ ($\beta = 1$ gives a rectangular distribution and $\beta = 0$ gives a triangular distribution) and
- σ is the estimated standard deviation.

For this study β was assumed to be 0.50 so that $f = 0.46$.

References

[Aus60] N. Austern, in *Proceedings of the International Conference on Nuclear Structure, Kingston, Canada, 1960*, D. A. Bromley and E. W. Vogt (eds.), (North-Holland, Amsterdam, 1960), pp. 323–335.

[Aus64] N. Austern, R. M. Drisko, E. C. Halbert, and G. R. Satchler, Phys. Rev. **113**, B3 (1964).

[Bac90] A. Bacher, G. P. Berg, D. Bilodeau, C. Foster, J. Lisantti, T. Rinckel, P. Schwandt, E. J. Stephenson, Y. Wang, and S. Wells, Scientific and Technical Report, May 1989 - April 1990, (Indiana University Cyclotron Facility , Bloomington, 1990), pp. 178–179.

[Bar68] R. W. Barnard and G. D. Jones, Nucl. Phys. **A106**, 497 (1968).

[Bar77] S. M. Barr and R. M. DelVecchio, Phys. Rev. C **15**, 114 (1977).

[Ber77] W. Bertozzi, M. V. Hynes, C. P. Sargent, C. Creswell, P. C. Dunn, A. Hirsch, M. Leitch, B. Norum, F. N. Rad, and T. Sasanuma, Nucl. Instrum. Methods **141**, 457 (1977).

[Ber79] W. Bertozzi, M. V. Hynes, C. P. Sargent, W. Turchinetz, and C. Williamson, Nucl. Instrum. Methods **162**, 211 (1979).

[Ber86] G. P. A. Berg, L. C. Bland, B. M. Cox, D. DuPlantis, D. W. Miller, K. Murphy, P. Schwandt, K. A. Solberg, E. J. Stephenson, B. Flanders, and H. Seifert, Scientific and

Technical Report, (Indiana University Cyclotron Facility, Bloomington, 1986), pp. 152–162.

[Ber88] G. P. A. Berg, L. C. Bland, D. DuPlantis, C. C. Foster, D. W. Miller, P. Schwandt, R. Sawafta, K. Solberg, and E. Stephenson, Scientific and Technical Report, January 1987 - April 1988, (Indiana University Cyclotron Facility, Bloomington, 1988), pp. 233–237.

[Ber89] G. P. A. Berg, L. Bland, C. C. Foster, J. Lisantti, T. Rinckel, R. Sawafta, P. Schwandt, K. Solberg, and E. J. Stephenson, Scientific and Technical Report, May 1988 - April 1989, (Indiana University Cyclotron Facility, Bloomington, 1989), pp. 200–204.

[Bev69] P. R. Bevington, *Data Reduction and Error Analysis for the Physical Sciences*, (McGraw-Hill, New York, 1969), p. 105.

[Boj88] J. Bojowald, H. Machner, H. Nann, W. Oelert, M. Rogge, and P. Turek, Phys. Rev. C **38**, 1153 (1988).

[Bot84] A. H. Botha and H. N. Jungwirth, in *Proceedings of the Tenth International Conference on Cyclotrons and their Applications, Michigan, 1984*, F. Marti (ed.) (IEEE, New York, 1984), p. 263.

[Bot95] A. H. Botha, private communication, National Accelerator Centre, (1995).

[Bre74] A. Breskin, G. Charpak, B. Gabioud, F. Sauli, N. Trautner, W. Duinker, and G. Schultz, Nucl. Instrum. Methods **119**, 9 (1974).

[Bru77] P. J. Brussaard and P. W. M. Glaudemans, *Shell-Model Applications in Nuclear Spectroscopy*, (North-Holland, Amsterdam, 1977), pp. 144–175.

[Bur95] W. E. Burcham and M. Jobes, *Nuclear and Particle Physics*, (Longman, Essex, 1995), pp. 184–204.

[Cam81] J. A. Cameron, E. Habib, A. A. Pilt, R. Schubank, and V. Janzen, Nucl. Phys. **A365**, 113 (1981).

[Cha77] N. S. Chant, N. S. Hall, C. F. Clement, S. M. Perez, and J. N. Craig, Phys. Rev. C **15**, 53 (1977).

[Cha84] G. Charpak and F. Sauli, Ann. Rev. Nucl. Part. Sci. **34**, 285 (1984).

[Cha93] C. H. C. Challens, M.Sc. thesis, University of the Western Cape, unpublished (1993).

[Chu78] W. K. Chu, J. W. Mayer, and M. A. Nicolet, *Backscattering Spectrometry*, (Academic Press, New York, 1978).

[Cle73] C. F. Clement and S. M. Perez, Nucl. Phys. **A213**, 510 (1973).

[Cle77] C. F. Clement and S. M. Perez, Nucl. Phys. **A284**, 469 (1977).

[Cle91] C. F. Clement and S. M. Perez, Rep. Prog. Phys. **54**, 127 (1991).

[Col59] L. Colli, F. Cvelber, S. Micheletti, and M. Pignanelli, Nuovo Cimento **14**, 1120 (1959).

[Col61] L. Colli, I. Iori, S. Micheletti, and M. Pignanelli, Nuovo Cimento **20**, 94 (1961).

[Con94] J. L. Conradie, Ph.D. thesis, University of Stellenbosch, unpublished (1994).

[den88a] J. W. A. den Herder, H. P. Blok, E. Jans, L. Lapikás, and P. K. A. de Witt Huberts, Phys. Lett. **60**, 1343 (1988).

[den88b] J. W. A. den Herder, H. P. Blok, E. Jans, P. H. M. Keizer, L. Lapikás, E. N. M. Quint, G. van der Steenhoven, and P. K. A. de Witt Huberts, Nucl. Phys. **A490**, 507 (1988).

[Doo85] L. R. Doolittle, Nucl. Instrum. Methods **B9**, 344 (1985).

[Eis88] J. M. Eisenberg and W. Greiner, *Excitation Mechanisms of the Nucleus*, (North-Holland, Amsterdam, 1988), pp. 412–422.

[Ful85] H. W. Fulbright, in *Treatise on Heavy-Ion Science: Vol. 7 - Instrumentation and Techniques*, D. A. Bromley (ed.), (Plenum Press, New York, 1985), pp. 179–224.

[Geo91] D. George and V. Vranković, ion-optical computer simulation program *TRACK* (version 4.8), unpublished (1991).

[Gon87] Wang Gongqing, Zhu Jiabi, and Zhang Jingen, Nucl. Data Sheets **50**, 255 (1987).

[Gou81] C. R. Gould, L. G. Holzsweig, S. E. King, Y. C. Lau, R. V. Poore, N. R. Roberson, and S. A. Wender, IEEE Trans. Nucl. Sci. **NS-28**, 3708 (1981).

[Gou83] C. R. Gould and N. R. Robertson, IEEE Trans. Nucl. Sci. **NS-30** 5, 3758 (1983).

[Gra92] P. Grabmayr, Prog. Part. Nucl. Phys. **29**, 251 (1992).

[Gra94] P. Grabmayr, A. Mondry, G. J. Wagner, P. Woldt, G. P. A. Berg, J. Lisantti, D. W. Miller, H. Nann, and E. J. Stephenson, Phys. Rev. C **49**, 2971 (1994).

[Hen74] D. L. Hendrie, in *Nuclear Spectroscopy and Reactions: Part A*, J. Cerny (ed.), (Academic Press, New York, 1974), pp. 365–412.

[Hen87] R. S. Henderson, O. Hausser, K. Hicks, C. Gunther, W. Faszer, R. Sawafta, and N. Poppe, Nucl. Instrum. Methods **A524**, 61 (1987).

[Hey94] K. L. G. Heyde, *The Nuclear Shell Model*, 2nd edition, (Springer-Verlag, Berlin, 1994), pp. 58–148.

[Hin67] P. F. Hinrichsen and B. Rosner, Bull. Amer. Phys. Soc. **12**, 696 (1967).

[Hod74] P. E. Hodgson, Nature Vol. 249, No. 5456, 412 (1974).

[Hol81] L. G. Holzsweig and R. V. Poore, IEEE Trans. Nucl. Sci. **NS-28**, 3815 (1981).

[ISO92] *Guide to the Expression of Uncertainty in Measurement*, document no. **ISO/TAG 4/WG 3**, 1st edition, (International Organization for Standardization, Geneva, 1992), pp. 12–16.

[Jac77] D. F. Jackson and R. C. Barrett, *Nuclear Sizes and Structure*, (Clarendon Press, Oxford, 1977), pp. 332–351.

[Jam75] F. James and M. Roos, Comput. Phys. Commun. **10**, 343 (1975).

[Jam89] F. James and M. Roos, document no. **D506**, (CERN, Geneva, 1989).

[Jin92] Yanhe Jin, D. S. Onley, and L. E. Wright, Phys. Rev. C **45**, 131 (1992).

[Jun87] Huo Junde, Hu Dailing, Zhou Chunmei, Han Xiaoling, Hu Baohua, and Wu Yaodong, Nucl. Data Sheets **51**, 1 (1987).

[Jun92] Huo Junde, Nucl. Data Sheets **67**, 523 (1992).

[Jun93] Huo Junde, Sun Huibin, Zhao Weizhong, and Zhou Qing, Nucl. Data Sheets **68**, 887 (1993).

[Kin81] S. E. King, Y. C. Lau, and C. R. Gould, IEEE Trans. Nucl. Sci. **NS-28** 5, 3822 (1981).

[Kno89] G. F. Knoll, *Radiation Detection and Measurement*, (John Wiley and Sons, New York, 1989), pp. 117–120.

[Kra88] G. J. Kramer, H. P. Blok, J. F. A. van Hienen, S. Brandenburg, M. N. Harakeh, S. Y. van der Werf, P. W. M. Glaudemans, and A. A. Wolters, Nucl. Phys. **A477**, 55 (1988).

[Kra89] G. J. Kramer, H. P. Blok, J. F. J. van den Brand, H. J. Bulten, R. Ent, E. Jans, J. B. J. M. Lanen, L. Lapikás, H. Nann, E. N. M. Quint, G. van der Steenhoven, P. K. A. de Witt Huberts, and G. J. Wagner, Phys. Lett. **B227**, 199 (1989).

[Kun93] P. D. Kunz and E. Rost, in *Computational Nuclear Physics 2 – Nuclear Reactions*, K. Langanke, J. A. Maruhn, and S. E. Koonin (eds.), (Springer-Verlag, New York, 1993), p. 88–107.

[Lu84] Xi-Ting Lu, Nucl. Instrum. Methods **225**, 283 (1984).

[Mah91] C. Mahaux and R. Sartor, Adv. in Nucl. Phys. **20**, 1 (1991).

[Man85] H. J. Mang, in *Proceedings of the Winter College on Fundamental Nuclear Physics, Vol.1, International Centre for Theoretical Physics, Trieste, Italy, 7 Feb - 30 Mar 1984*, K. Dietrich, M. Di Toro, and H. J. Mang (eds.), (World Scientific, Singapore, 1985), pp. 15–55.

[Mar68] J. B. Marion and F. C. Young, *Nuclear Reaction Analysis*, (North-Holland, Amsterdam, 1968).

[Mar70] P. Marmier and E. Sheldon, *Physics of Nuclei and Particles, Vol. II*, (Academic Press, London, 1970), pp. 1087–1169.

[Mar93] T. K. Marais, Ph.D. thesis, University of the Western Cape, unpublished (1993).

[Mat68] M. Matoba, Nucl. Phys. **A118**, 207 (1968).

[Moa77] A. Moalem, Nucl. Phys. **A289**, 45 (1977).

[Moa79] A. Moalem and Z. Vardi, Nucl. Phys. **A332**, 195 (1979).

[Mül79] J. W. Müller, Nucl. Instrum. Methods **163**, 241 (1979).

[Mül84] J. W. Müller, *Precision Measurement and Fundamental Constants II*, B. N. Taylor and W. D. Phillips (eds.), Natl. Bur. Stand. (U.S.A.), Spec. Publ. No. 617 (1984).

[NAC92] NAC annual report **NAC/AR/92-01**, (National Accelerator Centre, Faure, 1992), pp. 27–28.

[NAC94] NAC annual report, **NAC/AR/94-01**, (National Accelerator Centre, Faure, 1994), pp. 28–29.

[Nan89] H. Nann, in *Direct Nuclear Reactions - Proceedings of the International Seminar, 1989*, (Indian Academy of Sciences, Bangalore, 1989), pp. 317–319.

[Neu94] F. Neumeyer and S. Strauch, peak-fitting computer program *FIT2.1*, Technische Hochschule Darmstadt, unpublished (1994).

[New95] R. T. Newman and S. M. Perez, Phys. Rev. C **51**, 1414 (1995).

[New96] R. T. Newman, R. W. Fearick, S. M. Perez, D. G. Aschman, K. Bharuth-Ram, F. D. Smit, V. M. Tshivhase, and T. S. Volkwyn, Phys. Rev. C, (1996) (in press).

[Niw82] M. Niwano, T. Ishimatsu, R. Asano T. Suehiro, and M. Tanaka, Nucl. Phys. **A377**, 148 (1982).

[Off87] E. A. J. M. Offerman, C. W. De Jager, and H. De Vries, Nucl. Instrum. Methods **A262**, 298 (1987).

[Pee74] R. J. Peel, D. R. Dixon, M. W. Hill, G. L. Jensen, N. F. Mangelson, N. Nath, and V. C. Rogers, Nucl. Phys. **A235**, 205 (1974).

[Per88] S. M. Perez, Phys. Rev. Lett. **60** 13, 1342 (1988).

[Pil88] J. V. Pilcher, NAC internal report, (National Accelerator Centre, Faure, 1988).

[Pil89a] J. V. Pilcher, A. A. Cowley, D. M. Whittal, and J. J. Lawrie, Phys. Rev. C **40**, 1937 (1989).

[Pil89b] J. V. Pilcher, Ph.D. thesis, University of Cape Town, unpublished (1989).

[Pil92] J. V. Pilcher, NAC internal report, (National Accelerator Centre, Faure, 1992).

[Ros57] M. E. Rose, *Elementary Theory of Angular Momentum*, (John Wiley and Sons, New York, 1957).

[Roy67] R. R. Roy and B. P. Nigam, *Nuclear Physics - Theory and Experiment*, (John Wiley and Sons, New York, 1967), pp. 393–431.

[Sat83] G. R. Satchler, *Direct Nuclear Reactions*, (Oxford University Press, New York, 1983), pp. 90–96.

[Sat90] G. R. Satchler, *Introduction to Nuclear Reactions*, 2nd edition, (MacMillan, London, 1990), pp. 153–277.

[Sau77] F. Sauli, *Principles of Operation of Multiwire Proportional and Drift chambers*, document no. **77-09**, (CERN, Geneva, 1977).

[Sch82] P. Schwandt, *SNOOPY8 - Optical Potential Code for Elastic Scattering Analysis*, report no. **82-3**, (Indiana University Cyclotron Facility, Bloomington, 1982).

[Sch86] P. Schwandt, notes on the Indiana University Cyclotron Facility K600 spectrometer, unpublished (1986).

[Sic91] I. Sick and P. de Witt Huberts, Comments Nucl. Part. Phys. **20**, 177 (1991)

[Tro80] H. -J. Trost, A. Schwarz, U. Feindt, F. H. Heimlich, S. Heinzel, J. Hintze, F. Körber, R. Lekebusch, P. Lezoch, G. Möck, W. Paul, E. Roick, M. Wolff, J. Worzeck, and U. Strohbusch, Nucl. Phys. **A337**, 377 (1980).

[Udí93] J. M. Udías, P. Sarriguren, E. Moya de Guerra, E. Garrido, and J. A. Caballero, Phys. Rev. C **48**, 2731 (1993).

[Udí95] J. M. Udías, P. Sarriguren, E. Moya de Guerra, E. Garrido, and J. A. Caballero, Phys. Rev. C **51**, 3246 (1995).

[Val91] M. Vallières and H. Wua, *Computational Nuclear Physics I - Nuclear Structure*, K. Langanke, J. A. Maruhn, and S. E. Koonin (eds.), (Springer-Verlag, New York, 1991), pp. 1–23.

[van89] S. Y. van der Werf, M. N. Harakeh, and E. N. M. Quint, Phys. Lett. B **216**, 15 (1989).

[van94] M. G. van der Merwe, W. A. Richter, and B. A. Brown, Nucl. Phys. **A579**, 173 (1994).

[Vee93] R. Veenhof, drift-chamber simulation computer program *GARFIELD* (version 4.29), CERN program library entry **W5050**, (CERN, Geneva, 1993).

[Ver94] J. Vernotte, G. Berrier-Ronsin, S. Fortier, E. Hourani, J. Kalifa, A. Khendriche, J. M. Maison, L. H. Rosier, and G. Rotbard, Phys. Rev. C **49**, 1559 (1994).

[Wag90] G. J. Wagner, Prog. Part. Nucl. Phys. **24**, 17 (1990).

[Wal95] J. D. Walecka, *Theoretical Nuclear and Subnuclear Physics*, (Oxford Unversity Press, New York, 1995), p. 42.

[Wap71] A. H. Wapstra and N. B. Grove, Nucl. Data Tables **9** 4-5, 303 (1971).

[Weg87] H. E. Wegner, D. J. Clark, H. Wiedemann, H. A. Grunder, K. Batchelor, H. E. Jackson Jr., K. Strauch, M. Q. Barton, and U. Schumacher, in *Nuclear and Particle Phyiscs Source Book*, S. P. Parker (ed.), (McGraw-Hill, New York, 1987), pp. 398–453.

[Ynt61] J. L. Yntema, T. H. Braid, B. Zeidman, and H. W. Broek, in *Proceedings of the Rutherford Jubilee International Conference, Manchester, 1961*, J. B. Birks (ed.), (Academic Press, New York, 1961), p. 521.